NASA Technical Memorandum 110362 USAATCOM Technical Report 95-A-008

A Model Structure for Identification of Linear Models of the UH-60 Helicopter in Hover and Forward Flight

Jay W. Fletcher

Distribution Notice – Distribution authorized to U.S. Government Agencies and their contractors. Critical Technology determined August 2, 1995. Other requests for this document shall be referred to the Aeroflightdynamics Directorate (AMSAT-R-ABC), U.S. Army ATCOM, Ames Research Center, Moffett Field, CA 94035-1000.

Destruction Notice – Destroy by any method that will prevent disclosure of contents or reconstruction of the document.

August 1995

National Aeronautics and
Space Administration

US Army
Aviation and Troop Command

NASA Technical Memorandum 110362 USAATCOM Technical Report 95-A-008

A Model Structure for Identification of Linear Models of the UH-60 Helicopter in Hover and Forward Flight

Jay W. Fletcher, *Aeroflightdynamics Directorate, Aviation Research Development and Engineering Center, U.S. Army ATCOM, Ames Research Center, Moffett Field, California*

August 1995

National Aeronautics and
Space Administration

Ames Research Center
Moffett Field, CA 94035-1000

US Army
Aviation and Troop Command

Aeroflightdynamics Directorate
Moffett Field, CA 94035-1000

TABLE OF CONTENTS

Nomenclature

a	blade lift curve slope
a_o	blade coning angle measured from hub plane, rad
a_1, b_1	longitudinal and lateral tip-path-plane flapping angles, rad
a_x, a_y, a_z	body axis applied specific forces, ft/sec^2
A_1, B_1	longitudinal and lateral swashplate angles, rad
c	blade chord, ft
e	flapping hinge offset, ft
K_C	fuel controller collective anticipation gain, lbm/in.-sec
K_D	fuel controller derivative gain, lbm/sec
K_I	fuel controller integral gain, lbm/sec
K_P	fuel controller proportional gain, lbm
m	aircraft mass, slugs
M_{11}	vertical induced velocity apparent mass, slugs
N	number of blades
p, q, r	body-axis angular-rate perturbations, rad/sec
Q	equivalent shaft torque perturbation, ft-lbf
R	main rotor radius, ft
u, v, w	body axis airspeed component perturbations, ft/sec
w_f	fuel flow rate perturbation, lbm/sec
x, y, z	aircraft body axis system, positive: forward, right wing, down
δ_{lat}, δ_{lon}, δ_{ped}, δ_{col}	pilot control input perturbations, inches
Ψ	main rotor azimuth angle, rad
ψ_a	aerodynamic phase lag, rad
τ_{w_f}	fuel flow time constant, sec
Ω	engine/rotor-angular velocity, rad/sec
δ	blade mean profile drag coefficient
δ_3	pitch/flap coupling, rad
ρ	air density, slugs/ft^3
σ	main rotor solidity ratio
λ	inflow ratio
μ	advance ratio
ν	nondimensional induced velocity perturbation
ν_o	nondimensional induced velocity in hover
υ	induced velocity perturbation, ft/sec
γ	Lock number
ε	e/R
M_β	blade first flapwise mass moment, slug-ft
I_β	blade second flapwise mass moment, slug-ft^2
θ	aircraft pitch Euler angle, rad
θ_o	swashplate collective pitch angle, rad
θ_{tr}	tail rotor collective pitch angle, rad
θ_t	main rotor blade twist angle, rad
ϕ	aircraft roll Euler angle, rad

A Model Structure for Identification of Linear Models of the UH-60 Helicopter in Hover and Forward Flight

JAY W. FLETCHER

Aeroflightdynamics Directorate, Aviation Research, Development and Engineering Center, U.S. Army ATCOM, Ames Research Center

Summary

A linear model structure applicable to identification of the UH-60 flight dynamics in hover and forward flight without rotor-state data is developed. The structure of the model is determined through consideration of the important dynamic modes of the UH-60 in the frequency range of interest for flight control applications. Included are the six fuselage rigid body degrees of freedom (DOF), the rotor tip-path-plane flap and lead-lag dynamics, the main rotor angular velocity and induced velocity dynamics, and engine gas generator and governor dynamics. An empirical correction to the flapping equations referred to as the "aerodynamic phase lag" is included which emulates the effects of the main rotor dynamic wake on the development of flapping moments. The model structure is employed in the identification of linear models of the UH-60 from flight-test data at hover and 80 kts forward flight using a frequency-response-error identification method. The models are fit to flight-identified frequency responses through the adjustment of the values of the model parameters. Systematic model structure reduction is performed to ensure that minimally parameterized models are obtained. The identified models match the flight-test data well, predict the rigid body response of the UH-60 better than current generation blade-element simulation models, and are accurate from approximately 0.5 to 20 rad/sec. The identified physical flapping parameters correlate well with theoretical results. The aerodynamic phase lag formulation is shown to be an effective approach to improving the prediction of the aircraft off-axis angular-rate responses.

Introduction

Modern rotorcraft flight control system (FCS) design methods promise to yield high vehicle response bandwidth with good gust rejection. Successful achievement of these characteristics in flight depends on a design model which accurately characterizes the vehicle response up to the frequency of the regressing rotor-flap and lead-lag modes (ref. 1). Unfortunately, existing, full-flight-envelope flight simulation models used by the flight controls community may not have sufficient fidelity for this application (ref. 2).

Figure 1 compares frequency responses of two state-of-the-art blade element flight-dynamics simulation models (refs. 3 and 4) with frequency responses identified from hover flight-test data. Each simulation model, henceforth referred to as Blade Element (BE) Model A and BE Model B respectively, includes second-order tip-path-plane flap and lead-lag dynamics and a three-state dynamic induced velocity model (ref. 5). BE Model B also includes one main rotor rpm degree of freedom (DOF) and engine/governor dynamics. Both models predict the on-axis responses well to about 10 rad/sec but have deficiencies in their off-axis angular-rate response prediction. The discrepancies in the off-axis are of critical significance for FCS design since they may prevent decoupling and stability margin goals from being achieved (ref. 6). Similar off-axis modeling deficiencies have been observed in simulation models of the AH-64 (ref. 7) and BO 105 (ref. 8). This consistent discrepancy between simulation theory and experiment has led some researchers to question some of the basic assumptions made in flight dynamical modeling of single main rotor helicopters (ref. 2).

The extraction of very accurate linear models from flight-test data using system identification techniques provides an alternate source of FCS design models when such flight data are available. A linear model of the UH-60 identified from hover flight-test data which includes simplified rotor-flap and lead-lag dynamics is presented in reference 9. This model is also compared with flight test data in figure 1. The identified model fits the on-axis angular-rate responses very well up to 20 rad/sec. It also fits the pitch/roll and yaw/heave coupling responses up to the frequency limit of good coherence data at approximately 10 rad/sec.

One problem with the identified model is that constraints in the classical rotor flapping equations associated with dynamic coupling had to be relaxed to achieve these results. This decreases confidence in the robustness of the identification model structure. As Curtiss (ref. 2) implies,

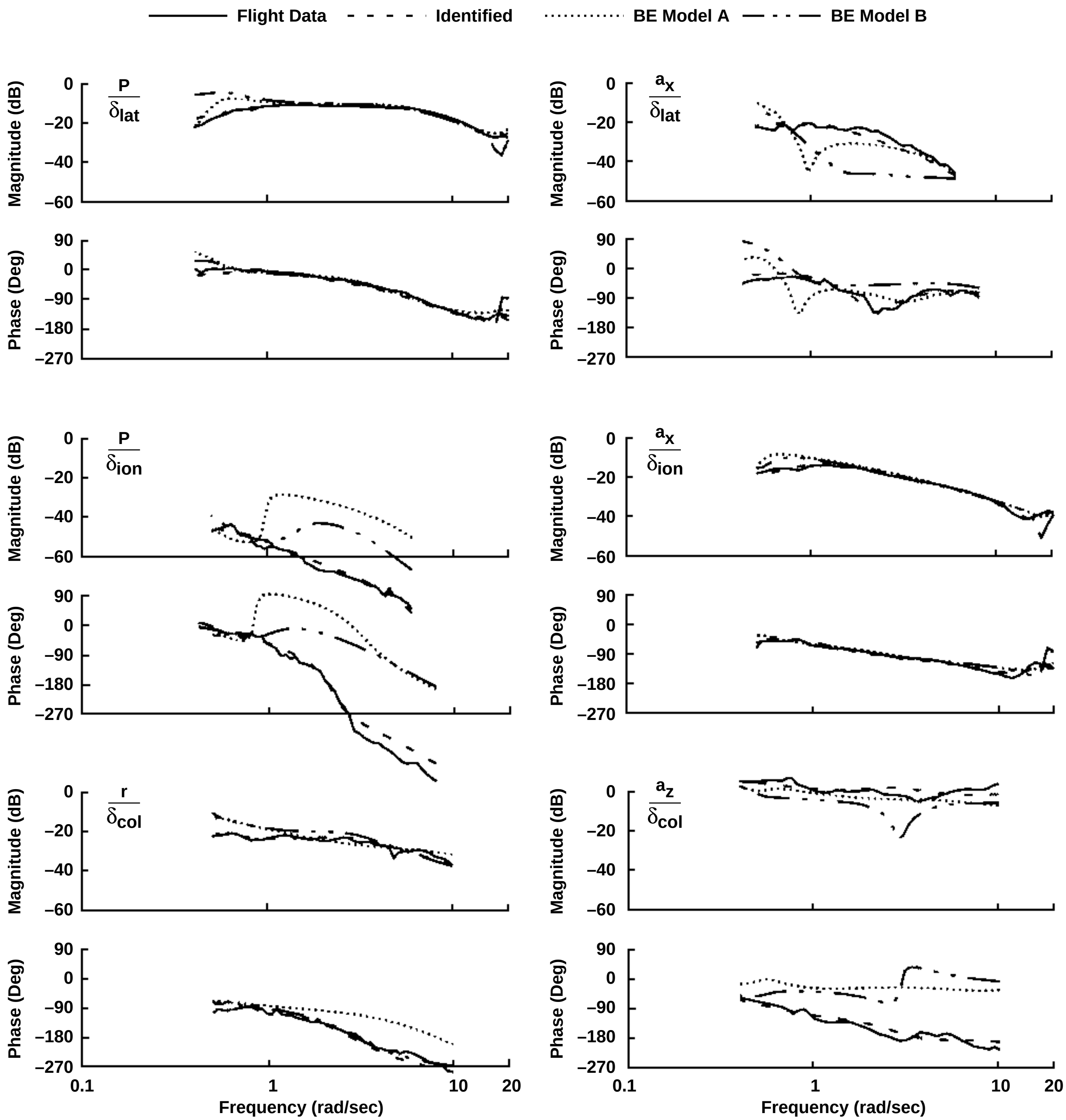

Figure 1. Comparison of blade element and identification models.

some effect is missing from the classical flapping equations which degrades fidelity in the case of the simulation models. This same effect is being compensated for by violation of constraints in the case of the identification model. A new formulation of the identification model structure is sought which will capture this effect and allow a model with correct physical constraints to be identified.

The effect in question may be the coupling of the angular DOF of the main rotor dynamic wake with the rotor flapping dynamics described by Rosen (ref. 10). Tischler has accounted for the discrepancy of the classical flapping equations in modeling the coupling response by introducing a phasing of the aerodynamic flapping moments through an adjustment of the swashplate control phasing angle (ref. 11). This aerodynamic phase correction was included in the UH-60 flight response identification for hover in reference 6. In the present study this model is refined and extended to the 80 kts forward flight condition.

This report presents the development of a generalized linear model structure applicable to identification of the UH-60 flight dynamics in hover and forward flight without rotor-state data. The structure of the model was determined through consideration of the important dynamic modes in the frequency range of interest for flight control applications. Included are the six rigid body fuselage DOF well as rotor tip-path-plane flap and lead-lag dynamics, main rotor rpm and induced velocity dynamics, and engine gas generator and governor dynamics. The aerodynamic phase lag correction to the flapping equations is included to capture the correct coupling behavior of the aircraft.

This report also documents the application of this model structure in the identification of models of the UH-60 flight dynamics for hover and 80 kts forward flight. These models have high fidelity in the frequency range of 0.3 to 20 rad/sec and are currently being used in the design of airspeed-scheduled flight control laws for the Rotorcraft Aircrew Systems Concepts Airborne Laboratory (RASCAL) (ref. 12) UH-60 helicopter (fig. 2) at Ames Research Center (ref. 6).

Identification Model Structure Formulation

The model structure formulation process consists of determining which dynamics are to be included in the model and how they are to be parameterized. This is largely determined by the required frequency range of the model and the number of dynamic states which are measured during the flight test. The effects of all of the dynamics which have significant modal responses in the desired frequency range should be included. However, it may be difficult to uniquely identify all of the dynamics if enough measurements are not available to allow the unique effects of each component of the system to be detectable in the data. In particular, it is difficult to simultaneously identify fuselage, rotor, and inflow dynamics if only fuselage measurements are available. If overparameterization occurs, some parts of the model must be fixed at theoretical values or a simplification of the dynamics must be made.

Both analytical (refs. 13, 1, and 14) and flight (refs. 15 and 16) investigations have demonstrated the need to explicitly represent the dynamics in the frequency range

Figure 2. The RASCAL UH-60 Helicopter.

of the regressing rotor modes in models used for the design of high bandwidth flight control systems. A major objective of this study was to determine a system identification model structure which meets this requirement and will not be overparameterized when rotor-state data are not available. This objective has been achieved by coupling simplified rigid blade flapping equations valid for frequencies approaching and beyond the flap regressing mode with six DOF quasi-steady fuselage equations valid for frequencies below the flap regressing mode. Special care is taken not to duplicate physical effects between the stability derivatives and coefficients in the rotor flapping equations. A parasitic dipole representation of the lead-lag dynamics (one-way coupled to the aircraft on-axis angular-rate response) characterizes the effects of the lead-lag dynamics in the frequency range of interest without overparameterization.

A second objective was to determine an identification model structure which would match the off-axis flight-test data without relaxing the physical constraints in the classical flapping equations. The work of Rosen, et al. in reference 10 on modeling unsteady aerodynamics indicates that the variation in wake geometry due to rotor pitch and roll motion has a significant effect on the development of blade aerodynamic forces and moments. This effect is not modeled in the Pitt/Peters dynamic inflow theory (ref. 5). Rosen and his colleagues developed a complex model that accounts for the full coupling between the rotor dynamics and the wake and shows excellent correlation of rotorcraft cross-coupling in hover for both the AH-64 and UH-60 helicopters. Recent results from an identification study (ref. 11) using wind tunnel data from a full-scale shaft-fixed test of a bearingless main rotor indicate that the cross-coupling prediction of the classical flapping equations with three-state dynamic inflow could be significantly improved by adjusting the swashplate control phasing. These results were later extended to the shaft-free case of the UH-60 in hover in reference 6 by replacing the swashplate control phase angle shift by a rotor blade aerodynamic phase lag, ψ_a. The hover results are herein refined and extended to the 80 kts forward flight case as well.

Previous theoretical (ref. 17) and experimental (refs. 4 and 9) studies have shown that the main rotor rpm/engine/governor dynamics of the UH-60 couple significantly into the overall yaw/heave response of the aircraft in hover. Also, the main rotor induced velocity dynamics have a major influence on the helicopter vertical response in hover since the vertical induced velocity mode often has a natural frequency near the regressing flap mode (ref. 18). The identification model structure was therefore extended to include all of these dynamic effects in hover as well.

The overall model structure includes fuselage rigid body dynamics, second-order main rotor tip-path-plane flap and lead/lag dynamics, and collective dynamic induced velocity, main rotor/engine angular rate, engine torque, and engine fuel flow dynamics. The induced velocity, rpm, torque, and fuel flow dynamics largely decouple from the remainder of the model in forward flight. Derivations of the various components of the model will now be covered.

Flapping Equations

The linearized tip-path-plane flapping equations of motion shown in equations (1)–(6) were obtained through simplification of equation (1) of reference 19. These rigid blade equations were derived with highly simplified aerodynamics and the assumption of constant rotor rpm. A further "high frequency approximation" was made by eliminating the terms dependent on vehicle velocity perturbations. This significantly reduces the number of free parameters in the equations, but limits their applicability to frequencies approaching and above the flap regressing mode frequency. The lower frequency effects of the main rotor flapping are retained in the quasi-steady fuselage equations as described below.

The aerodynamic terms of the flapping equations are denoted C_{aero}, A_{aero}, and B_{aero} respectively. They are separated from the inertial terms for convenience in the identification process, as will become evident below.

$$\ddot{a}_0 - \frac{M\beta}{I\beta}\dot{w} + C_{aero} = -\Omega^2\left(1 + e\frac{M\beta}{I\beta}\right)a_0 \quad (1)$$

$$\ddot{a}_1 + \dot{q} + 2\Omega\dot{b}_1 + A_{aero} = -\Omega^2 e\frac{M\beta}{I\beta}a_1 - 2\Omega\left(1 + e\frac{M\beta}{I\beta}\right)p \quad (2)$$

$$\ddot{b}_1 + \dot{p} - 2\Omega\dot{a}_1 + B_{aero} = -\Omega^2 e\frac{M\beta}{I\beta}b_1 + 2\Omega\left(1 + e\frac{M\beta}{I\beta}\right)q \quad (3)$$

$$C_{aero} = \frac{\gamma\Omega}{2}\left[\frac{1}{4}-\frac{2}{3}\varepsilon\right]\dot{a}_0 - \mu\frac{\gamma\Omega}{4}\left[\frac{1}{3}-\varepsilon\right]\dot{b}_1$$
$$+\delta_3\frac{\gamma\Omega^2}{2}\left[\frac{1}{4}-\frac{\varepsilon}{3}+\mu^2\left(\frac{1}{4}-\frac{\varepsilon}{2}\right)\right]a_0 - \mu\varepsilon\frac{\gamma\Omega^2}{8}a_1$$
$$-\mu\delta_3\frac{\gamma\Omega^2}{4}\left[\frac{2}{3}-\varepsilon\right]b_1 - \mu\frac{\gamma\Omega}{8}\left[\frac{2}{3}-\varepsilon\right]p$$
$$-\frac{\gamma\Omega}{2R}\left[\frac{1}{3}-\frac{\varepsilon}{2}\right]w + \frac{\gamma\Omega}{2R}\left[\frac{1}{3}-\frac{\varepsilon}{2}\right]\upsilon$$
$$+\mu\frac{\gamma\Omega^2}{2}\left[\frac{1}{3}-\frac{\varepsilon}{2}\right]B_1$$
$$-\frac{\gamma\Omega^2}{2}\left[\frac{1}{4}-\frac{\varepsilon}{3}+\mu^2\left(\frac{1}{4}-\frac{\varepsilon}{2}\right)\right]\theta_0 \tag{4}$$

$$A_{aero} = \frac{\gamma\Omega}{2}\left[\frac{1}{4}-\frac{2}{3}\varepsilon\right]\dot{a}_1 - \mu\frac{\gamma\Omega^2}{2}\left[\frac{1}{3}-\frac{\varepsilon}{2}\right]a_0$$
$$+\delta_3\frac{\gamma\Omega^2}{2}\left[\frac{1}{4}-\frac{\varepsilon}{3}+\mu^2\left(\frac{1}{8}-\frac{\varepsilon}{4}\right)\right]a_1$$
$$+\frac{\gamma\Omega^2}{2}\left[\frac{1}{4}-\frac{2}{3}\varepsilon+\mu^2\left(\frac{1}{8}-\frac{\varepsilon}{4}\right)\right]b_1$$
$$+\frac{\gamma\Omega}{2}\left[\frac{1}{4}-\frac{\varepsilon}{3}\right]q - \frac{\gamma\Omega^2}{2}\left[\frac{1}{4}-\frac{\varepsilon}{3}+\mu^2\left(\frac{1}{8}-\frac{\varepsilon}{4}\right)\right]A_1 \tag{5}$$

$$B_{aero} = -\mu\frac{\gamma\Omega}{2}\left[\frac{1}{3}-\varepsilon\right]\dot{a}_0 + \frac{\gamma\Omega}{2}\left[\frac{1}{4}-\frac{2}{3}\varepsilon\right]\dot{b}_1$$
$$-\mu\delta_3\frac{\gamma\Omega^2}{2}\left[\frac{2}{3}-\varepsilon\right]a_0$$
$$-\frac{\gamma\Omega^2}{2}\left[\frac{1}{4}-\frac{2}{3}\varepsilon-\mu^2\left(\frac{1}{8}-\frac{\varepsilon}{4}\right)\right]a_1$$
$$+\frac{\gamma\Omega}{2}\left[\frac{1}{4}-\frac{\varepsilon}{3}\right]p$$
$$+\delta_3\frac{\gamma\Omega^2}{2}\left[\frac{1}{4}-\frac{\varepsilon}{3}+3\mu^2\left(\frac{1}{8}-\frac{\varepsilon}{4}\right)\right]b_1$$
$$+\mu\frac{\gamma\Omega}{2R}\left[\frac{1}{2}-\varepsilon\right]w - \mu\frac{\gamma\Omega}{2R}\left[\frac{1}{2}-\varepsilon\right]\upsilon \tag{6}$$
$$+\mu\frac{\gamma\Omega^2}{2}\left[\frac{2}{3}-\varepsilon\right]\theta_0$$
$$-\frac{\gamma\Omega^2}{2}\left[\frac{1}{4}-\frac{\varepsilon}{3}+3\mu^2\left(\frac{1}{8}-\frac{\varepsilon}{4}\right)\right]B_1$$

The first three equations are herein referred to as the “C," “A," and “B” equations respectively. The second three are referred to as the “C_{aero},” “A_{aero},” and “B_{aero}” equations. Terms multiplying a state variable are analogous to stability derivatives. For example, the derivative $A_{\dot{b}_1}$ has the value –2Ω.

The advance ratio, nominal rotor-angular velocity, hinge offset, and rotor radius were fixed at their known physical values in the flapping equations. The remaining identification parameters are Lock number, γ, pitch/flap coupling, δ_3, and the ratio M_β/I_β. The resulting physical constraints between the terms of the flapping equations and these three free parameters were enforced in the identification.

Aerodynamic Phase Lag[1]

Recent results from an identification study (ref. 11) using full-scale bearingless main rotor (BMR) wind tunnel test data have been used here to modify the above tip-path-plane flapping equations to correctly capture the off-axis response. This is an empirical approach rather than the complete physical dynamic wake implementation of Rosen, but is easily incorporated into the existing blade-element rotor theory in equations (1)–(6). The development of this approach will now be covered.

The BMR identification model structure included the dynamics of flapping, lead-lag, and dynamic induced velocity and was formulated in terms of the physical parameters of the rotor (e.g., weight, inertia, hinge-offset, lift-curve slope, etc.). The study showed that the conventional rotor equations, including three-state Pitt-Peters induced velocity, accurately capture the on-axis responses to control inputs. This was confirmed by a full blade-element simulation model of the BMR (ref. 11). However, an accurate match of the off-axis responses required an adjustment in the known (geometric) swashplate control phasing angle. This result was confirmed by inserting the adjusted control phasing into the simulation model, which then correctly predicted the off-axis responses. The use of swashplate control phasing as a simulation tuning parameter was not fully successful for (shaft-free) flight responses (ref. 11), indicating that an alteration of the correction technique was needed to account for the aerodynamic coupling caused by shaft motion.

As discussed in reference 11, the adjustment of the swashplate phase angle is equivalent to an azimuthal rotation in the fixed-frame rotor aerodynamics, or a “lag” in the rotating frame (blade) aerodynamics. This is similar in effect to the Theodorsen function but larger in magnitude.

---

[1]Section from reference 6, written and updated by M. B. Tischler.

Follow-on identification analyses of the BMR data by Tischler have been based on the direct identification of this effective "aerodynamic phase lag," ψ_a defined in equation (7).

$$\begin{aligned} A'_{aero} &= A_{aero}\cos\psi_a - B_{aero}\sin\psi_a \\ B'_{aero} &= B_{aero}\cos\psi_a + A_{aero}\sin\psi_a \end{aligned} \tag{7}$$

The variables A_{aero} and B_{aero} are the fixed-frame cosine and sine aerodynamic moment components for the conventional rotor formulation in equations (1)–(6). The variables A'_{aero} and B'_{aero} are the fixed-frame moments including the aerodynamic phase lag correction.

Although the aerodynamic phase lag formulation is essentially comparable to swashplate tuning in the wind tunnel, this new approach also yields a correct prediction of cross-coupling for shaft-free flight simulation models. Analysis of an AH-64 helicopter has shown very close agreement between the results of Rosen's dynamic wake analysis, the present aerodynamic phase lag correction formulation, and flight data. An advantage of the present approach is that the aerodynamic phase lag, ψ_a, can easily be identified for a range of flight conditions and incorporated into existing flight-simulation models.

The aerodynamic phase lag correction is included in the flapping dynamics for hover by substituting A'_{aero} and B'_{aero} for A_{aero} and B_{aero} in equations (1)–(6). The aero phase lag, ψ_a, then becomes an additional parameter in the identification. The corrected aerodynamic moments are also scaled according to equation (8) to ensure that the on-axis responses of the identified model are not significantly affected by the off-axis correction.

$$\begin{aligned} A''_{aero} &= A'_{aero}\sec\psi_a \\ B''_{aero} &= B'_{aero}\sec\psi_a \end{aligned} \tag{8}$$

The lag in the rotating frame aerodynamics can be directly implemented in the body frame coning dynamics through the addition of a lagged aerodynamic force state to the model defined by $\tau \dot{C}'_{aero} + C'_{aero} = C_{aero}$ where $\psi_a = \tau\Omega$.

Collective Induced Velocity

From reference 18, the nonlinear, nondimensional uniform induced velocity equation for hover is

$$\frac{M_{11}}{\Omega}\frac{d\nu}{dt} + 2\left(\nu - \frac{w}{\Omega R} + \frac{2}{3}\frac{\dot{a}_0}{\Omega}\right)\nu = \frac{a\sigma}{2}\left\{\frac{1}{2}\left(\frac{w}{\Omega R} - \nu\right) + \frac{\theta_0}{3} + \frac{\theta_t}{4} - \frac{\dot{a}_0}{\Omega}\left(\frac{1}{3} - \frac{\varepsilon}{2}\right)\right\} \tag{9}$$

where $\nu = \dfrac{\upsilon}{\Omega R}$ is the nondimensional uniform induced velocity. Making this substitution, evaluating the derivative of the induced velocity, and linearizing with respect to the state variables yields the following dimensional linear uniform induced velocity perturbation, or "I" equation

$$\dot{\upsilon} - \frac{\upsilon_0}{\Omega_0}\dot{\Omega} = \frac{1}{M_{11}}\left\{\begin{aligned} &\left[\frac{2\upsilon_0}{R} + \frac{a\sigma\Omega_0}{4}\right]w - \left[\frac{4\upsilon_0}{R} + \frac{a\sigma\Omega_0}{4}\right]\upsilon \\ &-\left[\frac{4}{3}\upsilon_0 + \frac{a\sigma R\Omega_0}{2}\left(\frac{1}{3} - \frac{\varepsilon}{2}\right)\right]\dot{a}_0 \\ &+\left[\frac{3a\sigma R\Omega_0}{8} - \frac{a\sigma\upsilon_0}{2} - \frac{2\upsilon_0^2}{R\Omega_0}\right]\Omega \\ &+\left[\frac{a\sigma R\Omega_0^2}{6}\right]\theta_0 \end{aligned}\right\} \tag{10}$$

The terms of equation (10) in square brackets are identified as lumped parameters.

Rotor Angular Velocity

Considering inertial, engine torque, aerodynamic, and Correolis generated accelerations, and neglecting lead/lag, the nonlinear main rotor-angular velocity equation can be shown to be

$$I_R\left(\frac{d\Omega}{dt} - \frac{dr}{dt}\right) - 2N(\Omega - r)\left(I_\beta + eM_\beta\right)\beta\dot{\beta} = Q_E - Q_A \tag{11}$$

where $I_R = I_\zeta + N(e^2 m_\beta + I_\beta + 2eM_\beta)$ is the rotor system rotational inertia, Q_E is the total applied engine torque, and Q_A is the resultant aerodynamic torque acting about the rotor shaft defined in equation (12) from reference 20.

$$Q_A = \frac{1}{2}\rho a c N R^4 \Omega^2 \left\{ \begin{array}{l} \dfrac{\delta}{4a} - \left[\dfrac{\lambda}{3} + \left(\dfrac{\varepsilon}{3} - \dfrac{1}{4}\right)\dfrac{\dot{\beta}}{\Omega}\right]\theta_0 \\ -\dfrac{\theta_t}{4}\lambda - \left(\dfrac{\varepsilon}{4} - \dfrac{1}{5}\right)\theta_t \dfrac{\dot{\beta}}{\Omega} \\ -\dfrac{1}{2}\left(1-\varepsilon^2\right)\left[\lambda^2 + 2\lambda\varepsilon\dfrac{\dot{\beta}}{\Omega}\right] \\ +\dfrac{2}{3}\lambda\dfrac{\dot{\beta}}{\Omega} - \left(\dfrac{1}{4} - \dfrac{2}{3}\varepsilon\right)\left(\dfrac{\dot{\beta}}{\Omega}\right)^2 \end{array} \right\} \tag{12}$$

The inflow ratio in equation (12) is defined as

$$\lambda = \frac{w - \upsilon - \upsilon_0}{R\Omega}$$

Making the substitution for Q_A and λ, and linearizing with respect to the state variables yields the following linear rpm perturbation, or “R” equation

$$\dot{\Omega} - \dot{r} = \frac{N\gamma I_\beta}{R I_R} \left\{ \begin{array}{l} \left[\begin{array}{l} \left[\begin{array}{l} \upsilon_0\left(\dfrac{1}{3} - \dfrac{\varepsilon}{2}\right) \\ + \dfrac{2\beta_0\Omega_0 R}{\gamma}\left(\dfrac{eM_\beta}{I_\beta} + 1\right) \end{array} \right]\dot{\beta} \\ -\Omega_0\theta_t R\left(\dfrac{1}{10} - \dfrac{\varepsilon}{8}\right) \end{array} \right] \\ +\left[\dfrac{\Omega_0\theta_t}{8} - \dfrac{\upsilon_0}{2R}\right]w - \left[\dfrac{\Omega_0\theta_t}{8} - \dfrac{\upsilon_0}{2R}\right]\upsilon \\ -\left[\dfrac{\upsilon_0\theta_t}{8} + \dfrac{\delta R\Omega_0}{4a}\right]\Omega + \left[\dfrac{\upsilon_0\Omega_0}{6}\right]\theta_0 \end{array} \right\} + Q_E \tag{13}$$

The terms of equation (13) in square brackets were also identified as lumped parameters subject to the constraint, $R_w = R_\upsilon$.

Engine/Governor/Fuel Flow

The engine torque, fuel flow and rpm governor dynamics are depicted graphically in figure 3. The torque and fuel flow equations (with the governor included) are written in first order form in equations (14) and (15).

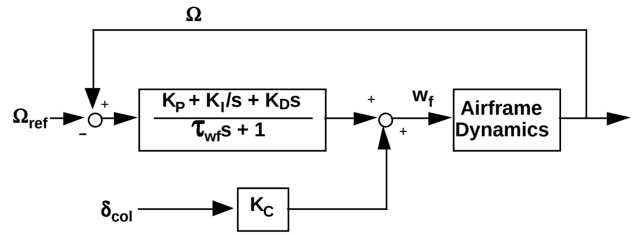

Figure 3. Engine, governor, fuel flow dynamics.

$$\dot{Q} = T_Q Q + T_{w_f} w_f + K_C T_{w_f}\delta_{col} \tag{14}$$

$$\tau_{w_f}\dot{w}_f = -w_f - K_D\dot{\Omega} + K_P\Omega + K_I\int\Omega \tag{15}$$

Values for the governor parameters K_C, K_D, K_I, and K_P were identified by Kim (ref. 4) using an analytical model of the UH-60 dynamics in hover, and have been retained in the identified models reported here. The constraint $T_{\delta_{col}} = K_C T_{w_f}$ defines the collective anticipation in the governor and was enforced in the identification.

Yaw and Heave

The components of the vertical acceleration, “Z,” and yaw acceleration, “N,” equations due to the rotor flapping, induced velocity, rotor rpm, and aircraft vertical velocity perturbations were obtained through linearization of equations (2) and (15) of reference 19 with respect to the chosen state variables. The resulting acceleration components are shown in equations (16) and (17).

$$a_Z + N\frac{M_\beta}{m}\ddot{a}_0 = \frac{N}{2m}\rho a c R\left(\Omega_0 R\right)^2 \left\{ \begin{array}{l} \left[\dfrac{1}{\Omega_0}\left(\dfrac{1}{3} - \dfrac{\varepsilon}{2}\right)\right]\dot{a}_0 - \left[\dfrac{\mu}{\Omega_0}\left(\dfrac{1}{4} - \dfrac{\varepsilon}{2}\right)\right]\dot{b}_1 + \delta_3\left[\dfrac{1}{3} + \dfrac{\mu^2}{2}(1-\varepsilon)\right]a_0 - \dfrac{\varepsilon\mu}{2}a_1 \\ -\dfrac{\delta_3\mu}{2}b_1 + \left[\dfrac{1}{2\Omega_0 R}\right]\upsilon - \left[\dfrac{1}{2\Omega_0 R}\right]w + \left[\dfrac{\upsilon_0}{2\Omega_0^2 R} - \dfrac{\theta_t}{2\Omega_0}\left(1+\mu^2\right)\right]\Omega + \dfrac{\mu}{2}B_1 \\ -\left[\dfrac{1}{3} + \dfrac{\mu^2}{2}(1-\varepsilon)\right]\theta_0 \end{array} \right\} \tag{16}$$

$$a_N = \frac{N}{2I_{ZZ}} \rho a c R^2 (\Omega_0 R)^2 \left\{ \begin{array}{l} \left[\frac{\upsilon_o}{\Omega_0^2}\left(\varepsilon - \frac{2}{3}\right) + \frac{\theta_t}{\Omega_0}\left(\frac{1}{5} - \frac{\varepsilon}{4}\right) \right] \dot{a}_0 + \left[\frac{\mu\theta_t}{\Omega_0}\left(\frac{\varepsilon}{6} - \frac{1}{8}\right) \right] \dot{b}_1 - \left[\frac{\delta_3 \upsilon_o}{3\Omega_0 R} \right] a_0 \\ + \frac{\mu}{2}\left(\frac{\upsilon_o}{\Omega_0 R} - \frac{\varepsilon\theta_t}{3} \right) a_1 + \frac{\delta_3 \mu \upsilon_o}{4\Omega_0 R} b_1 + \left[\frac{\upsilon_o}{\Omega_0^2 R^2} - \frac{\theta_t}{4\Omega_0 R} \right] \upsilon \\ - \left[\frac{\upsilon_o}{\Omega_0^2 R^2} - \frac{\theta_t}{4\Omega_0 R} \right] w + \left[\frac{\upsilon_o \theta_t}{4\Omega_0 R} + \frac{\delta}{2a\Omega_0}\left(1 + \mu^2\right) \right] \Omega - \frac{\mu \upsilon_o}{4\Omega_0 R} B_1 \\ - \left[\frac{\upsilon_o}{3\Omega_0 R} \right] \theta_0 \end{array} \right\} \tag{17}$$

The terms in square brackets in these equations were also identified as independent lumped parameters, except where physical constraints exist. Constraints between the "N" derivatives include $N_w = -N_\upsilon$, $N_{a_0} = -\delta_3 N_{\theta_0}$, and $N_{b_1} = -\delta_3 N_{B_1}$. Constraints between the "Z" derivatives include, $Z_w = -Z_\upsilon$, $Z_{a_0} = -\delta_3 Z_{\theta_0}$, and $Z_{b_1} = -\delta_3 Z_{B_1}$. The "w" terms are the Z_w and N_w derivatives in the quasi-steady stability derivative formulation. The other terms couple the rotor-angular velocity, induced velocity, and tip-path-plane flapping dynamics into the body heave and yaw dynamics. Additional coupling between the rotor and fuselage occurs due to tilt of the tip-path-plane as explained below.

Rotor/Body Coupling

The primary effect of tip-path-plane motions on the fuselage is the generation of pitch and roll moments at the hub and projection of thrust vector components along the x- and y-body axes. The resulting body axis angular accelerations, M_{a_1} and L_{b_1}, depend on hinge offset, the height of the rotor above the c.g., and the aircraft moments of inertia, I_{XX} and I_{YY}. For small tilt angles, and constant thrust the resulting body axis linear acceleration components are $X_{a_1} = -ga_1$ and $Y_{b_1} = gb_1$. The effects of tip-path-plane tilt on the vertical and yaw accelerations of the fuselage are less intuitive but are accounted for in the above "N" and "Z" equations, as are the effects of coning.

Fuselage Equations

The modified stability derivative formulation of the rigid-body fuselage equations of motion is shown in equation (18). Inputs to the model are in terms of the swashplate and tail rotor servo angular deflections for consistency with the rotor-flapping equations. The effects of coupling from the flapping, rpm, induced velocity, and torque equations are also shown as inputs for clarity, although these variables are treated as states in the overall model. Terms which appear only in forward flight are shown in bold.

Stability and control derivatives which are due primarily to the short-term effects of rotor-flap and coning motions should be removed from the rigid-body part of the formulation to prevent duplication of effects within the overall model structure. These effects are now accounted for in the flapping equations and are transferred to the fuselage through the coupling parameters described above. Examples are all of the A_1 and most of the B_1 control derivatives which have been removed. The remaining control derivatives are due to the changes in main and tail rotor thrusts directly produced by changes in collective main and tail rotor pitch angles.

In the hover flight condition, the X, L, and M stability derivatives due to p and q are dominated by the high frequency effects of the rotor and should be removed. However, the Y, Z, and N derivatives due to p and q should remain because they are mostly produced by the effects of the high, canted tail rotor. Other terms to be dropped from the N and Z equations in hover can be determined by setting $\mu = 0$ in equations (16) and (17).

Some of the derivatives which were redundant in hover may become distinct in forward flight. They may be required to model fuselage aerodynamics which are more significant and complex at this flight condition. A good example is the more significant M_q produced by the stabilator in forward flight.

The linearized transformation from pilot control inputs in inches to swashplate and tail rotor servo angles in radians is shown in equation (19). This was derived from the model presented in appendix A of reference 21 which assumes a control phase angle $\Delta = -9.7$ deg.

$$
\left\{\begin{matrix}\dot{u}\\ \dot{v}\\ \dot{w}\\ \dot{p}\\ \dot{q}\\ \dot{r}\\ \dot{\phi}\\ \dot{\theta}\end{matrix}\right\}=
\begin{bmatrix}
X_u & X_v & X_w & \mathbf{X_p} & \mathbf{X_q-w_0} & \mathbf{X_r+v_0} & & -g\\
Y_u & Y_v & Y_w & Y_p+\mathbf{w_0} & Y_q & Y_r-\mathbf{u_0} & g & \\
Z_u & Z_v & Z_w & Z_p-\mathbf{v_0} & Z_q+\mathbf{u_0} & Z_r & & \\
L_u & L_v & L_w & \mathbf{L_p} & \mathbf{L_q} & L_r & & \\
M_u & M_v & M_w & \mathbf{M_p} & \mathbf{M_q} & M_r & & \\
N_u & N_v & N_w & N_p & N_q & N_r & & \\
 & & & 1 & & & & \\
 & & & & 1 & & &
\end{bmatrix}
\left\{\begin{matrix}u\\ v\\ w\\ p\\ q\\ r\\ \phi\\ \theta\end{matrix}\right\}
$$

$$
+\begin{bmatrix}
 & & X_{\theta_0} & \mathbf{X_{\theta_{tr}}}\\
 & & Y_{\theta_0} & Y_{\theta_{tr}}\\
 & Z_{B_1} & Z_{\theta_0} & Z_{\theta_{tr}}\\
 & & L_{\theta_0} & L_{\theta_{tr}}\\
 & & M_{\theta_0} & M_{\theta_{tr}}\\
 & N_{B_1} & N_{\theta_0} & N_{\theta_{tr}}\\
 & & & \\
 & & &
\end{bmatrix}
\left\{\begin{matrix}A_1\\ B_1\\ \theta_o\\ \theta_{tr}\end{matrix}\right\}
+\begin{bmatrix}
 & & & & X_{a_1} & & & & \\
 & & & & & Y_{b_1} & & & \\
Z_{\dot{a}_0} & & \mathbf{Z_{\dot{b}_1}} & Z_{a_0} & \mathbf{Z_{a_1}} & \mathbf{Z_{b_1}} & Z_\upsilon & Z_\Omega & \\
 & & & & & L_{b_1} & & & \\
 & & & & M_{a_1} & & & & \\
N_{\dot{a}_0} & & \mathbf{N_{\dot{b}_1}} & N_{a_0} & \mathbf{N_{a_1}} & \mathbf{N_{b_1}} & N_\upsilon & N_\Omega & N_Q\\
 & & & & & & & & \\
 & & & & & & & &
\end{bmatrix}
\left\{\begin{matrix}\dot{a}_0\\ \dot{a}_1\\ \dot{b}_1\\ a_0\\ a_1\\ b_1\\ \upsilon\\ \Omega\\ Q\end{matrix}\right\}
\tag{18}
$$

$$
\left\{\begin{matrix}A_1\\ B_1\\ \theta_0\\ \theta_{tr}\end{matrix}\right\}=
\begin{bmatrix}
0.02753 & 0.008322 & -0.004782 & -0.005769\\
0.004705 & -0.04869 & 0.02798 & 0.007230\\
0 & 0 & 0 & 0.02795\\
0 & 0 & -0.09667 & 0.02795
\end{bmatrix}
\left\{\begin{matrix}\delta_{lat}\\ \delta_{lon}\\ \delta_{ped}\\ \delta_{col}\end{matrix}\right\}
\tag{19}
$$

Lead-Lag Dynamics

Simple identification model structures are not available for the lead-lag dynamics in terms of the physical rotor parameters. As discussed in reference 22, the effect of the regressing lead-lag dynamics for frequencies below 1/rev can be modeled by the addition of a second-order dipole appended to the roll-rate response to lateral stick according to equation (20). In equation (20) the shorthand notation $[\zeta,\omega]$ implies $s^2 + 2\zeta\omega s + \omega^2$, where $\zeta =$ damping ratio, $\omega =$ undamped natural frequency (rad/sec).

In references 23 and 9, this approach was extended to the pitch axis as well by appending another dipole with the same denominator eigenvalues to the pitch response. It was refined further in reference 6 by converting the transfer functions to observer canonical form and adding them to the state equations to act as filters on the p and q outputs of the model according to equations (21) and (22).

$$\left(\frac{p}{\delta_{lat}}\right)_{lead-lag} = \left(\frac{p}{\delta_{lat}}\right)\frac{[\zeta_p, \omega_p]}{[\zeta_{ll}, \omega_{ll}]} \tag{20}$$

$$\begin{Bmatrix} \dot{x}_1 \\ \dot{x}_2 \\ \dot{x}_3 \\ \dot{x}_4 \end{Bmatrix} = \begin{bmatrix} & 1 & & \\ x_{21} & x_{22} & & \\ & & & 1 \\ & & x_{21} & x_{22} \end{bmatrix} \begin{Bmatrix} x_1 \\ x_2 \\ x_3 \\ x_4 \end{Bmatrix} + \begin{bmatrix} x_{1p} & \\ x_{2p} & \\ & x_{3q} \\ & x_{4q} \end{bmatrix} \begin{Bmatrix} p \\ q \end{Bmatrix} \tag{21}$$

$$\begin{Bmatrix} p' \\ q' \end{Bmatrix} = \begin{bmatrix} 1 & & & \\ & & 1 & \end{bmatrix} \begin{Bmatrix} x_1 \\ x_2 \\ x_3 \\ x_4 \end{Bmatrix} + \begin{bmatrix} p_p & \\ & q_q \end{bmatrix} \begin{Bmatrix} p \\ q \end{Bmatrix} \tag{22}$$

Implementing the lead-lag dynamics this way models the true dynamic effect of the lead-lag on roll- and pitch-rate responses produced by any of the model inputs. It also simplifies enforcement of the real constraint that the low frequency gain of the filter be equal to unity.

Cyclic Dynamic Induced Velocity Model

The air mass dynamics are heavily coupled to the flapping dynamics in the hover flight condition, and, therefore, cannot be neglected in the present model. Previous identification studies (ref. 24) have shown, however, that excessive parameter correlation makes it very difficult to identify induced velocity dynamics parameters even when rotor blade motion measurements are available. An alternative used by Fletcher (ref. 9) and Harding (ref. 24) is to absorb the effects of the first harmonic induced velocity into the flapping equations through the use of the reduced Lock number (ref. 25) defined in equation (23).

$$\gamma^* = \frac{\gamma}{1 + \frac{a\sigma}{16\nu_o}} \tag{23}$$

In the present study, explicit vertical induced velocity dynamics were identified for hover, so the actual Lock number was identified in the coning equation. The reduced Lock number was constrained to it through equation (23) and employed in the cyclic flapping equations. For the forward flight condition, $\mu = 0.2$, the induced velocity ratio is very small, and all components of the induced velocity dynamics can be neglected resulting in the identification of one Lock number for the flapping and coning equations.

Complete Linear Model Structure for Identification

The complete, 33-state formulation of the identification model structure is shown in state-space form in Appendix A. Partitions in the stability and control derivative matrices serve to illustrate where coupling occurs between the fuselage, flapping, lead-lag and engine/governor/induced velocity dynamics. The control matrix represents the known control phasing though the swashplate and mixer. This formulation can be simplified to the hover case, by setting the advance ratio equal to zero, or to the forward flight case, by removing the rpm, induced velocity, torque, fuel flow, and rotor azimuth equations.

Identification Method

The frequency-response-error method of CIFER® (ref. 23) was used to identify the models presented in this paper. First, CIFER® is used to identify high quality, broad-band frequency responses from the flight-test data. Then, parameter values in the state-space representation of the system dynamics are determined by CIFER® through minimization of the weighted fit errors between the model and flight identified frequency responses.

The model structure is reduced to a minimum set of parameters by sequentially dropping the relatively insignificant parameters and reconverging the remaining model parameters to a best fit of the data until the overall cost function increases significantly. The choice of which parameter to drop is based on calculations of parameter insensitivities, Cramer–Rao bounds, and multiple parameter correlations each time the model is reconverged. Insensitive parameters are removed until a minimum number of parameters with insensitivity values exceeding a target value of 10 percent remain. Excessively-correlated parameters are then removed until a minimum number of parameters with Cramer–Rao percents greater than a target value of 20 percent remain. This approach has been found to be very reliable in model structure reduction, validating the relevance of the chosen accuracy metrics.

The final, minimally-parameterized model is checked for robustness by driving it with flight-measured control inputs of a different character than those used in the identification, and comparing the model responses to those measured in flight. The reader is referred to reference 23 for additional background on CIFER®.

Flight Test Results

Data Collection

A flight test program was initiated to collect flight-test data suitable for open-loop identification and verification using the RASCAL UH-60 Helicopter. Tests were conducted in hover and 80 kts forward flight under very calm wind conditions at the Ames flight test facility located at Crows Landing, Calif. in September 1992. The takeoff gross weight was approximately 15,350 lb and the c.g. was at station 360 for all flights.

Engine response flight-test data from the Airloads UH-60 (ref. 26) were used to supplement the RASCAL flight-test data in order to extend the hover model to include coupled body/rotor/engine dynamics. Merging these two data bases was deemed reasonable because the engine response dynamics are not highly airframe specific. An advantage of the frequency response identification process is the flexibility to use data from nonconcurrent flight test records.

Frequency sweeps (ref. 27), 2-3-1-1 multisteps,[2] and doublets were manually input into each pilot control with the Stability Augmentation System (SAS) and Flight Path Stabilization (FPS) system disengaged. The pilot was asked to minimize the use of off-axis inputs during the maneuvers to prevent correlation between controls. An effective piloting technique is to maintain the trim condition and stabilize the aircraft using pulse type inputs in the off-axis controls. Each maneuver was repeated several times to ensure sufficient data. The stabilator was fixed at the hover trim value of 40 deg trailing-edge-down during hover and 4 deg trailing-edge-down at 80 kts.

Good low frequency identification was achieved by sufficiently exciting the low frequency dynamics during the frequency sweeps with the SAS and FPS off. Attitude and position perturbations were noticeable to the pilot, but were not large enough to cause difficulty in maintaining stability at the trim condition. Flying with the stability augmentation disengaged improves the quality of the low frequency identification by preventing control correlations caused by feedback. Previous identification of UH-60 low frequency characteristics, particularly in the longitudinal axis, has been limited by availability of SAS-ON data only (ref. 26).

SAS/FPS-OFF low frequency inputs were achieved by modulating the low frequency amplitude of the frequency sweep to prevent large attitude excursions and superimposing pulse type inputs to prevent excursions away from the trim condition. This type of modulation keeps the response in the linear region, helps to maintain trim, eases the task of stabilization, and actually serves to enrich the frequency content of the input. A perfect swept sine wave is neither necessary nor desired.

Instrumentation and data consistency– Control positions were measured with string pots attached to the mechanical control system linkages. Response variables were measured by a Litton LN-93 Inertial Navigation Unit (INU) mounted on the cabin floor. The INU calculates body attitudes, angular rates, specific forces, and inertial velocities from ring laser gyro and accelerometer triads. These data are Kalman-filtered and output to a digital data bus at 256 Hz with minimal phase lag. The control position signals were digitized and merged with the digital output from the LN-93. Anti-alias filtering of the control positions was not necessary because the bandwidth of the potentiometers is significantly lower than the sample rate (ref. 28). Digital output from a GEC Helicopter Air Data Sensor (HADS) system was also recorded onboard. LASER tracking data were recorded during hover by the ground station and merged with the on-board data in a post processing step.

Kinematic consistency of the response variables was checked with the optimal state estimation program SMACK (ref. 29) using the procedure outlined in reference 30. This was done primarily to correct the measurements to the c.g., remove small drifts from the INU calculated velocities, and detect and remove disturbances from the air data. Excellent on-board data consistency and compatibility with the LASER derived inertial velocities was verified.

Frequency response identification– Frequency responses were calculated from the time histories of the angular rate, linear velocity, and linear acceleration responses of the helicopter to each of the four pilot controls. Excellent excitation of the aircraft dynamics in the frequency range of 0.1 to 20 rad/sec was achieved. As a result, 29 of the 36 possible body response frequency responses were included in the stability derivative identification for hover and 30 out of 36 for 80 kts.

[2] 2-3-1-1 multisteps are a series of step type inputs alternating in direction of the input and with relative time durations of two units, three units, one unit, and one unit. The steps are performed sequentially, to form one time record, starting and ending at the trim contol position.

Pitch- and roll-rate frequency responses identified with CIFER® from the flight-test data are shown in figures 4 and 5 for the hover and 80 kts flight conditions respectively. The coherence function indicates the extent to which the output is linearly related to the input. Factors which degrade the coherence function from a maximum value of one are: lack of input excitation, lack of aircraft response, process noise such as gusts, and significant nonlinearities in the dynamics. Coherence values of 0.6 and above are considered acceptable. The coherence function is used as a weighting function by CIFER® in minimizing frequency response errors to determine the values of the parameters in the state space model.

Referring to figure 4, it is evident that excellent identification of the on-axis responses has been achieved in the frequency range of 0.5 to 20 rad/sec. The coherence of the off-axis responses are not as good, but these data definitely supply sufficient information about the coupled response to be used in the stability derivative identification. The p/δ_{lon} response is better identified than the q/δ_{lat} response because there is more roll rate response due to a much smaller aircraft roll moment of inertia. The effects of rotor flapping can be seen in the downward break in the hover q/δ_{lon} and p/δ_{lat} magnitude curves above eight rad/sec, emphasizing the importance of these dynamics in the frequency range for flight control. The lead-lag mode dominates both the magnitude and phase curves of the on-axis frequency responses above 13 rad/sec.

Referring to figure 5, the forward flight results are generally similar to those in hover. A significant difference is that the quality of the frequency responses above 15 rad/sec is not as good. This is probably due to a lack of high frequency inputs since these sweeps were flown by a different pilot. However, the low-frequency identification results are of higher quality than the hover results. It is generally easier to achieve better low-frequency identification in forward flight because it is easier to maintain trim while conducting the frequency sweep.

Identification Results

Hover Yaw/Heave Model

It was desirable to identify a reduced-order model of the UH-60 yaw/heave dynamics in hover in order to reduce the possibility of correlation of the yaw/heave parameters with others in the overall model structure. A seven-state yaw-heave identification model structure was derived from the model of Appendix A as shown in equation (24). Parameter values were identified with CIFER® using flight-test data from the Airloads UH-60 helicopter in hover (ref. 26) since engine/drive train data were not available from the RASCAL flight-test experiment. The governor values identified in reference 4 were fixed in the identification. The induced velocity and other parameters were alternately fixed and freed during the model structure determination to avoid excessive correlation among the parameters.

$$
\begin{bmatrix}
1 & -1 & & & & & \\
 & 1 & & & & & \\
 & & 1 & & & & \\
-\chi & & & 1 & & & \\
 & & & & 1 & & \\
K_D & & & & & \tau_{w_f} & \\
 & & & & & & 1
\end{bmatrix}
\frac{d}{dt}\begin{Bmatrix} \Omega \\ r \\ w \\ \upsilon \\ Q \\ w_f \\ \Psi \end{Bmatrix}
=
\begin{bmatrix}
R_\Omega & & R_w & -R_w & R_Q & & \\
 & N_r & N_w & & N_Q & & \\
Z_\Omega & Z_r & Z_w & -Z_w & & & \\
I_\Omega & & I_w & I_\upsilon & & & \\
 & & & & T_Q & T_{w_f} & \\
K_P & & & & & -1 & K_I \\
1 & & & & & &
\end{bmatrix}
\begin{Bmatrix} \Omega \\ r \\ w \\ \upsilon \\ Q \\ w_f \\ \Psi \end{Bmatrix}
+
\begin{bmatrix}
 & R_{col} \\
N_{ped} & N_{col} \\
Z_{ped} & Z_{col} \\
 & -\kappa Z_{col} \\
 & K_C T_{w_f}
\end{bmatrix}
\begin{Bmatrix} \delta_{ped} \\ \delta_{col} \end{Bmatrix}
\tag{24}
$$

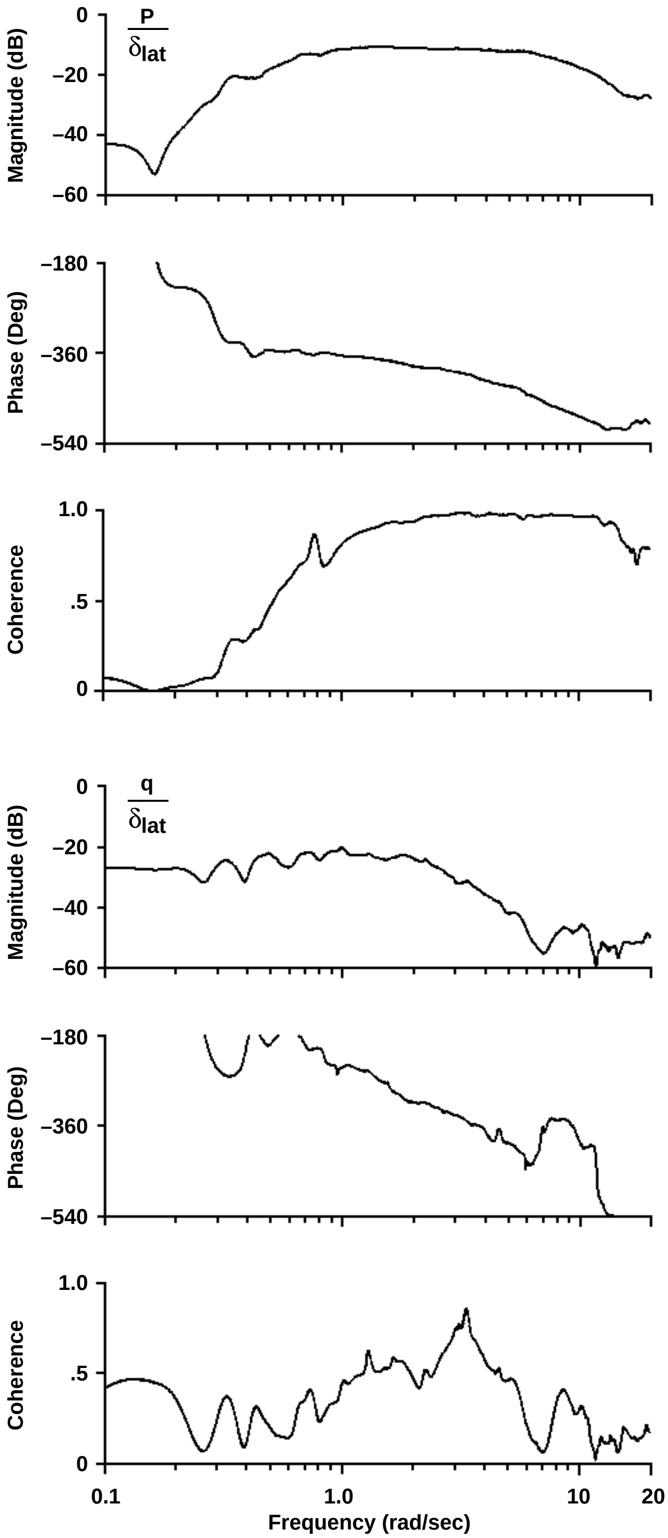

Figure 4. CIFER®–identified UH-60 frequency responses for hover.

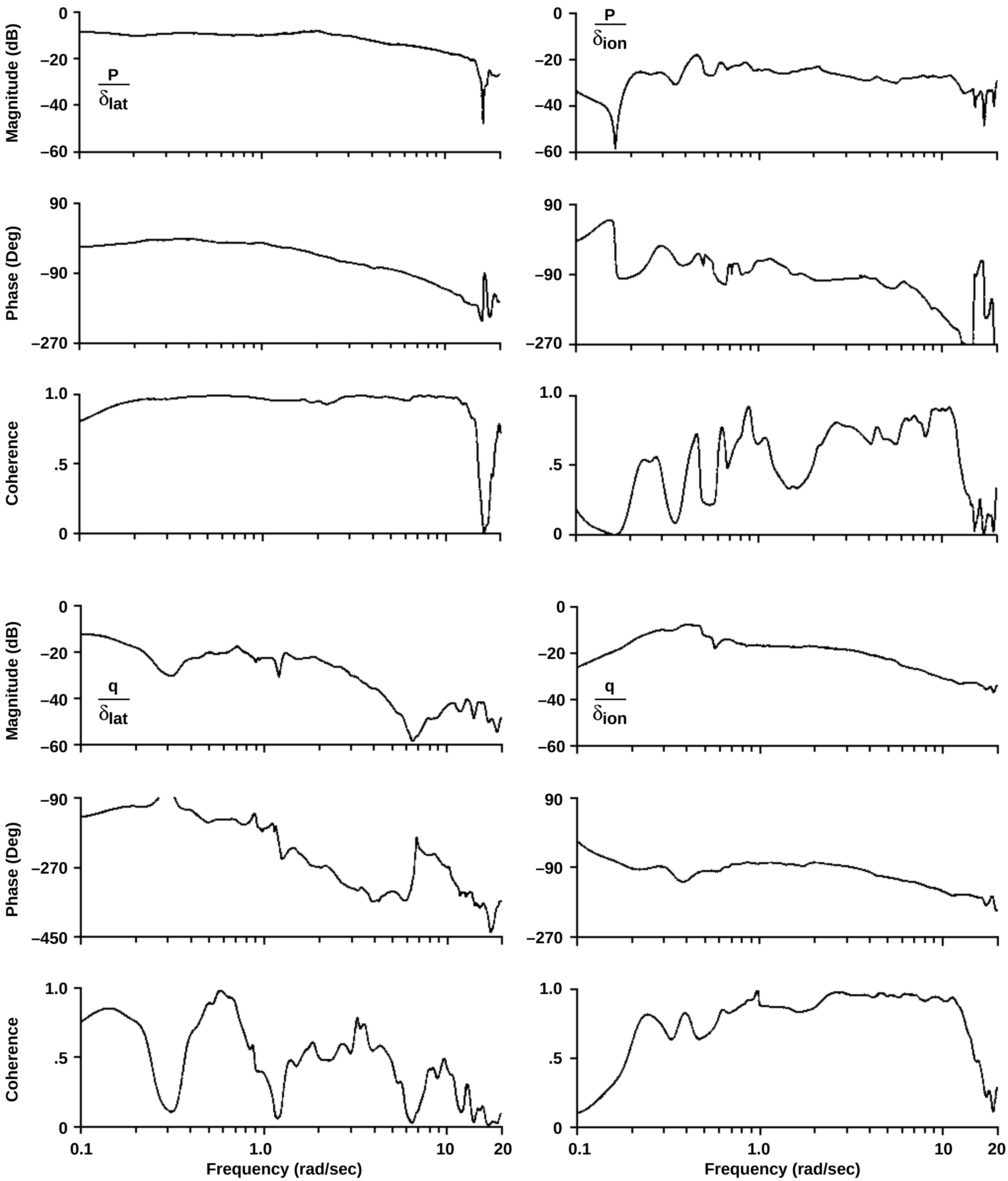

Figure 5. CIFER®–identified UH-60 frequency responses for 80 knots.

The final CIFER® results for the minimally parameterized model are shown in table 1. Cramer–Rao bounds and parameter insensitivities are shown for the final iteration in which the induced velocity parameters were fixed. The Cramer–Rao percentages for R_Ω and R_w are slightly larger than the target value of 20 percent. Further reduction of the model resulted in large increases in the frequency response fit cost functions.

The identified N_Q should be the reciprocal of the aircraft yaw moment of inertia. This leads to an estimate of I_{zz} = 48,060 slug-ft^2 which compares well with the value of 40,000 of BE model A. The damping derivatives identified, R_Ω, Z_w, N_u, I_υ, and T_Q all have very reasonable values. The large value identified for the effective time delay on collective, $\tau_{\delta_{col}}$, reflects the absence of explicit coning dynamics from the seven-state model, the phase effects of which are now modelled by this parameter.

The frequency response comparisons between the yaw/heave model and flight-test data of figure 6 show that the model is accurate in the frequency range of approximately 0.3 to 20 rad/sec. Overall, the match is very good, with the identified model predicting slightly higher closed-loop fuel control bandwidth than measured. The high-frequency vertical acceleration response to collective is fit well by the simple induced velocity model.

Time domain verification of the model with dissimilar flight-test data is shown in figure 7. It verifies a weakness in the initial fuel flow response modeling. The low frequency torque response also requires improvement. However, the rpm, vertical acceleration, and yaw-rate responses are all quite good. The overshoot in the acceleration response indicates accurate modeling of the vertical induced velocity.

Hover Model Identification Results

The results of the seven-state hover yaw/heave identification were incorporated into the overall hover model structure of Appendix A, excluding the lead-lag states. The

Table 1. Yaw/heave identified model parameters

Derivative[a]	Parameter value	Cramer–Rao (%)	Insensitivity (%)	Derivative	Parameter value	Cramer–Rao (%)	Insensitivity (%)
R_Ω	–0.5049	39.30	5.932	T_{wf}	3106.	16.74	1.054
R_w	–0.02419	54.33	3.707	I_Ω	35.40[b]		
R_Q	0.08688	6.897	1.067	I_w	9.254[b]		
R_υ	0.02419[c]			I_υ	–10.65[b]		
$R_{\delta col}$	–0.9644	13.26	0.8510	$I_{\delta col}$	99.85[c]		
Z_Ω	–6.362	22.17	8.825	K_P	–0.0595[b]		
Z_w	–1.096	5.026	1.363	K_I	–0.09090[b]		
Z_υ	1.096[c]			K_C	0.001600[b]		
$Z_{\delta col}$	–16.42	6.349	1.576	$N_{\delta ped}$	0.6426	4.759	2.052
N_r	–0.4452	13.55	5.391	$R_{\delta ped}$	0.0000[d]		
N_Q	0.02170	5.887	2.136	τ_{wf}	0.06700[b]		
$N_{\delta col}$	–0.1258	8.602	3.423	T_Q	–7.847	17.17	1.103
$\tau_{\delta ped}$	0.0000[d]			$\tau_{\delta col}$	0.05689	10.60	4.679

[a]Response units are ft, deg, sec, kilo-lbm, control units are inches.
[b]Fixed value in model.
[c]Fixed derivative tied to a free derivative.
[d]Eliminated during model structure determination.

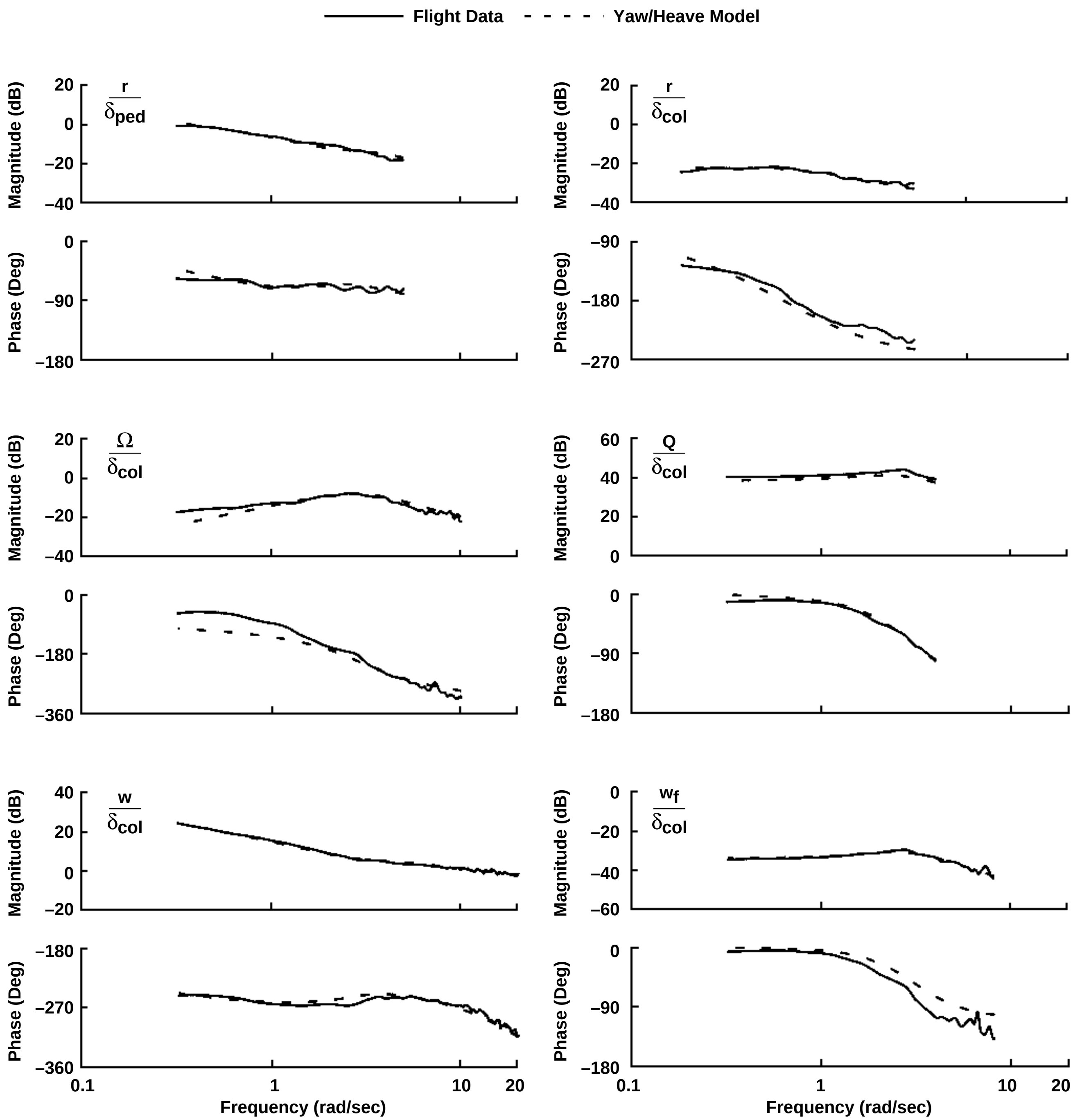

Figure 6. Seven state yaw/heave model responses for hover.

of the q/δ_{lon} and p/δ_{lat} frequency responses up to 20 rad/sec were identified.

The torque, fuel flow, and governor parameters from the seven-state Airloads model were not re-identified in the subsequent RASCAL models. This was considered to be an acceptable approach, since these dynamics should be relatively constant from airframe to airframe.

The equivalent time delays on the control inputs were fixed at a value representative of the hydraulic system delay. Modeling additional delay was not necessary since all of the significant sources of phase lag below 20 rad/sec are explicitly modeled. A value of 0.026 sec was identified from the frequency response of the lateral primary servo shown in figure 8. This agrees very well with the value of 0.024 identified by Ballin (ref. 26) for the Airloads UH-60.

The rigid body parameters of the model of reference 9 were used for startup of the hover model identification. The rotor parameters were also set at theoretical values for startup. Theoretical values for $I_{\dot{a}_0}$ and $R_{\dot{a}_0}$ were added since they were not identified in the seven-state formulation. The rpm and induced velocity dynamics were then re-optimized to account for the effects of coupling with coning. All of the rpm and induced velocity parameters were then fixed for the remainder of the model identification. The model structure was reduced as

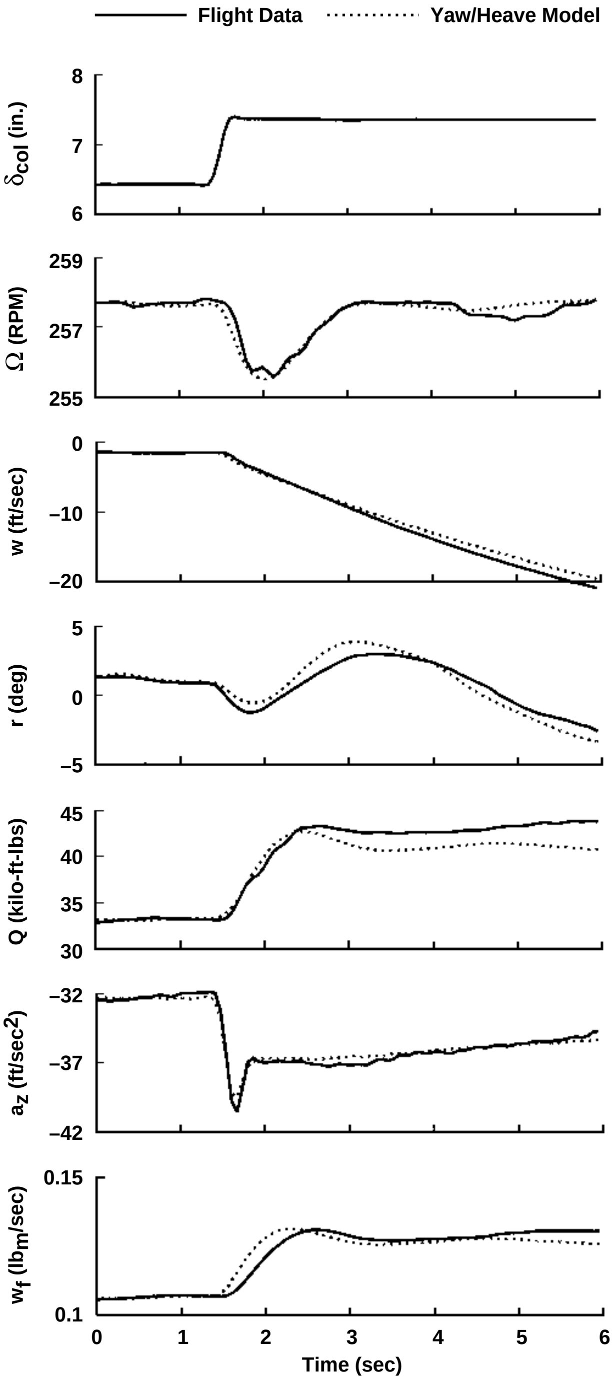

Figure 7. Yaw/heave model time responses.

resulting model was fit to 29 RASCAL frequency responses and the rpm and torque-frequency responses from the Airloads database. The pitch and roll angular-rate responses were fit up to 12 rad/sec, at which point the first effects of the lead-lag mode are seen. The hover model parameters were then fixed at their final values and the lead-lag dynamic parameters which optimized the fits

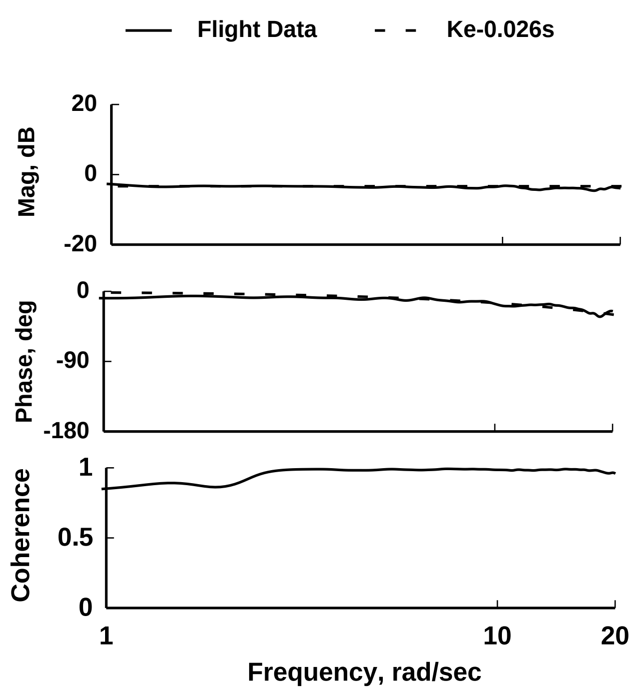

Figure 8. Lateral primary servo frequency response model.

previously described to achieve a minimally parameterized hover model.

Parameter values– The CIFER®-identified stability and control derivative values, Cramer–Rao bounds (as a percentage of parameter value), and parameter insensitivities for the hover model are presented in table 2. Almost all of the parameters remaining after the model structure reduction have error metric values at the target values or below.

X_u, Y_v, M_u, and Z_w are well-identified low frequency speed stability derivatives although the negative sign of M_u is counter to first principles quasi-steady theory. The sign difference may be due to the dynamic nature of the identification process versus the quasi-steady analysis. Negative values of M_u have also been reported in previous identification studies of the UH-60 (ref. 9) and AH-64 (ref. 24). The overall dynamics of the model are not adversely affected by the apparent sign discrepancy in any case.

N_{b_1} and $Z_{\delta_{lon}}$ were added to the hover model structure to improve the overall fit of the model although they were not predicted in the model structure development process. These parameters appear to be crucial to the identification and may be accounting for interactional aerodynamics between the main rotor and the tail rotor or tail boom.

For small flapping angles we expect $L_{b_1} / M_{a_1} \approx I_{YY} / I_{XX}$. The identified ratio of $L_{b_1} / M_{a_1} = 9.32$ is somewhat larger than the value of I_{YY}/I_{XX} = 7/14 used in BE Model A. The identified value of N_Q implies an estimated value of I_{ZZ} = 56,850, compared with I_{ZZ} = 40,000 for BE Model A. These discrepancies are not disturbing however, since aircraft moments of inertia are notoriously difficult to measure and are often adjusted in simulation models to improve correlation with flight-test data.

The lead-lag canonical parameters and dipole transfer functions are tabulated in table 3. This auxiliary identification extends the frequency range of the model from approximately 10 to 20 rad/sec. The effects are most noticeable in the on-axis angular frequency response plots which follow.

The identified rotor flapping parameters are compared with theoretical values in table 4. The identified Lock number and blade mass moment ratio are reasonably close to theoretical results. A stable value of pitch-flap coupling is identified which contributes significantly to the measured response. The aerodynamic phase lag is large (ψ_a = 39 deg) and indicates that a significant correction to the classical flapping equations is required to match the off-axis response in hover.

Effect of aerodynamic phase lag– Figure 9 shows the effect of the aerodynamic phase lag on the identified model. The figure compares the off-axis roll rate response to longitudinal cyclic input for the identified model with aerodynamic phase lag of ψ_a = 39 deg and a baseline case of ψ_a = 0 deg to the flight-identified results. Including the aerodynamic phase lag is seen to greatly improve the correlation of the off-axis response.

Frequency response comparisons– Figure 10 compares the on-axis roll rate frequency response to lateral cyclic of the identified model, linearized versions of BE Models A and B (refs. 4 and 3), and the flight-test data. The identified model fit is good up to 20 rad/sec, well into the frequency range dominated by the regressing flap and lead-lag modes. The lead-lag mode is quite evident in the 15 to 20 rad/sec frequency range and is matched well by the identified model. The linearized BE models are both deficient in capturing the frequency of the lead-lag mode.

Figure 11 shows a significant improvement in the fit of the off-axis p/δ_{lon} response over that of BE Models A and B. The simulation models have considerable phase error in this response, which is typical of current rotorcraft flight dynamics models. The identified model accurately describes the coupled response well up to six rad/sec. Identification above six rad/sec is not possible due to low coherence, which probably indicates a lack of any significant response in this frequency range.

Figures 12 and 13 show that the identified hover model captures the important yaw/heave coupling characteristics of the UH-60 in hover. Both the identified model and BE Model B include rpm and engine/governor dynamics which are clearly needed to match the r/δ_{col} response. However, only the flight identified model matches the a_z/δ_{ped} data in figure 13. This indicates that some other phenomenon may be modeled in the identification, which is not included in either of the simulation models.

The remaining frequency responses of the identified hover model are compared with those derived from flight-test data in Appendix B. All of the frequency responses used in the identification are shown. In general, the model fits the data very well. In particular, the on-axis angular-rate responses to cyclic are very accurate in the frequency range required for high bandwidth control, and the coupling behavior is very well modeled.

Eigenvalues– The eigenvalues of the hover model are tabulated with those of the linearized BE Models A and B in table 5. A one-to-one comparison of the resulting modes is difficult because each model contains a different set of dynamics. For example, the vertical aerodynamic lag state couples with the collective coning in the identified model creating four eigenvalues with frequencies

Table 2. 15 DOF identified hover model parameters

Derivative[a]	Parameter value	Cramer–Rao (%)	Insensitivity (%)
X_u	–0.04430	17.31	8.123
X_v	0.0000[d]		
X_w	0.0000[d]		
X_p	0.0000[d]		
X_q	0.0000[d]		
X_r	0.0000[d]		
X_{a_1}	–32.17[b]		
X_{θ_o}	16.94	5.012	2.308
$X_{\theta_{tr}}$	0.0000[b]		
Y_u	0.0000[d]		
Y_v	–0.2193	15.40	5.510
Y_w	0.0000[d]		
Y_p	1.820	13.58	4.769
Y_q	0.0000[d]		
Y_r	1.496	27.57	13.16
Y_{b_1}	32.17[b]		
Y_{θ_o}	0.0000[d]		
$Y_{\theta_{tr}}$	28.66	3.088	1.414
Z_u	0.0000[d]		
Z_v	0.0000[d]		
Z_w	–0.7164	10.44	2.406
Z_p	0.0000[d]		
Z_q	–2.006	20.25	9.616
Z_r	2.290	8.700	3.572
Z_{a_o}	53.41[c]		
$Z_{\dot{a}_o}$	20.64	13.77	4.347
Z_{Ω}	–1.483	20.18	7.635
Z_{υ}	0.7164[c]		
Z_{θ_o}	–389.7	5.456	1.225
$Z_{\theta_{tr}}$	9.328	7.954	3.029
L_u	0.04090	14.45	5.134
L_v	0.0000[d]		
L_w	0.0000[d]		
L_p	0.0000[d]		
L_q	0.0000[d]		
L_r	0.0000[d]		
L_{b_1}	48.65	2.984	1.080
L_{θ_o}	–3.679	13.85	4.045
$L_{\theta_{tr}}$	6.183	5.217	1.494
M_u	–0.01406	12.48	4.313
M_v	0.007714	13.56	5.446
M_w	0.0000[d]		
M_p	0.0000[d]		
M_q	0.0000[d]		
M_r	–0.1697	12.10	4.199

Table 2. Continued

M_{a_1}	5.221	1.763	0.7622
M_{θ_o}	3.780	9.025	2.903
$M_{\theta_{tr}}$	–2.541	3.091	1.177
N_u	–0.01870	15.38	4.921
N_v	0.0000[d]		
N_w	–0.01246	20.07	4.191
N_p	0.0000[d]		
N_q	–0.3676	12.05	4.743
N_r	–0.4444	9.175	3.237
N_{b_1}	4.491	4.963	2.395
N_{a_o}	–0.4433[c]		
$N_{\dot{a}_o}$	0.0000[d]		
N_Q	0.01759	6.437	2.030
N_Ω	0.0000[d]		
N_υ	0.01246[c]		
N_{θ_o}	3.235	16.38	3.346
$N_{\theta_{tr}}$	–7.021	4.088	1.018
C_{a_o}	–758.2[c]		
$C_{\dot{w}}$	–0.03025[c]		
A_p	–56.16[c]		
A_{a_1}	–29.21[c]		
B_q	56.16[c]		
B_{b_1}	–29.21[c]		
c_w	–1.345[c]		
c_{a_o}	101.0[c]		
$c_{\dot{a}_o}$	25.48[c]		
c_υ	1.345[c]		
c_{θ_o}	–737.0[c]		
a_q	17.43[c]		
a_{a_1}	64.52[c]		
a_{b_1}	439.5[c]		
$a_{\dot{a}_1}$	16.28[c]		
a_{A_1}	–470.8[c]		
b_p	17.43[c]		
b_{a_1}	–439.5[c]		
b_{b_1}	64.52[c]		
$b_{\dot{b}_1}$	16.28[c]		
b_{B_1}	–470.8		
$R_{\dot{a}_o}$	2.988[b]		
R_Ω	–0.3331[b]		
R_Q	0.1074[b]		
R_{θ_o}	–32.20b		
I_w	12.44[b]		
$I_{\dot{a}_o}$	–197.3b		
I_υ	–17.03b		

Table 2. Concluded

I_Ω	20.02b		
γ	8.621	2.094	0.7967
M_β/I_β	0.03205	31.38	4.308
ψ_a	0.6177	15.01	5.898
δ_3	0.1470	9.139	1.293
$Z_{\delta_{lon}}$	1.153	3.218	1.577

[a]Response units are ft, deg, sec, kilo-lbm, control units are inches.
[b]Fixed value in model.
[c]Fixed derivative tied to a free derivative.
[d]Eliminated during model structure determination.

Table 3. Hover lead-lag parameters

Parameter	Value
pp	1.241
x1p	–1.560
x2p	–75.12
x21	–356.1
x22	–6.617
qq	1.482
x3q	–1.890
x4q	–161.9
Roll dipole	[0.1682,16.95]/[0.1753,18.87]
Pitch diplole	[0.1737,16.50]/[0.1753,18.87]

Table 4. Comparison of theoretical and identified flapping parameters

Parameter	Identified value	Theoretical value[a]
γ	8.62	8.06
M_β/I_β	0.0321	0.0573
δ_3	7.84 deg	0.0
ψ_a	38.8 deg	N.A.

[a]From GenHel UH-60 simulation model documentation.

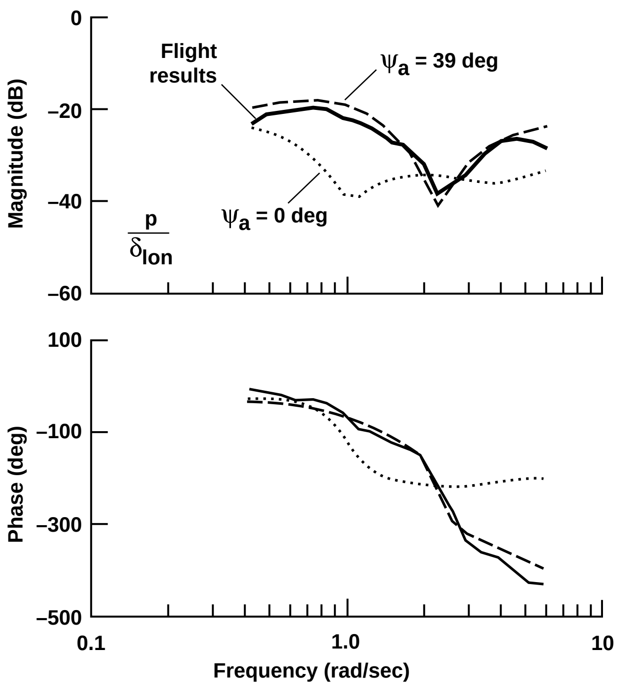

Figure 9. Effect of aero phase lag on identification.

bracketing the frequencies of the BE model coning modes. The lower frequency rpm modes are comparable between the identified model and BE Model B. However, the collective lag couples extensively with the higher frequency engine/governor dynamics in BE Model B, modifying the torque and fuel flow modes. The coupling between the body roll and pitch and regressing flapping is tighter in the BE models making comparison with the identified regressing flap mode difficult. However, there is reasonable agreement between all of the models for the regressing lead-lag, progressing flap, and rigid body modes.

Time domain comparison and verification– Time domain verification of the identified model with dissimilar flight-test data is illustrated for the four control axes in figure 14. In general, the model compares very well with the flight-test measured responses. Both the on- and off-axis responses to cyclic inputs are well predicted in agreement with the frequency response results.

Some minor discrepancies include the yaw-rate and vertical-acceleration responses to lateral cyclic, the yaw

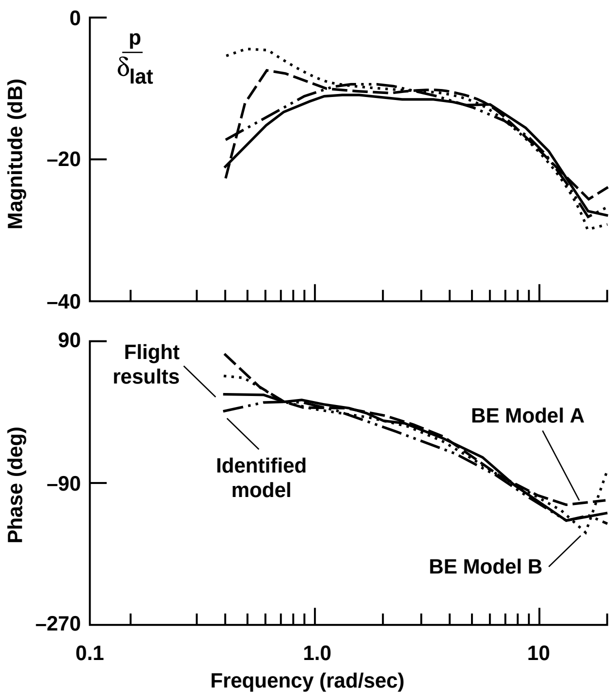

Figure 10. Comparison of p/δ_{lat} frequency responses in hover.

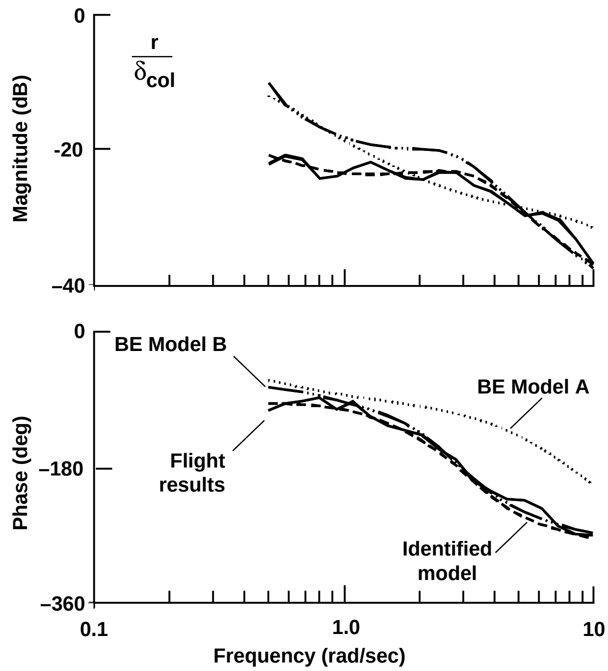

Figure 12. Comparison of r/δ_{col} frequency responses in hover.

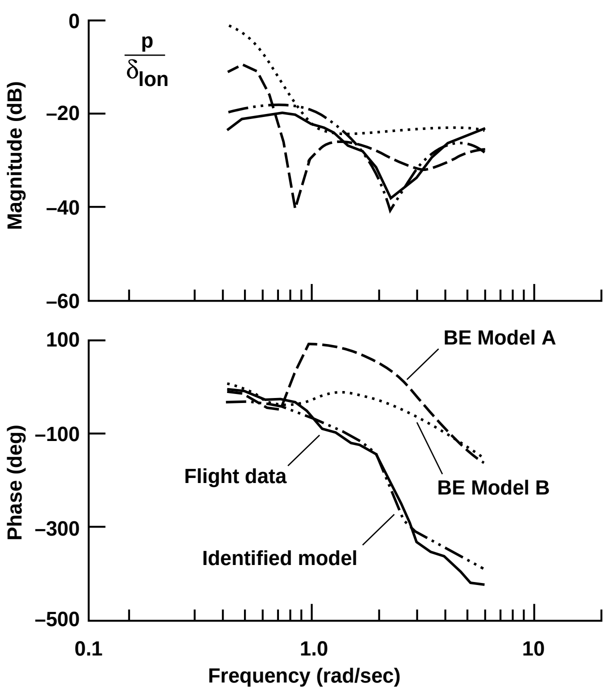

Figure 11. Comparison of p/δ_{lon} frequency responses in hover.

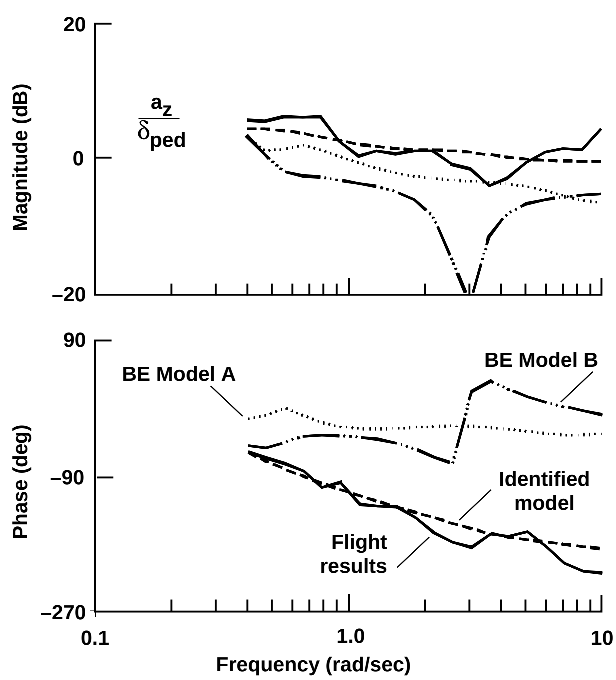

Figure 13. Comparison of a_z/δ_{ped} frequency responses in hover.

Table 5. Comparison of hover model eigenvalues

Description	Identified value	BE Mod A (ref. 3)	BE Mod B (ref. 4)
Heave/inflow	(0.2317)		
Heave/yaw		[0.999,0.231]	[0.645,0.164]
Lat transl/yaw	[0.927,3.94]		
Lateral translation		[0.249,0.544]	[0.321,0.546]
Long translation	[–0.998,0.449]	[–0471,0.486]	[–0.481,0.225]
Pitch	[0.644,1.01]	(1.3479)	(0.801)
rpm	(2.6575)		(1.81)
rpm/fuel flow	[0.512,3.40]		[0.465,2.83]
Roll	(3.7538)		
Pitch/long flap		(4.8290)	(5.57)
Roll/lateral flap		[0.609,5.37]	[0.669,5.40]
Regressing flap	[0.601,10.3]		
Collective lead–lag		[0.725,7.88]	
Collective inflow		(19.348)	
Fuel flow/torque	(16.9998)		
Torque/collec lag			(8.15)
Con/torq/coll lag			(14.1)
Coll lag/rpm/fuel			[0.935,24.7]
Regr lead–lag	[0.175,18.9]	[0.210,20.1]	[0.164,18.5]
Cyclic inflow		[0.993,24.7]	[0.987,28.8]
Coning/aero lag	[0.819,23.7]		
Coning		[0.332,26.0]	[0.340,26.8]
Coning/aero lag	[0.316,34.6]		
Progr lead–lag		[0.163,37.6]	[0.120,39.2]
Progressing flap	[0.145,50.2]	[0.180,52.1]	[0.239,51.1]

rate response to longitudinal cyclic, the roll response to pedals, and the lateral acceleration response to collective. With the exception of roll rate due to pedals, the frequency response data corresponding to these input/output pairs used in the identification were not ideal. The vertical acceleration due to lateral cyclic and lateral acceleration due to collective frequency responses were not included, and the yaw rate due to longitudinal cyclic has relatively low coherence. The yaw rate response to lateral cyclic frequency response has good coherence only for relatively high frequencies which is reflected in the time domain as well. The weaknesses are therefore understandable in terms of a lack of good frequency response data for these transfer functions.

80 Kts Identification Results

The model structure of Appendix A, minus the lead-lag dynamics was used as a starting point for the 80 kts parametric identification. Startup values for the rigid body parameters were obtained from a linearized version of BE Model A at 80 kts, and startup values for the flapping parameters were obtained from the hover identification. The induced velocity and rpm parameters were fixed at theoretical values for the new flight condition, and the fuel flow, torque, and governor parameters were again fixed at the seven-state identification model values.

It was desirable to remove the inflow, engine, fuel flow, and governor dynamics from the forward flight formulation since it was expected that they would not contribute significantly to the aircraft response. In particular, it was anticipated that the yaw/heave coupling through the drive train torque reaction would be overshadowed by the main rotor/tail rotor/fuselage interactional aerodynamics. Inflow effects are also much less significant at this flight condition. Removal of these dynamics from the model had almost no effect on the fit to the 80 kts data and was therefore adopted for the remainder of the model structure reduction procedure.

It was immediately evident that reasonable values for the Lock number and ratio M_β/I_β could not be identified from the 80 kts flight data. This is somewhat understandable since the effects of rotor flapping are more correlated with the effects of other aircraft aerodynamics such as the horizontal tail in forward flight. These rotor parameters, which should be invariant with flight condition, were therefore fixed at the hover identified values. This produced a minimal decrease in fit quality of the model which was deemed acceptable. The model structure

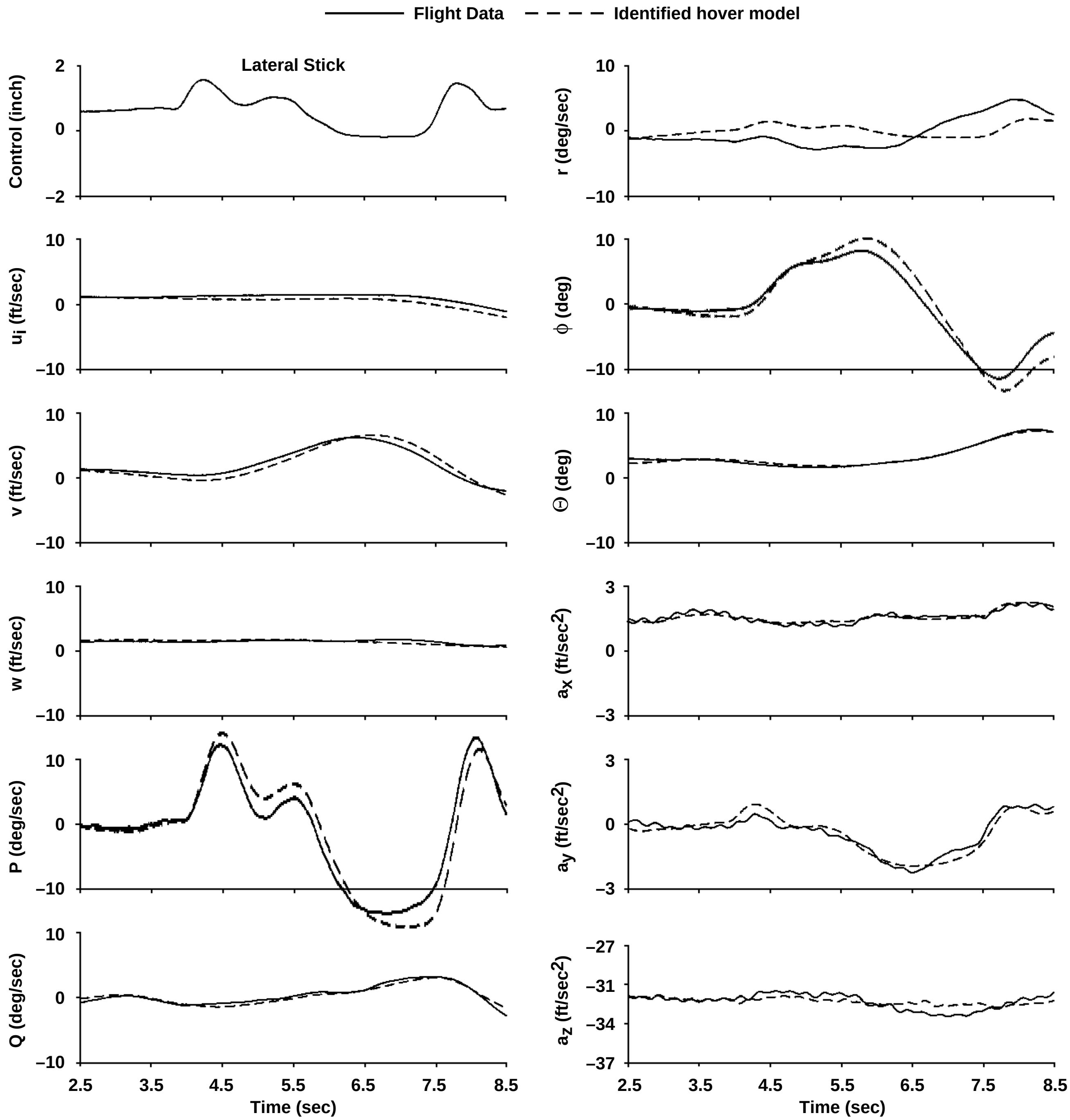

Figure 14. (a) Comparison of model time responses at hover.

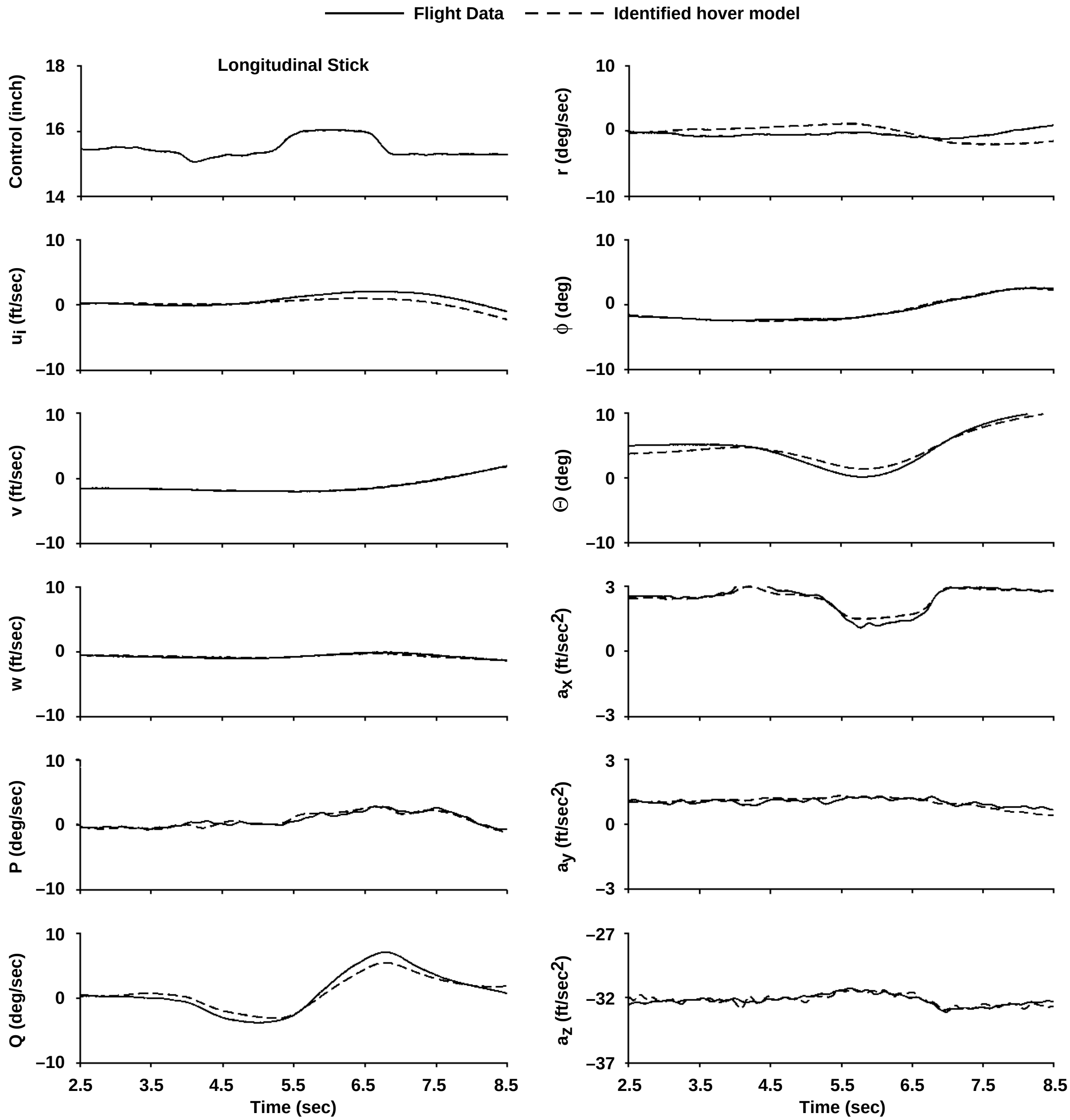

Figure 14. (b) Continued.

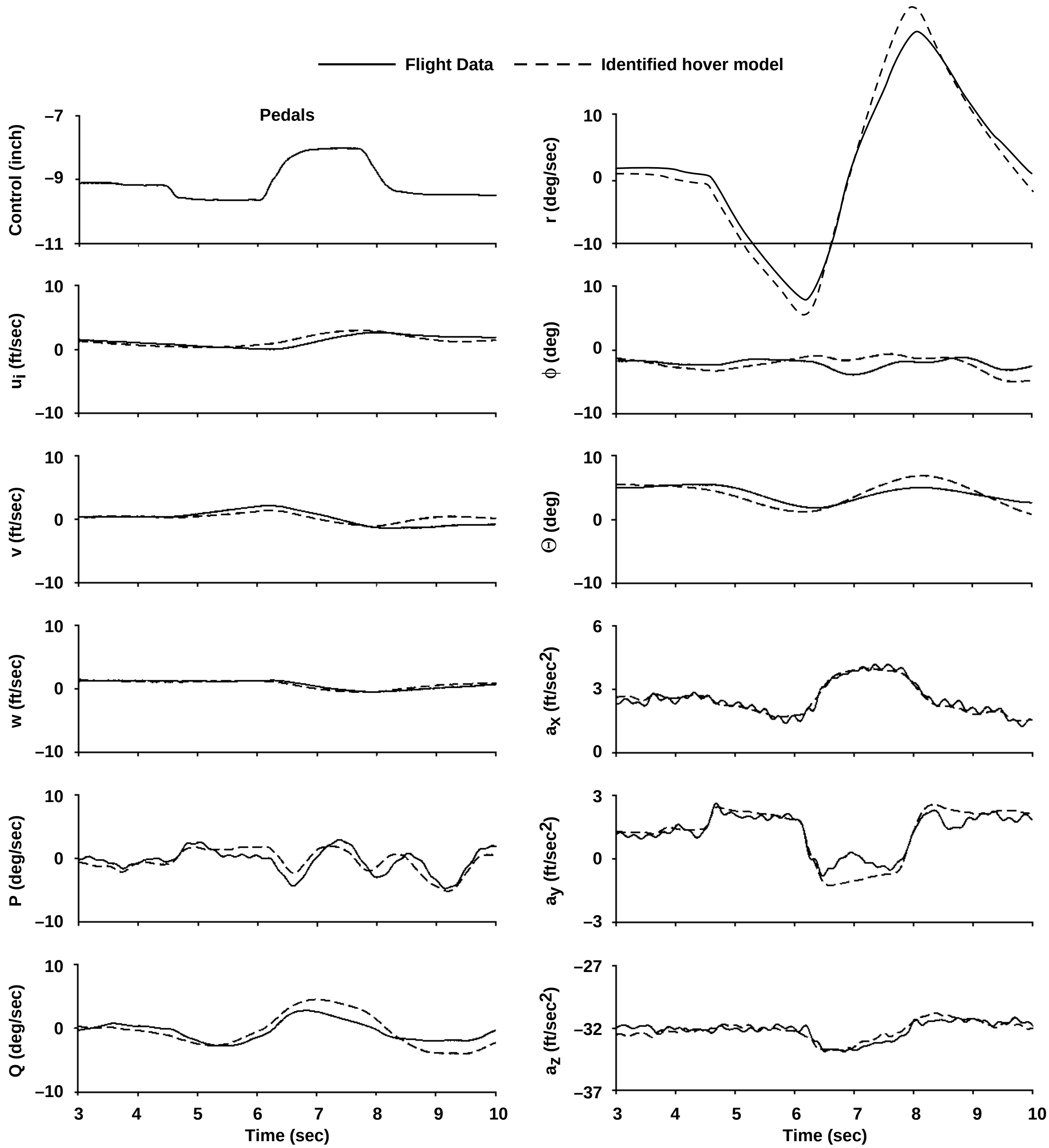

Figure 14. (c) Continued.

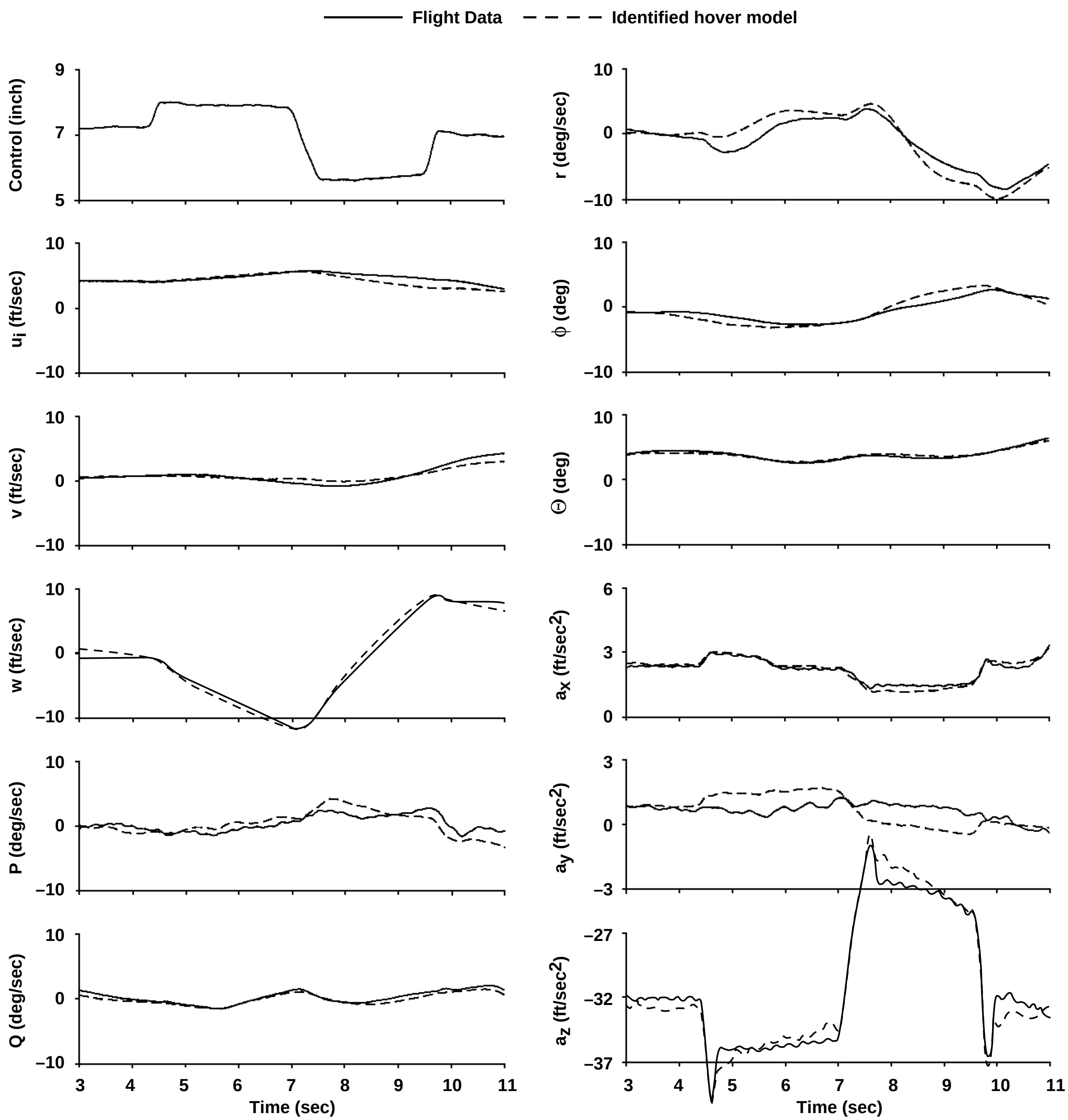

Figure 14 (d) Concluded.

reduction then continued until a minimally parameterized 80 kts model was achieved.

Parameter values– The CIFER®-identified stability and control derivative values, Cramer–Rao bounds (as a percentage of parameter value), and parameter insensitivities for the identified 80 kts model are presented in table 6. The model structure reduction was halted when further elimination of parameters caused an unacceptable increase in the frequency response fit cost function. Using this criterion, neither Y_q nor L_r could be removed from the model, although their error metrics are slightly higher than the target values.

The number of parameters in the 80 kts model is larger than in the hover model due to a greater level aerodynamic complexity in the forward flight condition. For example, M_p is a more significant parameter at 80 kts, reflecting the additional pitch damping effectiveness of the stabilator in forward flight.

Many additional terms appear in the flapping equations in forward flight including response coupling terms and additional control power and flapping spring terms. Many of these terms were fixed in the identification though constraint to the fixed Lock number and some were constrained to the pitch/flap coupling.

The 80 kts identified moment ratio $L_{b_1}/M_{a_1} = 7.49$ is closer to the inertia ratio $I_{YY}/I_{XX} = 7.14$ used in BE Model A than the value $L_{b_1}/M_{a_1} = 9.32$ identified in hover.

The important rotor flapping parameters identified for 80 kts are compared with the values identified for hover in table 7. With the Lock number and ratio M_β/I_β fixed, the pitch/flap coupling and aerodynamic phase lag were well identified. The value of pitch-flap coupling is similar to that identified in hover, as expected. However, a much smaller value of the aerodynamic phase lag is identified for 80 kts. Since the exact mechanism of this effect is not known, it is not possible to comment on the adequacy of this result, but similar trends have been seen in simulation studies of the AH-64.

The lead-lag canonical parameters and dipole transfer functions identified for 80 kts are tabulated in table 8. This auxiliary identification extends the frequency range of the model from approximately 10 to 20 rad/sec. The effects are most noticeable in the on-axis angular frequency response plots which follow. It is interesting to note that the zeros are now at lower frequencies than the poles (a stabilizing effect) which is opposite from the hover results. The identified lead-lag regressing mode is also at lower frequency for this flight condition than in hover.

Frequency response comparisons– Several frequency responses of the identified model are compared with those of BE Model A and flight-test data at the 80 kts flight condition in figure 15. The identified model fits both the on-axis and off-axis responses much better than does the linearized simulation model. Of particular interest is the mismatch between BE Model A and the flight-test data below 3 rad/sec. Although this frequency range is not as critical for the FCS design application, the errors are very significant, even for the on-axis. Improved modeling of the lead-lag dynamics by the identified model is evident in the roll rate response to lateral cyclic frequency response plot between 10 and 20 rad/sec. Discrepancies between the BE model and flight are not as large for the yaw and heave responses as for hover which is likely to be due to the decreased importance of coupling through the drivetrain in forward flight. However, the identified model is still far superior, particularly for the prediction of yaw rate due to collective.

The remaining frequency responses of the identified 80 kts model are compared with those derived from flight-test data in Appendix C. All of the frequency responses used in the identification are shown. In general, the model fits the data very well. In particular, the on-axis angular-rate responses to cyclic are very accurate in the frequency range required for high bandwidth control, and the coupling behavior is very well modeled.

Eigenvalues– The eigenvalues of the Identified 80 kts model are tabulated with those of the linearized BE Model A in table 9. Also tabulated are the flap, lag, and inflow mode eigenvalues from the identified and BE hover models. Again, a one-to-one comparison of the resulting modes is difficult because each model contains a different set of dynamics. For example, the identified model does not contain explicit inflow dynamics at 80 kts, which is reflected in the difference in the coning and regressing flapping mode frequencies between the two 80 kts models. The BE model also contains the differential flap and lead-lag modes, although they are only weakly coupled with the other rotor modes.

The progressing flap, pitch, roll, phugoid, and dutch roll modes are similar for the identified model and the BE model at 80 kts. The regressing lead-lag mode modal frequency is again underpredicted by the BE model, and this time, the damping is also very underpredicted. This is evident in the frequency response comparison of figure 15 as well. There is an explicit modal expression of the coupling between the roll and regressing lead-lag in the identified model which does not appear in the BE model.

Table 6. Identified 80 kts model parameters

Derivative[a]	Parameter value	Cramer–Rao (%)	Insensitivity (%)
X_u	–0.04985	9.348	3.366
X_v	0.0000[d]		
X_w	0.03199	15.40	4.645
X_p	0.0000[d]		
X_q	0.0000[d]		
X_r	1.495	22.98	9.451
X_{a_1}	–32.17b		
X_{θ_o}	34.74	3.883	1.275
$X_{\theta_{tr}}$	4.563	15.41	5.423
Y_u	0.05161	20.01	1.719
Y_v	–0.1601	5.579	0.9162
Y_w	–0.03226	22.65	4.498
Y_p	0.0000[d]		
Y_q	1.973	47.01	13.95
Y_r	3.861	18.59	5.496
Y_{b_1}	32.17[b]		
Y_{θ_o}	0.0000[d]		
$Y_{\theta_{tr}}$	23.16	5.986	1.817
Z_u	0.2303	19.49	1.437
Z_v	–0.1307	28.03	4.404
Z_w	–1.147	5.177	0.4414
Z_p	21.43	15.84	2.464
Z_q	0.0000[d]		
Z_r	0.0000[d]		
Z_{a_o}	76.31[c]		
Z_{a_1}	–73.38	24.05	2.680
Z_{b_1}	166.2	28.63	4.218
$Z_{\dot{a}_o}$	20.71	9.368	3.308
$Z_{\dot{b}_1}$	0.0000[d]		
Z_{B_1}	61.73	25.28	3.414
Z_{θ_o}	–444.9	3.293	0.5368
$Z_{\theta_{tr}}$	0.0000[d]		
L_u	0.01012	14.04	2.167
L_v	0.0000[d]		
L_w	–0.04281	5.200	0.8300
L_p	0.0000[d]		
L_q	1.835	8.493	2.689
L_r	–0.4431	33.20	10.22
L_{b_1}	54.13	3.707	0.9530
L_{θ_o}	–8.412	5.330	1.488
$L_{\theta_{tr}}$	6.888	5.138	1.365
M_u	–0.005802	16.32	0.9979
M_v	0.01359	5.544	0.7490
M_w	0.005361	13.98	1.676
M_p	–0.3154	7.933	2.783
M_q	–0.7140	9.629	2.247

Table 6. Continued

M_r	–0.4201	13.21	3.169
M_{a_1}	7.222	3.460	0.7736
M_{θ_o}	3.743	5.325	0.8434
$M_{\theta_{tr}}$	–2.353	7.297	1.182
N_u	0.003419	26.95	2.066
N_v	0.0100	7.041	1.124
N_w	–0.02141	4.394	0.4968
N_p	0.3240	12.52	2.809
N_q	0.0000[d]		
N_r	–1.232	4.799	1.247
N_{a_o}	–0.5507[c]		
N_{a_1}	–14.36	8.537	0.4591
N_{b_1}	5.305	7.400	2.014
$N_{\dot{a}_o}$	0.0000[d]		
$N_{\dot{b}_1}$	0.0000[d]		
N_{B_1}	–9.13	13.42	0.7489
N_{θ_o}	3.210	16.41	1.421
$N_{\theta_{tr}}$	–3.660	4.738	0.9418
C_{a_o}	–758.2[c]		
$C_{\dot{w}}$	–0.03025[c]		
A_p	–56.16[c]		
A_{a_1}	–29.21[c]		
B_q	56.16[c]		
B_{b_1}	–29.21[c]		
c_w	–1.345[c]		
c_p	–3.608[c]		
c_{a_o}	141.8[c]		
c_{a_1}	–7.322[c]		
c_{b_1}	–33.54[c]		
$c_{\dot{a}_o}$	25.48[c]		
$c_{\dot{b}_1}$	–3.337[c]		
c_{B_1}	194.8[c]		
c_{θ_o}	–765.3[c]		
a_q	27.29[c]		
a_{a_o}	–194.8[c]		
a_{a_1}	139.3[c]		
a_{b_1}	702.2[c]		
$a_{\dot{a}_1}$	25.48[c]		
a_{A_1}	–751.1[c]		
b_p	27.29[c]		
b_{a_o}	–67.08[c]		
b_{a_1}	–673.7[c]		
b_{b_1}	144.2[c]		
$b_{\dot{a}_o}$	–6.674[c]		
$b_{\dot{b}_1}$	25.48[c]		

Table 6. Concluded

$^{b}B_1$	–779.5[c]		
$^{b}\theta_o$	–389.7[c]		
ψ_a	0.2453	8.620	2.880
δ_3	0.1722	3.931	1.064

[a]Response units are ft, deg, sec, kilo-lbm, control units are inches.
[b]Fixed value in model.
[c]Fixed derivative tied to a free derivative.
[d]Eliminated during model structure determination.

Table 7. Comparison of identified rotor parameters at hover and 80 kts

Parameter	Identified value	Theoretical value
γ	8.62	8.62
M_β/I_β	0.0321	0.0321
δ_3	7.84 deg	9.86 deg
ψ_a	38.8 deg	15.1 deg

Table 8. Lead-lag parameters for 80 kts

Parameter	Value
pp	0.9467
x1p	–2.435
x2p	29.94
x21	–284.4
x22	–6.072
qq	0.9313
x3q	–0.5532
x4q	22.93
Roll Dipole	[0.1010,17.33]/[0.1801,16.87]
Pitch Diplole	[0.1667,17.47]/[0.1801,16.87]

The dynamic mode introduced by the aerodynamic phase lag is at a higher frequency for the 80 kts flight condition since the aerodynamic phase lag is smaller. It still couples with the coning, raising the frequency of it’s modal frequency, but not as tightly as in hover.

Time domain comparison and verification– Time domain verification of the identified model with dissimilar flight-test data is illustrated for the four control axes in figure 16. In general, the model compares very well with the flight-test measured responses. The on- and off-axis pitch and roll responses to cyclic inputs are well predicted in agreement with the frequency response results. Some minor discrepancies include the velocity responses to lateral cyclic, the low frequency roll response to longitudinal cyclic, the roll response to pedals, and the lateral velocity response to collective.

The prediction of the velocity responses to lateral cyclic is diminished in quality because high quality velocity frequency responses for the lateral cyclic inputs were not available for use in the derivative identification. Acceleration responses were available for the x- and y-body axes which allows the model to predict these higher frequency responses well.

The roll response to longitudinal cyclic shows some low frequency error, but the high frequency component is well modeled. Low frequency errors in the model are not of concern because they will be washed out by the flight control system.

Problems with the roll response to pedals were seen in the frequency domain during the identification. The model structure is not adequate to capture this coupled response well. Since it is seen only in forward flight, the discrepancy may be the result of tailplane interactions with the main rotor wake. It may be possible to model the effect with additional states.

The poor lateral-velocity response to collective is partially due to the exclusion of this frequency response from the identification and is also a frequency dependent error. The lateral acceleration is much better predicted.

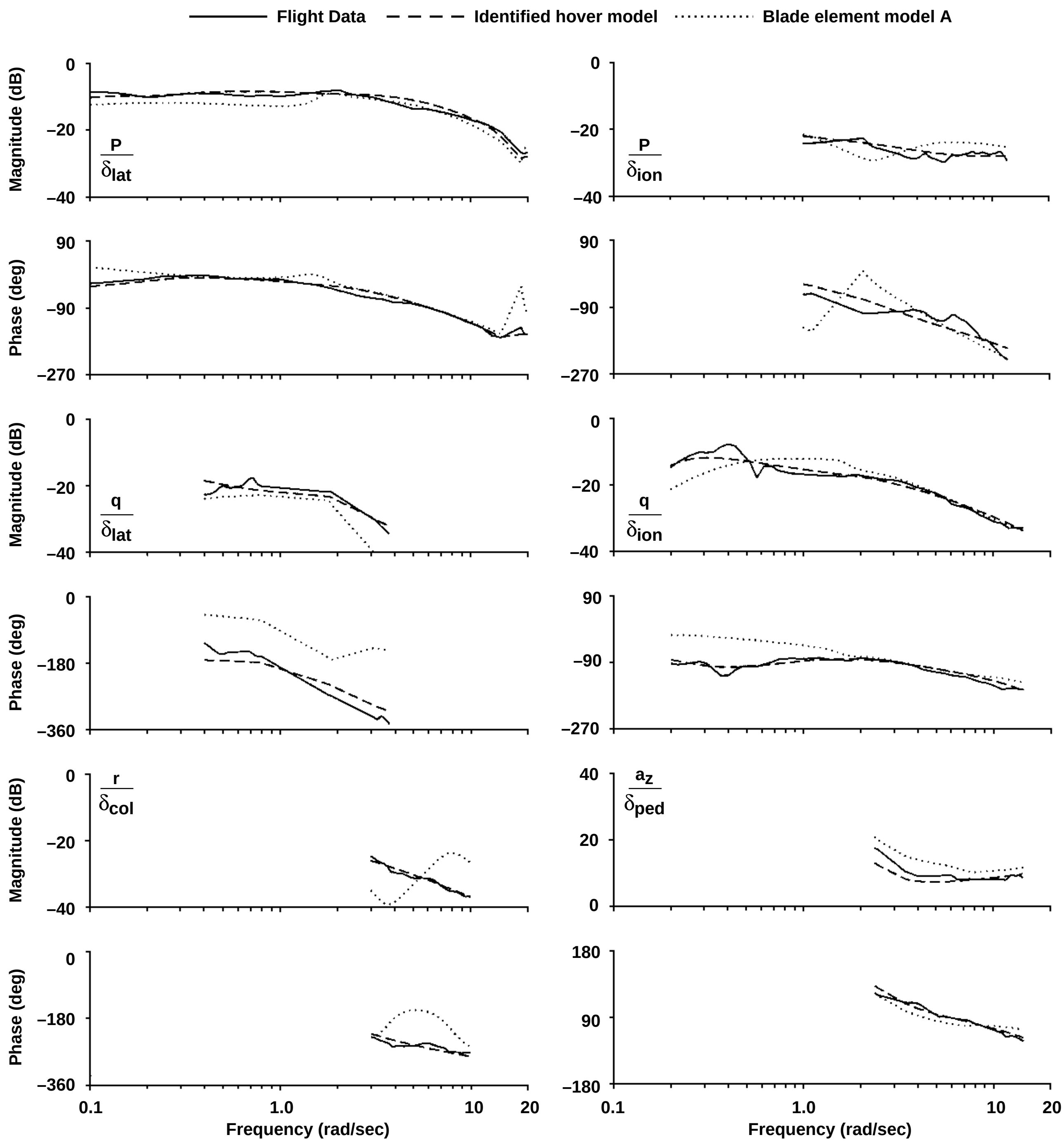

Figure 15. Comparison of model frequency responses at 80 Kts.

Table 9. Comparison of 80 kts model eigenvalues

Description	Identified 80 kts value	Identified hover value	BE Model A 80 kts value	BE Model A hover value
Roll	(–0.0668)		(0.0416)	
Pitch	(–0.499)		(–0.337)	
Phugoid	[0.562,0.231]		[0.899,0.426]	
Dutch roll	[0.448,1.75)		[0.193,1.70]	
Pitch/long flap				(4.8290)
Roll/regressing lag	(–2.75)			
Roll/regressing lag	(–5.60)			
Roll/lateral flap			[0.932,3.34]	[0.609,5.37]
Regressing flap	[0.927,11.9]	[0.601,10.3]	[0.830,7.08]	
Differential lead-lag			[0.195,7.28]	
Collective lead-lag			[0.224,7.91]	[0.725,7.88]
Collective inflow			(24.55)	(19.348)
Regr lead-lag	[0.180,16.9]	[0.175,18.9]	[0.0615,18.5]	[0.210,20.1]
Cyclic inflow			[0.920,32.4]	[0.993,24.7]
Coning/aero lag		[0.819,23.7]		
Coning	[0.411,34.4]		[0.306,25.95]	[0.332,26.0]
Differential flap			[0.383,27.5]	
Coning/aero lag		[0.316,34.6]		
Progr lead-lag			[0.0420,38.2]	[0.163,37.6]
Progressing flap	[0.237,51.9]	[0.145,50.2]	[0.183,52.3]	[0.180,52.1]
Aero lag	(82.306)			

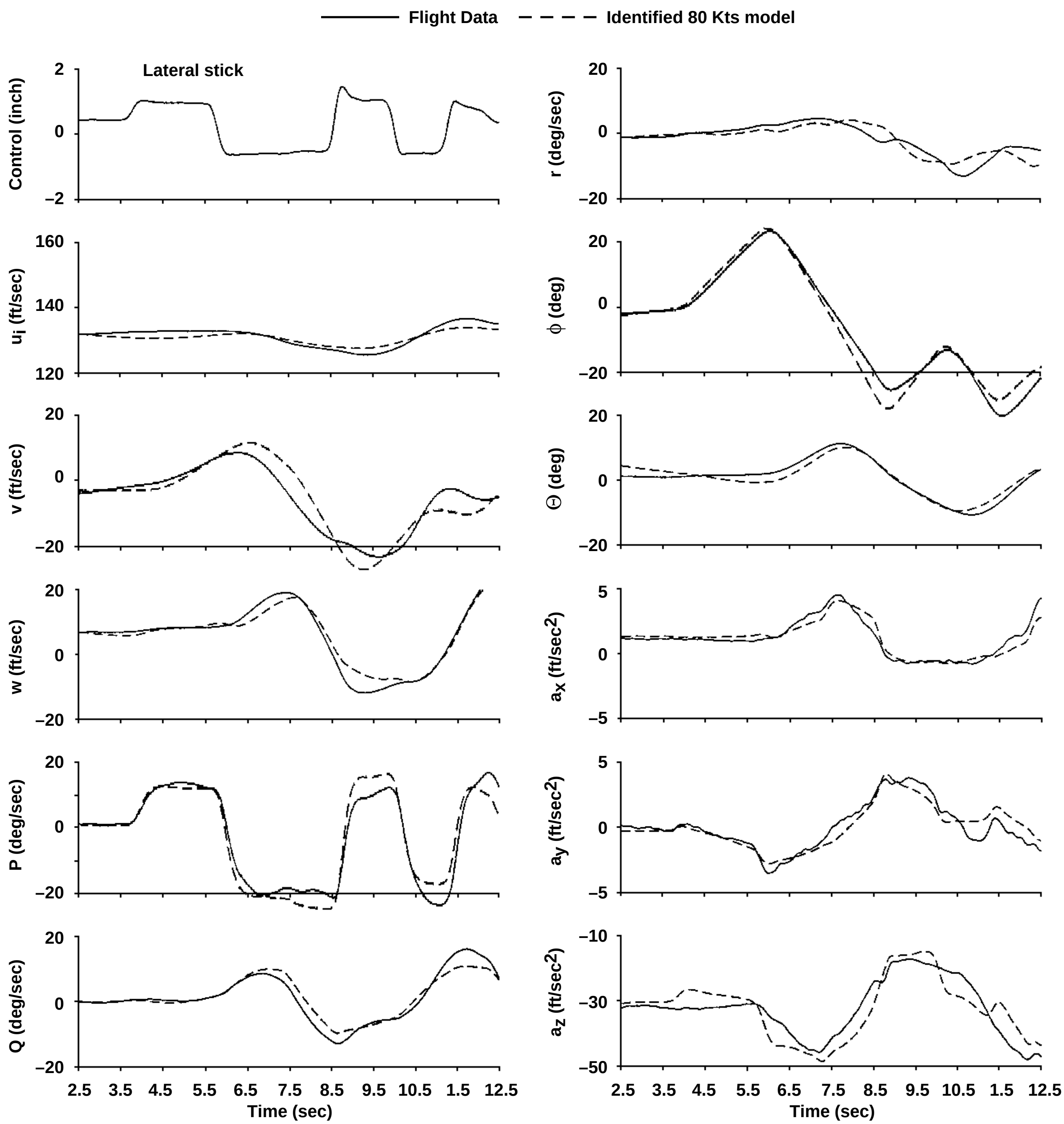

Figure 16. (a) Comparison of model time responses at 80 Kts.

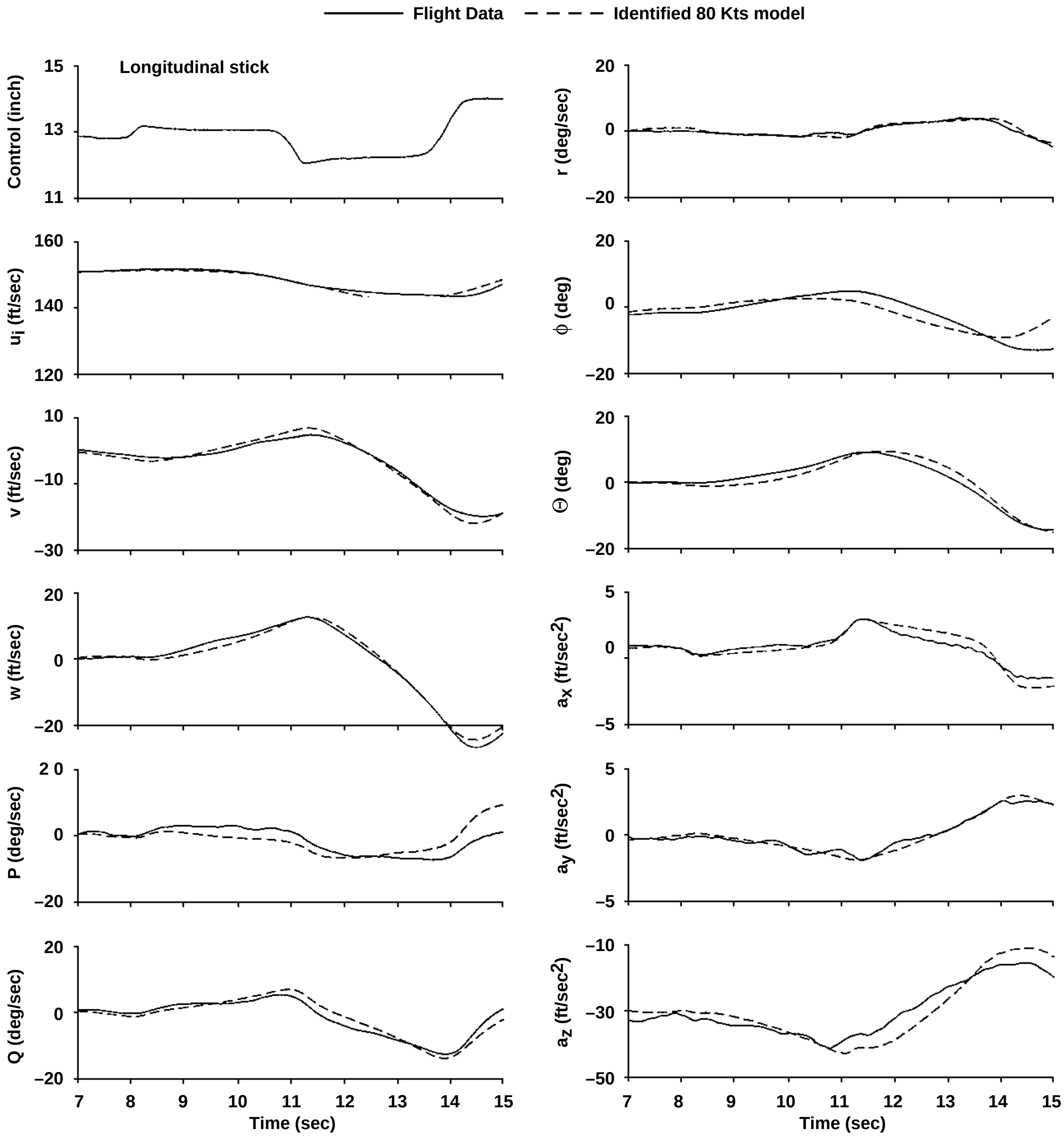

Figure 16. (b) Continued.

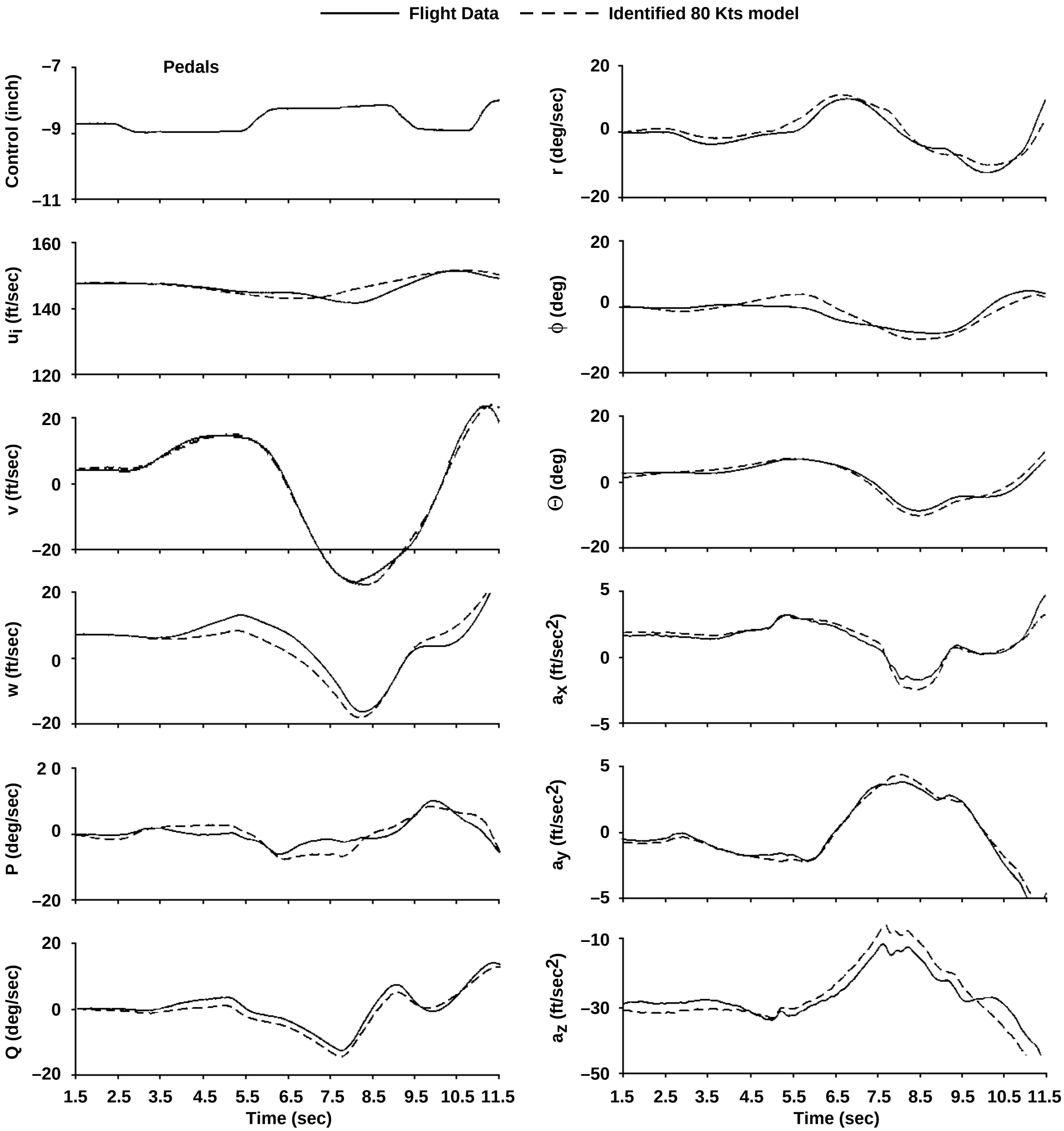

Figure 16. (c) Continued.

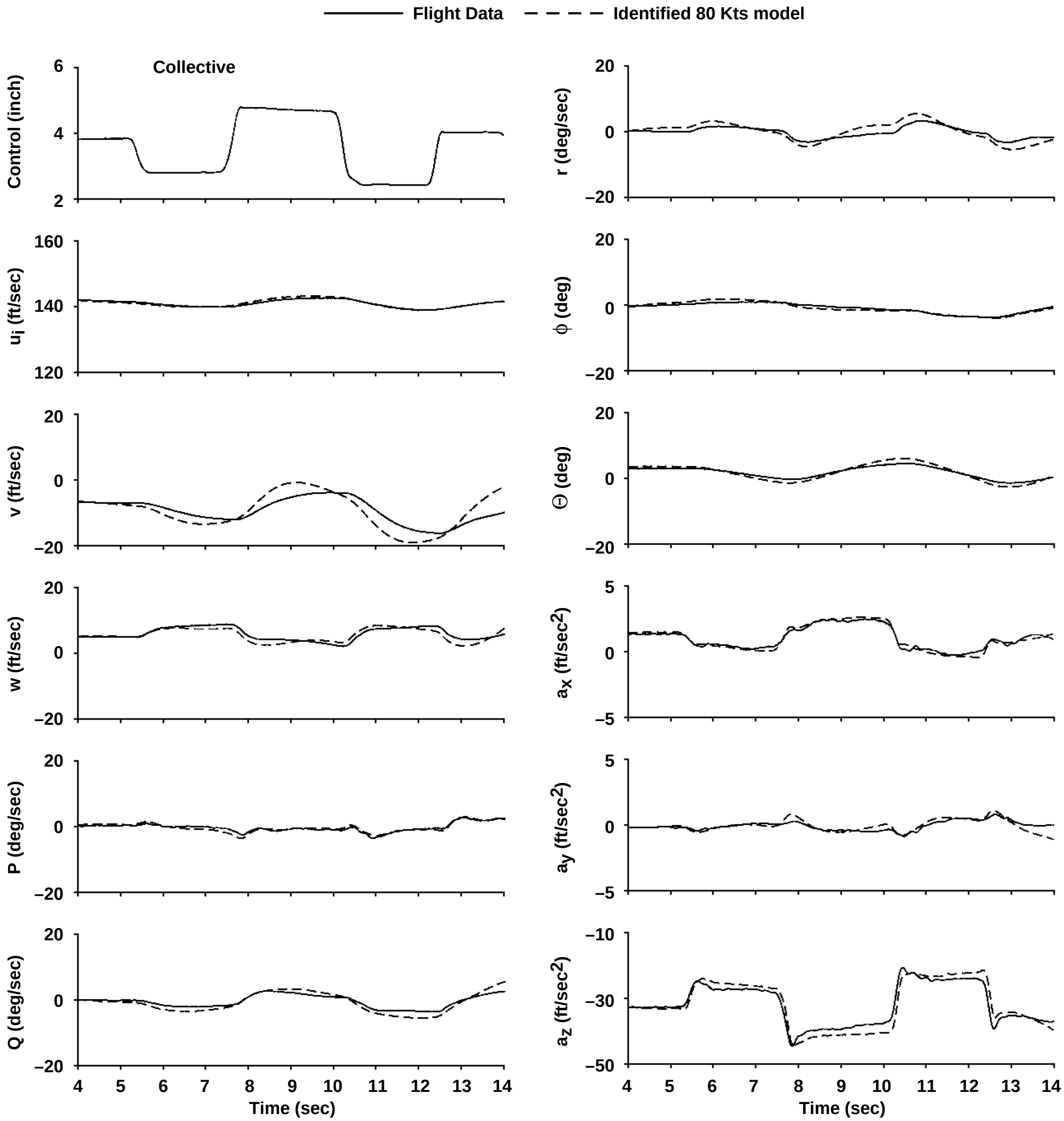

Figure 16. (d) Concluded.

Summary and Conclusions

A model structure applicable to the identification of linear models of the UH-60 in hover and forward flight has been developed. Fuselage linear and angular DOF, main rotor flap, and lead-lag, collective induced velocity, main rotor/ engine rpm, and engine/governor dynamics are included in the general linear model structure formulation.

1. The model structure is not overparameterized when flapping data are not available for use in the identification.

2. Introduction of the aerodynamic phase lag parameter into the flapping dynamics allows identification of models which correctly predict the off-axis response without relaxing physical constraints in the flapping equations of motion.

3. The model structure is appropriate for identification of models for use in the design of high bandwidth control laws for the UH-60 at hover and 80 kts forward flight.

Linear models of the UH-60 flight dynamics at hover and 80 kts forward flight have been identified from flight-test data using the developed linear model structure.

1. The identified models adequately fit the flight-test data and accurately predict the vehicle response to pilot inputs in the frequency range of 0.3 to 20 rad/sec.

2. They predict the on-axis responses of the helicopter with at least equal fidelity and the off-axis angular responses to cyclic controls with improved fidelity when compared with two BE simulation models of the UH-60.

3. The identified models predict the yaw-heave coupling of the helicopter with improved fidelity compared to the BE models.

References

1. Tischler, M. B.: Digital Control of Highly Augmented Combat Rotorcraft. NASA TM-88346, USAAVSCOM Technical Report 87-A-5, May 1987.

2. Curtiss, H. C., Jr.: On the Calculation of the Response of Helicopters to Control Inputs. 18th European Rotorcraft Forum, Avignon, France, Sept. 1992.

3. Takahashi, M. D.: A Flight-Dynamic Helicopter Mathematical Model with Single Flap-Lag-Torsion Main Rotor. NASA TM-102267, USAAVSCOM TM-90-A-004, Feb. 1990.

4. Kim, F. D.: Analysis of Propulsion System Dynamics in the Validation of a High-Order State Space Model of the UH-60. AIAA-92-4150-CP, AIAA/AHS Flight Simulation Technologies Conference, Hilton Head, S.C., Aug. 1992.

5. Peters, D. A.; and HaQuang, N.: Dynamic Induced Velocity for Practical Applications. J. Amer. Hel. Soc., vol., no., Oct. 1988, pp. 64–68.

6. Takahashi, M. D.; Fletcher, J. W.; and Tischler, M. B.: Development of a Model Following Control Law for Inflight Simulation Using Analytical and Identified Models. 51st Annual Forum of the Amer. Hel. Soc., Fort Worth, Tex., May 1995.

7. Mansur, M. H.: Development and Validation of a Blade-Element Mathematical Model for the AH-64A Apache Helicopter. NASA TM-108863, USAATCOM Technical Report 94-A-002, Apr. 1995.

8. 8 FMP WG-18: Rotorcraft System Identification. 8 Advisory Report 280, 8-AR-280, 1991.

9. Fletcher, J. W. Identification of UH-60 Stability Derivative Models in Hover from Flight Test Data. J. Amer. Hel. Soc., vol. 40, no. 1, pp. 32-46, Jan. 1995.

10. Rosen, A.; and Isser, A.: A New Model of Rotor Dynamics During Pitch and Roll of a Hovering Helicopter. 50th Amer. Hel. Soc. Ann. Form., Washington, D.C., May 1994.

11. Tischler, M. B.; Driscoll, J. T.; Cauffman, M. G.; and Freedman, C. J.: Study of Bearingless Main Rotor Dynamics from Frequency-Response Wind Tunnel Test Data. Paper presented at the AHS Aeromechanics Specialists Conference, San Francisco, Calif., Jan. 1994.

12. Aiken, E.; Jacobsen, R.; Eshow, M., Hindson, W.; and Doane, D.: Preliminary Design Features of the RASCAL – A NASA/Army Rotorcraft In-Flight Simulator. AIAA-92-4175, Aug. 1992.

13. Chen, R. T. N.; and Hindson, W. S.: Influence of High-Order Dynamics on Helicopter Control System Bandwidth. AIAA J. Guid., Cont., and Dyn., vol. 9, no. 2, 1986, pp. 190–197.

14. Takahashi, M. D.: Rotor-State Feedback in the Design of Flight-Control Laws for a Hovering Helicopter. J. Amer. Hel. Soc., vol. 39, no. 1. Jan. 1994.

15. Hilbert, K. B.; Lebacqz, J. V.; and Hindson, W. S.: Flight Investigation of a Multivariable Model-Following Control System for Rotorcraft. AIAA Paper 86-9779, AIAA 3rd Flight Test Conference, Las Vegas, Nev., Apr. 1986

16. Kaletka, J.; and von Grünhagen, W.: Identification of Mathematical Derivative Models for the Design of a Model Following Control System. 45th Ann. Form. Amer. Hel. Soc., Boston, Mass., May 1989.

17. Chen, R. T. N.: An Exploratory Investigation of the Flight Dynamic Effects of Rotor rpm Variations and Rotor State Feedbacks in Hover. 18th European Rotorcraft Forum, Avignon, France, Sept. 1992.

18. Chen, R. T. N.; and Hindson, W. S.: Influence of Dynamic Induced velocity on the Helicopter Vertical Response. NASA TM-88327, June 1986.

19. Chen, R. T. N.: A Simplified Rotor System Mathematical Model for Piloted Flight Dynamics Simulation. NASA TM-78575, May 1979.

20. Chen, R. T. N.: Flap-Lag Equations of Motion of Rigid, Articulated Rotor Blades with Three Hinge Sequences. NASA TM-100023, Nov. 1987.

21. Takahashi, M. D.: Flight-Control Design Using Rotor-State Feedback for an Articulated Rotor Helicopter in Hover. NASA TM-103967, USAATCOM Technical Report 92-A-012, March 1993.

22. Tischler, M. B.: System Identification Requirements for High-Bandwidth Rotorcraft Flight Control System Design. J. Guid., Cont., and Dyn., vol. 13, no. 5, 1990, pp. 835–841.

23. Tischler, M. B.; and Cauffman, M. G.: Frequency-Response Method for Rotorcraft System Identification: Flight Applications to BO 105 Coupled Rotor/Fuselage Dynamics. J. Amer. Hel. Soc., vol. 37, no. 3, July 1992, pp. 3–17.

24. Harding, J. W.: Frequency Domain Identification of Coupled Rotor/Body Models of the AH-64. 48th Ann. Form. Amer. Hel. Soc., Washington, D.C., June 1992.

25. Curtiss, H. C., Jr.: Stability and Control Modeling. Vertica, vol. 12, no. 4, 1988.

26. Ballin, M. G.; and Dalang-Secretan, M. A.: Validation of the Dynamic Response of a Blade-Element UH-60 Simulation Model in Hovering Flight. 46th Ann. Form. Amer. Hel. Soc., Washington, D.C., May 1990.

27. Tischler, M. B.; Fletcher, J. W.; Diekman, V. L.; Williams, R. A.; and Cason, R. W.: Demonstration of Frequency-Sweep Testing Technique Using a Bell 214-ST Helicopter. NASA TM-89422, USAAVSCOM TM-87-A-1, Apr. 1987.

28. Holland, R.: Digital Processing of Flight Test Data of a Helicopter without Using Anti-Aliasing Filters. ESA Translation from DFVLR-Mitt. 87-12, ESA-TT-1094, 1987.

29. Bach, R. E., Jr.: State Estimation Applications in Aircraft Flight-Data Analysis: A User’s Manual for SMACK. NASA RP-1252, March 1991.

30. Fletcher, J. W.:Obtaining Consistent Models of Helicopter Flight-Data Measurement Errors Using Kinematic -Compatibility and State-Reconstruction Methods. 46th Ann. Form. Amer. Hel. Soc., Washington, D.C., May 1990.

Appendix A

Appendix A

Linear Model Structure for Identification

A thirty-three state formulation of the linear model structure for identification according to the state equation (A-1) is presented in symbolic form in figure (A-1). The model includes dynamics for the rigid body fuselage, main rotor tip-path-plane flapping, coning, and sine and cosine lead-lag, main rotor angular velocity, engine torque, main rotor induced velocity, fuel flow, and engine governor of the UH-60. Partitions in the matrices serve to illustrate where coupling occurs between the fuselage, flapping, lead-lag, and engine/governor/induced velocity dynamics. The control matrix represents the known control phasing though the swashplate and mixer. This formulation can be simplified to the forward flight case by removing the rpm, induced velocity, torque, fuel flow, and rotor azimuth state equations.

$$M\dot{x}(t) = Fx(t) + Gu(t) \qquad \text{(A-1)}$$

The observation equation used in the identifications is shown in equation (A-2). The numerical values identified for the parameters in the F, G, H, and j matrices for the hover and 80 Kts identifications are presented in figures A-2 and A-3 respectively.

$$y(t) = Hx(t) + ju(t) \qquad \text{(A-2)}$$

$$
M=\left[\begin{array}{*{31}{c}}
1 \\
& 1 \\
& & 1 & & & & & & & & & Z_{\ddot{a}_0} \\
& & & 1 \\
& & & & 1 \\
& & & & & 1 \\
& & & & & & 1 \\
& & & & & & & 1 \\
& & & & & & & & 1 \\
& & & & & & & & & 1 \\
& & & & & & & & & & 1 \\
& & C_{\dot{w}} & & & & & & & & & 1 \\
& & & & 1 & & & & & & 2\Omega_0 & & 1 \\
& & & 1 & & & & & & -2\Omega_0 & & & & 1 \\
& & & & & & & & & & & & & & 1-\chi \\
& & & & & & & -1 & & & & & & & & 1 \\
& & & & & & & & & & & & & & & & 1 \\
& & & & & & & & & & & & & & & K_D & & \tau_{w_f} \\
& & & & & & & & & & & & & & & & & & 1 \\
{} \\
{} \\
{} \\
& & & & & & & & & & & & & & & & & & & & & & \tau \\
{} \\
{} \\
{} \\
{} \\
{} \\
{} \\
{} \\
{}
\end{array}\right]
\quad
G=\left[\begin{array}{cccc}
{} \\
{} \\
{} \\
{} \\
{} \\
{} \\
{} \\
{} \\
{} \\
{} \\
{} \\
{} \\
{} \\
{} \\
{} \\
{} \\
& & & T_{col} \\
{} \\
{} \\
{} \\
{} \\
{} \\
{} \\
{} \\
{} \\
0.02753 & 0.008322 & -0.004782 & -0.005769 \\
0.004705 & -0.04869 & 0.02798 & 0.007230 \\
& & & 0.02795 \\
& & -0.09667 & 0.02795 \\
{} \\
{}
\end{array}\right]
\quad
x=\left[\begin{array}{c}
u \\ v \\ w \\ p \\ q \\ r \\ \phi \\ \theta \\ a_0 \\ a_1 \\ b_1 \\ \dot{a}_0 \\ \dot{a}_1 \\ \dot{b}_1 \\ \dot{\upsilon} \\ \Omega \\ Q \\ w_f \\ \Psi \\ C_{aero} \\ A_{aero} \\ B_{aero} \\ C'_{aero} \\ A'_{aero} \\ B'_{aero} \\ A_1 \\ B_1 \\ \theta_0 \\ \theta_{tr} \\ x_1 \\ x_2
\end{array}\right]
$$

Figure A-1 Linear identification model structure.

$$
F = \left[\begin{array}{cccccccc|cccccc|ccccc|ccc|ccc|cccc|cc}
X_u&X_v&X_w&X_p&X_q&X_r&&-g & &X_{a_1}&&&& & &&&& & && & && & &&X_{\theta_0}&X_{\theta_{tr}} & & \\
Y_u&Y_v&Y_w&Y_p&Y_q&Y_r&g& & &&Y_{b_1}&&& & &&&& & && & && & &&Y_{\theta_0}&Y_{\theta_{tr}} & & \\
Z_u&Z_v&Z_w&Z_p&Z_q&Z_r&& & Z_{a_0}&Z_{a_1}&Z_{b_1}&Z_{\dot a_0}&&Z_{\dot b_1} & Z_\upsilon&Z_\Omega&&& & && & && & &Z_{B_1}&Z_{\theta_0}&Z_{\theta_{tr}} & & \\
L_u&L_v&L_w&L_p&L_q&L_r&& & &&L_{b_1}&&& & &&&& & && & && & &&L_{\theta_0}&L_{\theta_{tr}} & & \\
M_u&M_v&M_w&M_p&M_q&M_r&& & &M_{a_1}&&&& & &&&& & && & && & &&M_{\theta_0}&M_{\theta_{tr}} & & \\
N_u&N_v&N_w&N_p&N_q&N_r&& & N_{a_0}&N_{a_1}&N_{b_1}&N_{\dot a_0}&&N_{\dot b_1} & N_\upsilon&N_\Omega&N_Q&& & && & && & &N_{B_1}&N_{\theta_0}&N_{\theta_{tr}} & & \\
&&&&&&&&&&&&&&&&&&&&&&&&&&&&&& \\
&&&&&&&&&&&&&&&&&&&&&&&&&&&&&& \\
\hline
&&&&&&& & &&&1&& & &&&& & && & && & &&& & & \\
&&&&&&& & &&&&1& & &&&& & && & && & &&& & & \\
&&&&&&& & &&&&&1 & &&&& & && & && & &&& & & \\
&&&&&&& & C_{a_0}&&&&& & &&&& & && & 1&& & &&& & & \\
&&&A_p&&&& & &A_{a_1}&&&& & &&&& & && & &\sec\psi_a& & &&& & & \\
&&&&B_q&&& & &&B_{b_1}&&& & &&&& & && & &&\sec\psi_a & &&& & & \\
\hline
&&I_w&&&&& & &&&I_{\dot a_0}&& & I_\upsilon&I_\Omega&&& & && & && & &&I_{\theta_0}& & & \\
&&R_w&&&&& & &&&R_{\dot a_0}&& & R_\upsilon&R_\Omega&R_Q&& & && & && & &&R_{\theta_0}& & & \\
&&&&&&& & &&&&& & &&T_Q&T_{w_f}& & && & && & &&& & & \\
&&&&&&& & &&&&& & &K_P&&-1&K_I & && & && & &&& & & \\
&&&&&&& & &&&&& & &1&&& & && & && & &&& & & \\
\hline
&&c_w&c_p&&&& & c_{a_0}&c_{a_1}&c_{b_1}&c_{\dot a_0}&&c_{\dot b_1} & c_\upsilon&&&& & -1&& & && & &c_{B_1}&c_{\theta_0}& & & \\
&&&&a_q&&& & a_{a_0}&a_{a_1}&a_{b_1}&&a_{\dot a_1}& & &&&& & &-1& & && & a_{A_1}&&& & & \\
&&b_w&b_p&&&& & b_{a_0}&b_{a_1}&b_{b_1}&b_{\dot a_0}&&b_{\dot b_1} & b_\upsilon&&&& & &&-1 & && & &b_{B_1}&b_{\theta_0}& & & \\
\hline
&&&x_{1p}&&&& & &&&&& & &&&& & 1&& & -1&& & &&& & & \\
&&&&&&& & &&&&& & &&&& & &\cos\psi_a&-\sin\psi_a & &-1& & &&& & & \\
&&&&&&& & &&&&& & &&&& & &\sin\psi_a&\cos\psi_a & &&-1 & &&& & & \\
\hline
&&&&&&& & &&&&& & &&&& & && & && & -1&&& & & \\
&&&&&&& & &&&&& & &&&& & && & && & &-1&& & & \\
&&&&&&& & &&&&& & &&&& & && & && & &&-1& & & \\
&&&&&&& & &&&&& & &&&& & && & && & &&&-1 & & \\
\hline
&&&&&&& & &&&&& & &&&& & && & && & &&& & &1 \\
&&&&&&& & &&&&& & &&&& & && & && & &&& & x_{21}&x_{22}
\end{array}\right]
$$

Figure A-1 Concluded.

F Matrix					
u	v	w	p	q	r
–0.04430	0.00000	0.00000	0.00000	0.00000	0.00000
0.00000	–0.21927	0.00000	1.82002	0.00000	1.49554
0.00000	0.00000	–0.71540	0.00000	–2.00552	2.28973
0.04090	0.00000	0.00000	0.00000	0.00000	0.00000
–0.01306	0.00771	0.00000	0.00000	0.00000	–0.16786
–0.01870	0.00000	–0.01136	0.00000	–0.36757	–0.44439
0.00000	0.00000	0.00000	1.00000	0.00000	0.00000
0.00000	0.00000	0.00000	0.00000	1.00000	0.00000
0.00000	0.00000	0.00000	–2.16365	0.00000	0.00000
0.00000	0.00000	0.00000	0.00000	2.16365	0.00000
0.00000	0.00000	–0.02419	0.00000	0.00000	0.00000
0.00000	0.00000	11.44000	0.00000	0.00000	0.00000
0.00000	0.00000	0.00000	0.00000	0.00000	0.00000
0.00000	0.00000	0.00000	0.00000	0.00000	0.00000
0.00000	0.00000	0.00000	0.00000	0.00000	0.00000
0.00000	0.00000	0.00000	0.00000	0.00000	0.00000
0.00000	0.00000	0.00000	0.00000	0.00000	0.00000
0.00000	0.00000	0.00000	0.00000	17.43087	0.00000
0.00000	0.00000	0.00000	17.43087	0.00000	0.00000
0.00000	0.00000	0.00000	0.00000	0.00000	0.00000
0.00000	0.00000	0.00000	0.00000	0.00000	0.00000
0.00000	0.00000	0.00000	0.00000	0.00000	0.00000
0.00000	0.00000	0.00000	0.00000	0.00000	0.00000
0.00000	0.00000	0.00000	0.00000	0.00000	0.00000
0.00000	0.00000	0.00000	0.00000	0.00000	0.00000
0.00000	0.00000	0.00000	0.00000	0.00000	0.00000
0.00000	0.00000	0.00000	0.00000	0.00000	0.00000
0.00000	0.00000	–1.34481	0.00000	0.00000	0.00000
0.00000	0.00000	0.00000	0.00000	0.00000	0.00000
0.00000	0.00000	0.00000	–1.56000	0.00000	0.00000
0.00000	0.00000	0.00000	–75.11000	0.00000	0.00000
0.00000	0.00000	0.00000	0.00000	–1.89000	0.00000
0.00000	0.00000	0.00000	0.00000	–161.89999	0.00000

Figure A-2. Hover identification matrix results.

F Matrix					
ϕ	θ	$\dot{a}_1$	$\dot{b}_1$	Ω	ν
0.00000	–32.17000	0.00000	0.00000	0.00000	0.00000
32.17000	0.00000	0.00000	0.00000	0.00000	0.00000
0.00000	0.00000	0.00000	0.00000	–1.48315	0.71540
0.00000	0.00000	0.00000	0.00000	0.00000	0.00000
0.00000	0.00000	0.00000	0.00000	0.00000	0.00000
0.00000	0.00000	0.00000	0.00000	0.00000	0.01136
0.00000	0.00000	0.00000	0.00000	0.00000	0.00000
0.00000	0.00000	0.00000	0.00000	0.00000	0.00000
0.00000	0.00000	0.00000	–54.00000	0.00000	0.00000
0.00000	0.00000	54.00000	0.00000	0.00000	0.00000
0.00000	0.00000	0.00000	0.00000	–0.33310	0.02419
0.00000	0.00000	0.00000	0.00000	20.02000	–17.03000
0.00000	0.00000	0.00000	0.00000	0.00000	0.00000
0.00000	0.00000	0.00000	0.00000	–0.05950	0.00000
0.00000	0.00000	0.00000	0.00000	1.00000	0.00000
0.00000	0.00000	1.00000	0.00000	0.00000	0.00000
0.00000	0.00000	0.00000	1.00000	0.00000	0.00000
0.00000	0.00000	16.27571	0.00000	0.00000	0.00000
0.00000	0.00000	0.00000	16.27571	0.00000	0.00000
0.00000	0.00000	0.00000	0.00000	0.00000	0.00000
0.00000	0.00000	0.00000	0.00000	0.00000	0.00000
0.00000	0.00000	0.00000	0.00000	0.00000	0.00000
0.00000	0.00000	0.00000	0.00000	0.00000	0.00000
0.00000	0.00000	0.00000	0.00000	0.00000	0.00000
0.00000	0.00000	0.00000	0.00000	0.00000	0.00000
0.00000	0.00000	0.00000	0.00000	0.00000	0.00000
0.00000	0.00000	0.00000	0.00000	0.00000	0.00000
0.00000	0.00000	0.00000	0.00000	0.00000	1.34481
0.00000	0.00000	0.00000	0.00000	0.00000	0.00000
0.00000	0.00000	0.00000	0.00000	0.00000	0.00000
0.00000	0.00000	0.00000	0.00000	0.00000	0.00000
0.00000	0.00000	0.00000	0.00000	0.00000	0.00000
0.00000	0.00000	0.00000	0.00000	0.00000	0.00000

Figure A-2. Continued.

F Matrix					
Q	w_f	Ψ	a_1	b_1	A_{aero}
0.00000	0.00000	0.00000	–32.17400	0.00000	0.00000
0.00000	0.00000	0.00000	0.00000	32.17400	0.00000
0.00000	0.00000	0.00000	0.00000	0.00000	0.00000
0.00000	0.00000	0.00000	0.00000	48.64883	0.00000
0.00000	0.00000	0.00000	5.22099	0.00000	0.00000
0.01759	0.00000	0.00000	0.00000	4.49138	0.00000
0.00000	0.00000	0.00000	0.00000	0.00000	0.00000
0.00000	0.00000	0.00000	0.00000	0.00000	0.00000
0.00000	0.00000	0.00000	–29.20933	0.00000	0.00000
0.00000	0.00000	0.00000	0.00000	–29.20933	0.00000
0.10737	0.00000	0.00000	0.00000	0.00000	0.00000
0.00000	0.00000	0.00000	0.00000	0.00000	0.00000
–7.84700	3106.00000	0.00000	0.00000	0.00000	0.00000
0.00000	–1.00000	–0.09090	0.00000	0.00000	0.00000
0.00000	0.00000	0.00000	0.00000	0.00000	0.00000
0.00000	0.00000	0.00000	0.00000	0.00000	0.00000
0.00000	0.00000	0.00000	0.00000	0.00000	0.00000
0.00000	0.00000	0.00000	64.51820	439.47861	0.00000
0.00000	0.00000	0.00000	–439.47861	64.51820	0.00000
0.00000	0.00000	0.00000	0.00000	0.00000	0.00000
0.00000	0.00000	0.00000	0.00000	0.00000	0.00000
0.00000	0.00000	0.00000	0.00000	0.00000	0.00000
0.00000	0.00000	0.00000	0.00000	0.00000	0.00000
0.00000	0.00000	0.00000	0.00000	0.00000	0.00000
0.00000	0.00000	0.00000	0.00000	0.00000	0.00000
0.00000	0.00000	0.00000	0.00000	0.00000	0.00000
0.00000	0.00000	0.00000	0.00000	0.00000	0.00000
0.00000	0.00000	0.00000	0.00000	0.00000	0.00000
0.00000	0.00000	0.00000	0.00000	0.00000	0.00000
0.00000	0.00000	0.00000	0.00000	0.00000	0.00000
0.00000	0.00000	0.00000	0.00000	0.00000	0.00000
0.00000	0.00000	0.00000	0.00000	0.00000	0.00000
0.00000	0.00000	0.00000	0.00000	0.00000	0.00000

Figure A-2. Continued.

F Matrix

B_{aero}	A'_{aero}	B'_{aero}	A_1	B_1
0.00000	0.00000	0.00000	0.00000	0.00000
0.00000	0.00000	0.00000	0.00000	0.00000
0.00000	0.00000	0.00000	0.00000	0.00000
0.00000	0.00000	0.00000	0.00000	0.00000
0.00000	0.00000	0.00000	0.00000	0.00000
0.00000	0.00000	0.00000	0.00000	0.00000
0.00000	0.00000	0.00000	0.00000	0.00000
0.00000	0.00000	0.00000	0.00000	0.00000
0.00000	0.00000	0.00000	0.00000	0.00000
0.00000	0.00000	0.00000	0.00000	0.00000
0.00000	0.00000	0.00000	0.00000	0.00000
0.00000	0.00000	0.00000	0.00000	0.00000
0.00000	0.00000	0.00000	0.00000	0.00000
0.00000	0.00000	0.00000	0.00000	0.00000
0.00000	0.00000	0.00000	0.00000	0.00000
0.00000	0.00000	0.00000	0.00000	0.00000
0.00000	0.00000	0.00000	0.00000	0.00000
0.00000	0.00000	0.00000	0.00000	0.00000
0.00000	0.00000	0.00000	0.00000	0.00000
0.00000	0.00000	0.00000	0.00000	0.00000
0.00000	0.00000	0.00000	0.00000	0.00000
0.00000	0.00000	0.00000	0.00000	0.00000
0.00000	0.00000	0.00000	0.00000	0.00000
0.00000	0.00000	0.00000	0.00000	0.00000
0.00000	0.00000	0.00000	0.00000	0.00000
0.00000	0.00000	0.00000	0.00000	0.00000
0.00000	0.00000	0.00000	0.00000	0.00000
0.00000	0.00000	0.00000	0.00000	0.00000
0.00000	0.00000	0.00000	0.00000	0.00000
0.00000	0.00000	0.00000	0.00000	0.00000
0.00000	0.00000	0.00000	0.00000	0.00000
0.00000	0.00000	0.00000	0.00000	0.00000
0.00000	0.00000	0.00000	0.00000	0.00000

Figure A-2. Continued.

F Matrix					
θ_0	θ_{tr}	$\dot{a}_1$	a_0	C_{aero}	C'_{aero}
0.00000	0.00000	0.00000	0.00000	0.00000	0.00000
0.00000	0.00000	0.00000	0.00000	0.00000	0.00000
0.00000	0.00000	20.64279	53.41310	0.00000	0.00000
0.00000	0.00000	0.00000	0.00000	0.00000	0.00000
0.00000	0.00000	0.00000	0.00000	0.00000	0.00000
0.00000	0.00000	0.00000	–0.44331	0.00000	0.00000
0.00000	0.00000	0.00000	0.00000	0.00000	0.00000
0.00000	0.00000	0.00000	0.00000	0.00000	0.00000
0.00000	0.00000	0.00000	0.00000	0.00000	0.00000
0.00000	0.00000	0.00000	0.00000	0.00000	0.00000
0.00000	0.00000	2.98800	0.00000	0.00000	0.00000
0.00000	0.00000	–197.30000	0.00000	0.00000	0.00000
0.00000	0.00000	0.00000	0.00000	0.00000	0.00000
0.00000	0.00000	0.00000	0.00000	0.00000	0.00000
0.00000	0.00000	0.00000	0.00000	0.00000	0.00000
0.00000	0.00000	0.00000	0.00000	0.00000	0.00000
0.00000	0.00000	0.00000	0.00000	0.00000	0.00000
0.00000	0.00000	0.00000	0.00000	0.00000	0.00000
0.00000	0.00000	0.00000	0.00000	0.00000	0.00000
0.00000	0.00000	0.00000	0.00000	0.00000	0.00000
0.00000	0.00000	0.00000	0.00000	0.00000	0.00000
0.00000	0.00000	0.00000	0.00000	0.00000	0.00000
0.00000	0.00000	0.00000	0.00000	0.00000	0.00000
0.00000	0.00000	0.00000	0.00000	0.00000	0.00000
0.00000	0.00000	0.00000	0.00000	0.00000	0.00000
0.00000	0.00000	0.00000	–29.20935	0.00000	–1.00000
0.00000	0.00000	1.00000	0.00000	0.00000	0.00000
0.00000	0.00000	25.48252	101.00093	0.00000	0.00000
0.00000	0.00000	0.00000	0.00000	0.00000	–1.00000
0.00000	0.00000	0.00000	0.00000	0.00000	0.00000
0.00000	0.00000	0.00000	0.00000	0.00000	0.00000
0.00000	0.00000	0.00000	0.00000	0.00000	0.00000
0.00000	0.00000	0.00000	0.00000	0.00000	0.00000

Figure A-2. Continued.

F Matrix			
x_1	x_2	x_3	x_4
0.00000	0.00000	0.00000	0.00000
0.00000	0.00000	0.00000	0.00000
0.00000	0.00000	0.00000	0.00000
0.00000	0.00000	0.00000	0.00000
0.00000	0.00000	0.00000	0.00000
0.00000	0.00000	0.00000	0.00000
0.00000	0.00000	0.00000	0.00000
0.00000	0.00000	0.00000	0.00000
0.00000	0.00000	0.00000	0.00000
0.00000	0.00000	0.00000	0.00000
0.00000	0.00000	0.00000	0.00000
0.00000	0.00000	0.00000	0.00000
0.00000	0.00000	0.00000	0.00000
0.00000	0.00000	0.00000	0.00000
0.00000	0.00000	0.00000	0.00000
0.00000	0.00000	0.00000	0.00000
0.00000	0.00000	0.00000	0.00000
0.00000	0.00000	0.00000	0.00000
0.00000	0.00000	0.00000	0.00000
0.00000	0.00000	0.00000	0.00000
0.00000	0.00000	0.00000	0.00000
0.00000	0.00000	0.00000	0.00000
0.00000	0.00000	0.00000	0.00000
0.00000	0.00000	0.00000	0.00000
0.00000	0.00000	0.00000	0.00000
0.00000	0.00000	0.00000	0.00000
0.00000	0.00000	0.00000	0.00000
0.00000	0.00000	0.00000	0.00000
0.00000	0.00000	0.00000	0.00000
0.00000	1.00000	0.00000	0.00000
–356.00000	–6.62000	0.00000	0.00000
0.00000	0.00000	0.00000	1.00000
0.00000	0.00000	–356.00000	–6.62000

Figure A-2. Continued.

G Matrix			
δ_{lat}	δ_{lon}	δ_{ped}	δ_{col}
0.00000	0.00000	0.00000	0.00000
0.00000	0.00000	0.00000	0.00000
0.00000	1.14271	0.00000	0.00000
0.00000	0.00000	0.00000	0.00000
0.00000	0.00000	0.00000	0.00000
0.00000	0.00000	0.00000	0.00000
0.00000	0.00000	0.00000	0.00000
0.00000	0.00000	0.00000	0.00000
0.00000	0.00000	0.00000	0.00000
0.00000	0.00000	0.00000	0.00000
0.00000	0.00000	0.00000	0.00000
0.00000	0.00000	0.00000	4.65900
0.00000	0.00000	0.00000	0.00000
0.00000	0.00000	0.00000	0.00000
0.00000	0.00000	0.00000	0.00000
0.00000	0.00000	0.00000	0.00000
0.00000	0.00000	0.00000	0.00000
0.00000	0.00000	0.00000	0.00000
0.00000	0.00000	0.00000	0.00000
0.00000	0.00000	0.00000	0.00000
0.00000	0.00000	0.00000	0.00000
0.02753	0.00832	–0.00478	–0.00577
0.00471	–0.04869	0.02798	0.00723
0.00000	0.00000	0.00000	0.02795
0.00000	0.00000	–0.09667	0.02795
0.00000	0.00000	0.00000	0.00000
0.00000	0.00000	0.00000	0.00000
0.00000	0.00000	0.00000	0.00000
0.00000	0.00000	0.00000	0.00000
0.00000	0.00000	0.00000	0.00000
0.00000	0.00000	0.00000	0.00000
0.00000	0.00000	0.00000	0.00000
0.00000	0.00000	0.00000	0.00000

Figure A-2. Continued.

Time Delays			
δ_{lat}	δ_{lon}	δ_{ped}	δ_{col}
0.02600	0.02600	0.02600	0.02600
0.02600	0.02600	0.02600	0.02600
0.02600	0.02600	0.02600	0.02600
0.02600	0.02600	0.02600	0.02600
0.02600	0.02600	0.02600	0.02600
0.02600	0.02600	0.02600	0.02600
0.02600	0.02600	0.02600	0.02600
0.02600	0.02600	0.02600	0.02600
0.02600	0.02600	0.02600	0.02600
0.02600	0.02600	0.02600	0.02600
0.02600	0.02600	0.02600	0.02600

H Matrix					
u	v	w	p	q	r
1.00000	0.00000	0.00000	0.00000	0.00000	0.00000
0.00000	1.00000	0.00000	0.00000	0.00000	0.00000
0.00000	0.00000	1.00000	0.00000	0.00000	0.00000
0.00000	0.00000	0.00000	1.24000	0.00000	0.00000
0.00000	0.00000	0.00000	0.00000	1.49000	0.00000
0.00000	0.00000	0.00000	0.00000	0.00000	1.00000
–0.04430	0.00000	0.00000	0.00000	0.00000	0.00000
0.00000	–0.21927	0.00000	1.82002	0.00000	1.49554
0.00000	0.00000	–0.73272	0.00000	–2.05410	2.34520
0.00000	0.00000	0.00000	0.00000	0.00000	0.00000
0.00000	0.00000	0.00000	0.00000	0.00000	0.00000

H Matrix					
ϕ	θ	$\dot{a}_1$	$\dot{b}_1$	Ω	ν
0.00000	0.00000	0.00000	0.00000	0.00000	0.00000
0.00000	0.00000	0.00000	0.00000	0.00000	0.00000
0.00000	0.00000	0.00000	0.00000	0.00000	0.00000
0.00000	0.00000	0.00000	0.00000	0.00000	0.00000
0.00000	0.00000	0.00000	0.00000	0.00000	0.00000
0.00000	0.00000	0.00000	0.00000	0.00000	0.00000
0.00000	0.03000	0.00000	0.00000	0.00000	0.00000
–0.03000	0.00000	0.00000	0.00000	0.00000	0.00000
0.00000	0.00000	0.00000	0.00000	–1.51907	0.73272
0.00000	0.00000	0.00000	0.00000	1.00000	0.00000
0.00000	0.00000	0.00000	0.00000	0.00000	0.00000

Figure A-2. Continued.

H Matrix					
Q	w_f	Ψ	a_1	b_1	A_{aero}
0.00000	0.00000	0.00000	0.00000	0.00000	0.00000
0.00000	0.00000	0.00000	0.00000	0.00000	0.00000
0.00000	0.00000	0.00000	0.00000	0.00000	0.00000
0.00000	0.00000	0.00000	0.00000	0.00000	0.00000
0.00000	0.00000	0.00000	0.00000	0.00000	0.00000
0.00000	0.00000	0.00000	0.00000	0.00000	0.00000
0.00000	0.00000	0.00000	–32.17400	0.00000	0.00000
0.00000	0.00000	0.00000	0.00000	32.17400	0.00000
0.00000	0.00000	0.00000	0.00000	0.00000	0.00000
0.00000	0.00000	0.00000	0.00000	0.00000	0.00000
1.00000	0.00000	0.00000	0.00000	0.00000	0.00000

H Matrix				
B_{-aero}	A'_{aero}	B'_{aero}	A_1	B_1
0.00000	0.00000	0.00000	0.00000	0.00000
0.00000	0.00000	0.00000	0.00000	0.00000
0.00000	0.00000	0.00000	0.00000	0.00000
0.00000	0.00000	0.00000	0.00000	0.00000
0.00000	0.00000	0.00000	0.00000	0.00000
0.00000	0.00000	0.00000	0.00000	0.00000
0.00000	0.00000	0.00000	0.00000	0.00000
0.00000	0.00000	0.00000	0.00000	0.00000
0.00000	0.00000	0.00000	0.00000	0.00000
0.00000	0.00000	0.00000	0.00000	0.00000
0.00000	0.00000	0.00000	0.00000	0.00000

Figure A-2. Continued.

H Matrix					
θ_0	θ_{tr}	$\dot{a}_0$	a_0	C_{aero}	C'_{aero}
0.00000	0.00000	0.00000	0.00000	0.00000	0.00000
0.00000	0.00000	0.00000	0.00000	0.00000	0.00000
0.00000	0.00000	0.00000	0.00000	0.00000	0.00000
0.00000	0.00000	0.00000	0.00000	0.00000	0.00000
0.00000	0.00000	0.00000	0.00000	0.00000	0.00000
0.00000	0.00000	0.00000	0.00000	0.00000	0.00000
0.00000	0.00000	0.00000	0.00000	0.00000	0.00000
0.00000	0.00000	0.00000	0.00000	0.00000	0.00000
0.00000	0.00000	21.14281	–518.25012	0.00000	–0.75567
0.00000	0.00000	0.00000	0.00000	0.00000	0.00000
0.00000	0.00000	0.00000	0.00000	0.00000	0.00000

H Matrix			
x_1	x_2	x_3	x_4
0.00000	0.00000	0.00000	0.00000
0.00000	0.00000	0.00000	0.00000
0.00000	0.00000	0.00000	0.00000
1.00000	0.00000	0.00000	0.00000
0.00000	0.00000	1.00000	0.00000
0.00000	0.00000	0.00000	0.00000
0.00000	0.00000	0.00000	0.00000
0.00000	0.00000	0.00000	0.00000
0.00000	0.00000	0.00000	0.00000
0.00000	0.00000	0.00000	0.00000
0.00000	0.00000	0.00000	0.00000

J Matrix			
δ_{lat}	δ_{lon}	δ_{ped}	δ_{col}
0.00000	0.00000	0.00000	0.00000
0.00000	0.00000	0.00000	0.00000
0.00000	0.00000	0.00000	0.00000
0.00000	0.00000	0.00000	0.00000
0.00000	0.00000	0.00000	0.00000
0.00000	0.00000	0.00000	0.00000
0.00000	0.00000	0.00000	0.47336
0.00000	0.00000	–2.77011	0.80092
0.00000	1.17039	–0.92361	–10.89007
0.00000	0.00000	0.00000	0.00000
0.00000	0.00000	0.00000	0.00000

Output vector = $[u, v, w, p, q, r, a_x, a_y, a_z, \Omega, Q]^T$

Figure A-2. Concluded.

F Matrix					
u	v	w	p	q	r
–0.04985	0.00000	0.03199	0.00000	0.00000	1.49457
0.05161	–0.16011	–0.03226	0.00000	1.97298	3.86122
0.23035	–0.12072	–1.13694	21.42576	0.00000	0.00000
0.01011	0.00000	–0.04281	0.00000	1.83466	–0.44307
–0.00580	0.01259	0.00536	–0.31441	–0.71302	–0.42013
0.00342	0.01000	–0.02131	0.32402	0.00000	–1.23212
0.00000	0.00000	0.00000	1.00000	0.00000	0.04700
0.00000	0.00000	0.00000	0.00000	1.00000	0.00000
0.00000	0.00000	0.00000	–2.16338	0.00000	0.00000
0.00000	0.00000	0.00000	0.00000	2.16338	0.00000
0.00000	0.00000	0.00000	–2.43500	0.00000	0.00000
0.00000	0.00000	0.00000	29.94000	0.00000	0.00000
0.00000	0.00000	0.00000	0.00000	–0.55320	0.00000
0.00000	0.00000	0.00000	0.00000	22.93000	0.00000
0.00000	0.00000	0.00000	0.00000	0.00000	0.00000
0.00000	0.00000	0.00000	0.00000	0.00000	0.00000
0.00000	0.00000	0.00000	0.00000	27.28547	0.00000
0.00000	0.00000	0.00000	27.28547	0.00000	0.00000
0.00000	0.00000	0.00000	0.00000	0.00000	0.00000
0.00000	0.00000	0.00000	0.00000	0.00000	0.00000
0.00000	0.00000	0.00000	0.00000	0.00000	0.00000
0.00000	0.00000	0.00000	0.00000	0.00000	0.00000
0.00000	0.00000	0.00000	0.00000	0.00000	0.00000
0.00000	0.00000	0.00000	0.00000	0.00000	0.00000
0.00000	0.00000	0.00000	0.00000	0.00000	0.00000
0.00000	0.00000	0.00000	0.00000	0.00000	0.00000
0.00000	0.00000	–1.34488	–3.60789	0.00000	0.00000
0.00000	0.00000	0.00000	0.00000	0.00000	0.00000

Figure A-3. 80 kts identification matrix results.

F Matrix					
ϕ	θ	$\dot{a}_1$	$\dot{b}_1$	x_1	x_2
0.00000	–32.17000	0.00000	0.00000	0.00000	0.00000
32.17000	0.00000	0.00000	0.00000	0.00000	0.00000
0.00000	–1.51700	0.00000	0.00000	0.00000	0.00000
0.00000	0.00000	0.00000	0.00000	0.00000	0.00000
0.00000	0.00000	0.00000	0.00000	0.00000	0.00000
0.00000	0.00000	0.00000	0.00000	0.00000	0.00000
0.00000	0.00000	0.00000	0.00000	0.00000	0.00000
0.00000	0.00000	0.00000	0.00000	0.00000	0.00000
0.00000	0.00000	0.00000	–54.00000	0.00000	0.00000
0.00000	0.00000	54.00000	0.00000	0.00000	0.00000
0.00000	0.00000	0.00000	0.00000	0.00000	1.00000
0.00000	0.00000	0.00000	0.00000	–284.39999	–6.07200
0.00000	0.00000	0.00000	0.00000	0.00000	0.00000
0.00000	0.00000	0.00000	0.00000	0.00000	0.00000
0.00000	0.00000	1.00000	0.00000	0.00000	0.00000
0.00000	0.00000	0.00000	1.00000	0.00000	0.00000
0.00000	0.00000	25.48368	0.00000	0.00000	0.00000
0.00000	0.00000	0.00000	25.48368	0.00000	0.00000
0.00000	0.00000	0.00000	0.00000	0.00000	0.00000
0.00000	0.00000	0.00000	0.00000	0.00000	0.00000
0.00000	0.00000	0.00000	0.00000	0.00000	0.00000
0.00000	0.00000	0.00000	0.00000	0.00000	0.00000
0.00000	0.00000	0.00000	0.00000	0.00000	0.00000
0.00000	0.00000	0.00000	0.00000	0.00000	0.00000
0.00000	0.00000	0.00000	0.00000	0.00000	0.00000
0.00000	0.00000	0.00000	0.00000	0.00000	0.00000
0.00000	0.00000	0.00000	–3.33719	0.00000	0.00000
0.00000	0.00000	0.00000	0.00000	0.00000	0.00000

Figure A-3. Continued.

F Matrix				
x_3	x_4	a_1	b_1	A_{aero}
0.00000	0.00000	–32.17400	0.00000	0.00000
0.00000	0.00000	0.00000	32.17400	0.00000
0.00000	0.00000	–73.38137	156.16231	0.00000
0.00000	0.00000	0.00000	54.12263	0.00000
0.00000	0.00000	7.22210	0.00000	0.00000
0.00000	0.00000	–13.36306	5.30503	0.00000
0.00000	0.00000	0.00000	0.00000	0.00000
0.00000	0.00000	0.00000	0.00000	0.00000
0.00000	0.00000	–29.20556	0.00000	0.00000
0.00000	0.00000	0.00000	–29.20556	0.00000
0.00000	0.00000	0.00000	0.00000	0.00000
0.00000	0.00000	0.00000	0.00000	0.00000
0.00000	1.00000	0.00000	0.00000	0.00000
–284.39999	–6.07200	0.00000	0.00000	0.00000
0.00000	0.00000	0.00000	0.00000	0.00000
0.00000	0.00000	0.00000	0.00000	0.00000
0.00000	0.00000	128.84030	702.18042	0.00000
0.00000	0.00000	–673.73120	133.71191	0.00000
0.00000	0.00000	0.00000	0.00000	0.00000
0.00000	0.00000	0.00000	0.00000	0.00000
0.00000	0.00000	0.00000	0.00000	0.00000
0.00000	0.00000	0.00000	0.00000	0.00000
0.00000	0.00000	0.00000	0.00000	0.00000
0.00000	0.00000	0.00000	0.00000	0.00000
0.00000	0.00000	0.00000	0.00000	0.00000
0.00000	0.00000	0.00000	0.00000	0.00000
0.00000	0.00000	–7.32182	–33.42026	0.00000
0.00000	0.00000	0.00000	0.00000	0.00000

Figure A-3. Continued.

F Matrix

B_{aero}	A'_{aero}	B'_{aero}	A_1	B_1
0.00000	0.00000	0.00000	0.00000	0.00000
0.00000	0.00000	0.00000	0.00000	0.00000
0.00000	0.00000	0.00000	0.00000	0.00000
0.00000	0.00000	0.00000	0.00000	0.00000
0.00000	0.00000	0.00000	0.00000	0.00000
0.00000	0.00000	0.00000	0.00000	0.00000
0.00000	0.00000	0.00000	0.00000	0.00000
0.00000	0.00000	0.00000	0.00000	0.00000
0.00000	0.00000	0.00000	0.00000	0.00000
0.00000	0.00000	0.00000	0.00000	0.00000
0.00000	0.00000	0.00000	0.00000	0.00000
0.00000	0.00000	0.00000	0.00000	0.00000
0.00000	0.00000	0.00000	0.00000	0.00000
0.00000	0.00000	0.00000	0.00000	0.00000
0.00000	0.00000	0.00000	0.00000	0.00000
0.00000	0.00000	0.00000	0.00000	0.00000
0.00000	0.00000	0.00000	0.00000	0.00000
0.00000	0.00000	0.00000	0.00000	0.00000
0.00000	0.00000	0.00000	0.00000	0.00000
0.00000	0.00000	0.00000	0.00000	0.00000
0.00000	0.00000	0.00000	0.00000	0.00000
0.00000	0.00000	0.00000	0.00000	0.00000
0.00000	0.00000	0.00000	0.00000	0.00000
0.00000	0.00000	0.00000	0.00000	0.00000
0.00000	0.00000	0.00000	0.00000	0.00000
0.00000	0.00000	0.00000	0.00000	0.00000
0.00000	0.00000	0.00000	0.00000	0.00000
0.00000	0.00000	0.00000	0.00000	0.00000

Figure A-3. Continued.

F Matrix					
θ_0	θ_{tr}	$\dot{a}_0$	a_0	C_{aero}	C'_{aero}
0.00000	0.00000	0.00000	0.00000	0.00000	0.00000
0.00000	0.00000	0.00000	0.00000	0.00000	0.00000
0.00000	0.00000	20.71073	76.31174	0.00000	0.00000
0.00000	0.00000	0.00000	0.00000	0.00000	0.00000
0.00000	0.00000	0.00000	0.00000	0.00000	0.00000
0.00000	0.00000	0.00000	–0.55065	0.00000	0.00000
0.00000	0.00000	0.00000	0.00000	0.00000	0.00000
0.00000	0.00000	0.00000	0.00000	0.00000	0.00000
0.00000	0.00000	0.00000	0.00000	0.00000	0.00000
0.00000	0.00000	0.00000	0.00000	0.00000	0.00000
0.00000	0.00000	0.00000	0.00000	0.00000	0.00000
0.00000	0.00000	0.00000	0.00000	0.00000	0.00000
0.00000	0.00000	0.00000	0.00000	0.00000	0.00000
0.00000	0.00000	0.00000	0.00000	0.00000	0.00000
0.00000	0.00000	0.00000	0.00000	0.00000	0.00000
0.00000	0.00000	0.00000	0.00000	0.00000	0.00000
0.00000	0.00000	0.00000	–194.83461	0.00000	0.00000
0.00000	0.00000	–6.67400	–66.84224	0.00000	0.00000
0.00000	0.00000	0.00000	0.00000	0.00000	0.00000
0.00000	0.00000	0.00000	0.00000	0.00000	0.00000
0.00000	0.00000	0.00000	0.00000	0.00000	0.00000
0.00000	0.00000	0.00000	0.00000	0.00000	0.00000
0.00000	0.00000	0.00000	0.00000	0.00000	0.00000
0.00000	0.00000	0.00000	0.00000	0.00000	0.00000
0.00000	0.00000	0.00000	–29.20557	0.00000	–1.00000
0.00000	0.00000	1.00000	0.00000	0.00000	0.00000
0.00000	0.00000	25.48368	131.27611	0.00000	0.00000
0.00000	0.00000	0.00000	0.00000	0.00000	–1.00000

Figure A-3. Continued.

G Matrix			
DLAT	DLON	DPED	DCOL
0.00000	0.00000	0.00000	0.00000
0.00000	0.00000	0.00000	0.00000
0.00000	0.00000	0.00000	0.00000
0.00000	0.00000	0.00000	0.00000
0.00000	0.00000	0.00000	0.00000
0.00000	0.00000	0.00000	0.00000
0.00000	0.00000	0.00000	0.00000
0.00000	0.00000	0.00000	0.00000
0.00000	0.00000	0.00000	0.00000
0.00000	0.00000	0.00000	0.00000
0.00000	0.00000	0.00000	0.00000
0.00000	0.00000	0.00000	0.00000
0.00000	0.00000	0.00000	0.00000
0.00000	0.00000	0.00000	0.00000
0.00000	0.00000	0.00000	0.00000
0.00000	0.00000	0.00000	0.00000
0.00000	0.00000	0.00000	0.00000
0.00000	0.00000	0.00000	0.00000
0.00000	0.00000	0.00000	0.00000
0.00000	0.00000	0.00000	0.00000
0.02753	0.00832	–0.00478	–0.00577
0.00471	–0.04869	0.02798	0.00723
0.00000	0.00000	0.00000	0.02795
0.00000	0.00000	–0.09667	0.02795
0.00000	0.00000	0.00000	0.00000
0.00000	0.00000	0.00000	0.00000
0.00000	0.00000	0.00000	0.00000
0.00000	0.00000	0.00000	0.00000

Time Delays			
DLAT	DLON	DPED	DCOL
0.02600	0.02600	0.02600	0.02600
0.02600	0.02600	0.02600	0.02600
0.02600	0.02600	0.02600	0.02600
0.02600	0.02600	0.02600	0.02600
0.02600	0.02600	0.02600	0.02600
0.02600	0.02600	0.02600	0.02600
0.02600	0.02600	0.02600	0.02600
0.02600	0.02600	0.02600	0.02600
0.02600	0.02600	0.02600	0.02600

Figure A-3. Continued.

H Matrix					
u	v	w	p	q	r
1.00000	0.00000	0.00000	0.00000	0.00000	0.00000
0.00000	1.00000	0.00000	0.00000	0.00000	0.00000
0.00000	0.00000	1.00000	0.00000	0.00000	0.00000
0.00000	0.00000	0.00000	0.94670	0.00000	0.00000
0.00000	0.00000	0.00000	0.00000	0.93120	0.00000
0.00000	0.00000	0.00000	0.00000	0.00000	1.00000
–0.04985	0.00000	0.03199	0.00000	0.00000	1.49457
0.05161	–0.16011	–0.03226	0.00000	1.97298	3.86122
0.23593	–0.12365	–1.16448	21.94467	3.51178	0.00000

H Matrix					
ϕ	θ	$\dot{a}_1$	$\dot{b}_1$	x_1	x_2
0.00000	0.00000	0.00000	0.00000	0.00000	0.00000
0.00000	0.00000	0.00000	0.00000	0.00000	0.00000
0.00000	0.00000	0.00000	0.00000	0.00000	0.00000
0.00000	0.00000	0.00000	0.00000	1.00000	0.00000
0.00000	0.00000	0.00000	0.00000	0.00000	0.00000
0.00000	0.00000	0.00000	0.00000	0.00000	0.00000
0.00000	0.03000	0.00000	0.00000	0.00000	0.00000
–0.03000	0.00000	0.00000	0.00000	0.00000	0.00000
0.00000	–0.05374	0.00000	0.00000	0.00000	0.00000

H Matrix				
x_3	x_4	a_1	b_1	A_{aero}
0.00000	0.00000	0.00000	0.00000	0.00000
0.00000	0.00000	0.00000	0.00000	0.00000
0.00000	0.00000	0.00000	0.00000	0.00000
0.00000	0.00000	0.00000	0.00000	0.00000
1.00000	0.00000	0.00000	0.00000	0.00000
0.00000	0.00000	0.00000	0.00000	0.00000
0.00000	0.00000	–32.17400	0.00000	0.00000
0.00000	0.00000	0.00000	32.17400	0.00000
0.00000	0.00000	–75.15861	159.94443	0.00000

Figure A-3. Continued.

H Matrix

B_{aero}	A'_{aero}	B'_{aero}	A_1	B_1
0.00000	0.00000	0.00000	0.00000	0.00000
0.00000	0.00000	0.00000	0.00000	0.00000
0.00000	0.00000	0.00000	0.00000	0.00000
0.00000	0.00000	0.00000	0.00000	0.00000
0.00000	0.00000	0.00000	0.00000	0.00000
0.00000	0.00000	0.00000	0.00000	0.00000
0.00000	0.00000	0.00000	0.00000	0.00000
0.00000	0.00000	0.00000	0.00000	0.00000
0.00000	0.00000	0.00000	0.00000	0.00000

H Matrix

θ_0	θ_{tr}	$\dot{a}_0$	a_0	C_{aero}	C'_{aero}
0.00000	0.00000	0.00000	0.00000	0.00000	0.00000
0.00000	0.00000	0.00000	0.00000	0.00000	0.00000
0.00000	0.00000	0.00000	0.00000	0.00000	0.00000
0.00000	0.00000	0.00000	0.00000	0.00000	0.00000
0.00000	0.00000	0.00000	0.00000	0.00000	0.00000
0.00000	0.00000	0.00000	0.00000	0.00000	0.00000
0.00000	0.00000	0.00000	0.00000	0.00000	0.00000
0.00000	0.00000	0.00000	0.00000	0.00000	0.00000
0.00000	0.00000	21.21232	–494.79245	0.00000	–0.75567

J Matrix

DLAT	DLON	DPED	DCOL
0.00000	0.00000	0.00000	0.00000
0.00000	0.00000	0.00000	0.00000
0.00000	0.00000	0.00000	0.00000
0.00000	0.00000	0.00000	0.00000
0.00000	0.00000	0.00000	0.00000
0.00000	0.00000	0.00000	0.00000
0.00000	0.00000	–0.44111	1.09851
0.00000	0.00000	–2.23861	0.64725
0.29750	–3.07865	1.76917	–12.27824

Output vector = $[u, v, w, p, q, r, a_x, a_y, a_z]^T$

Figure A-3. Concluded.

Appendix B

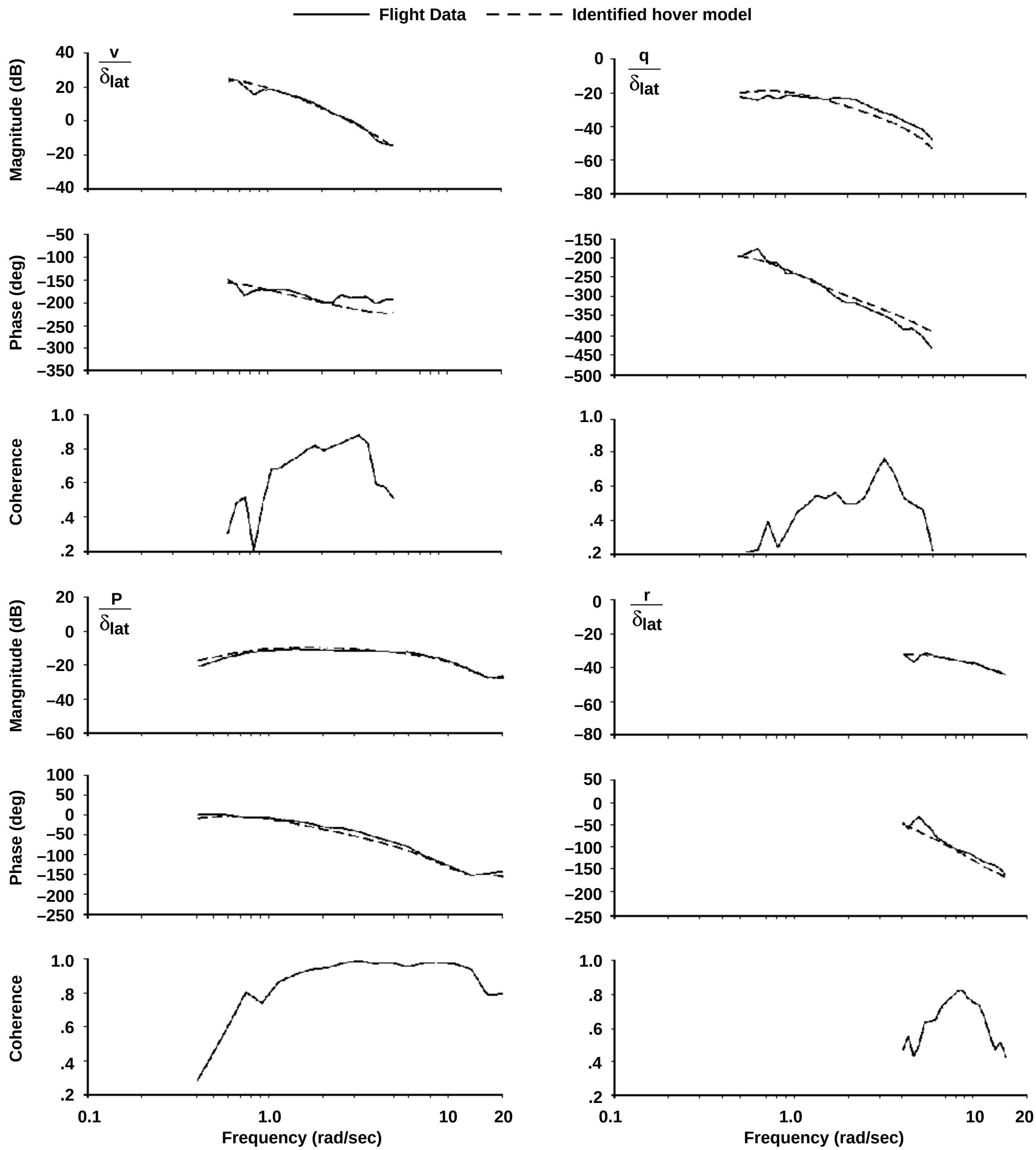

Figure B-1. Hover frequency response comparison.

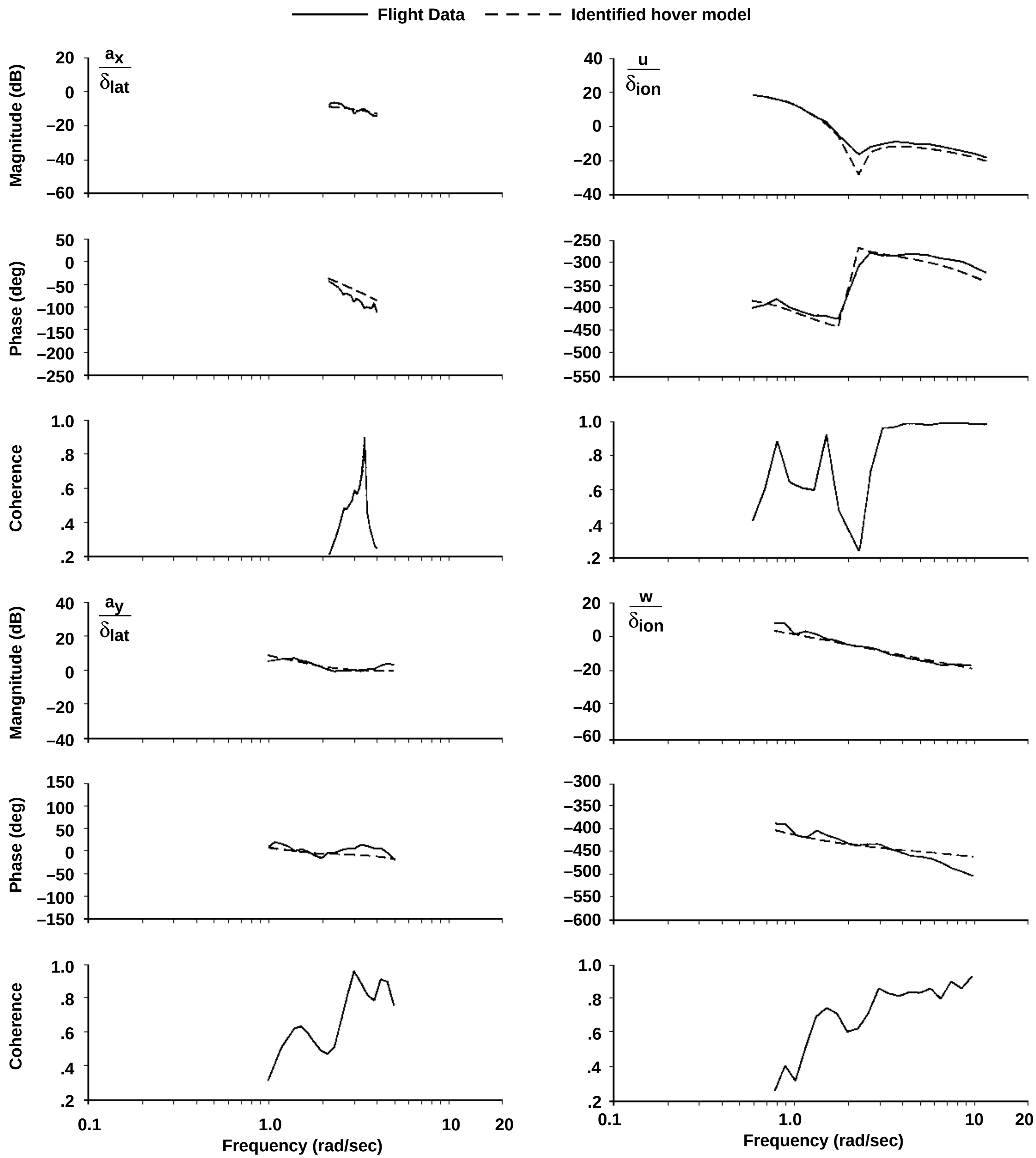

Figure B-1. Continued.

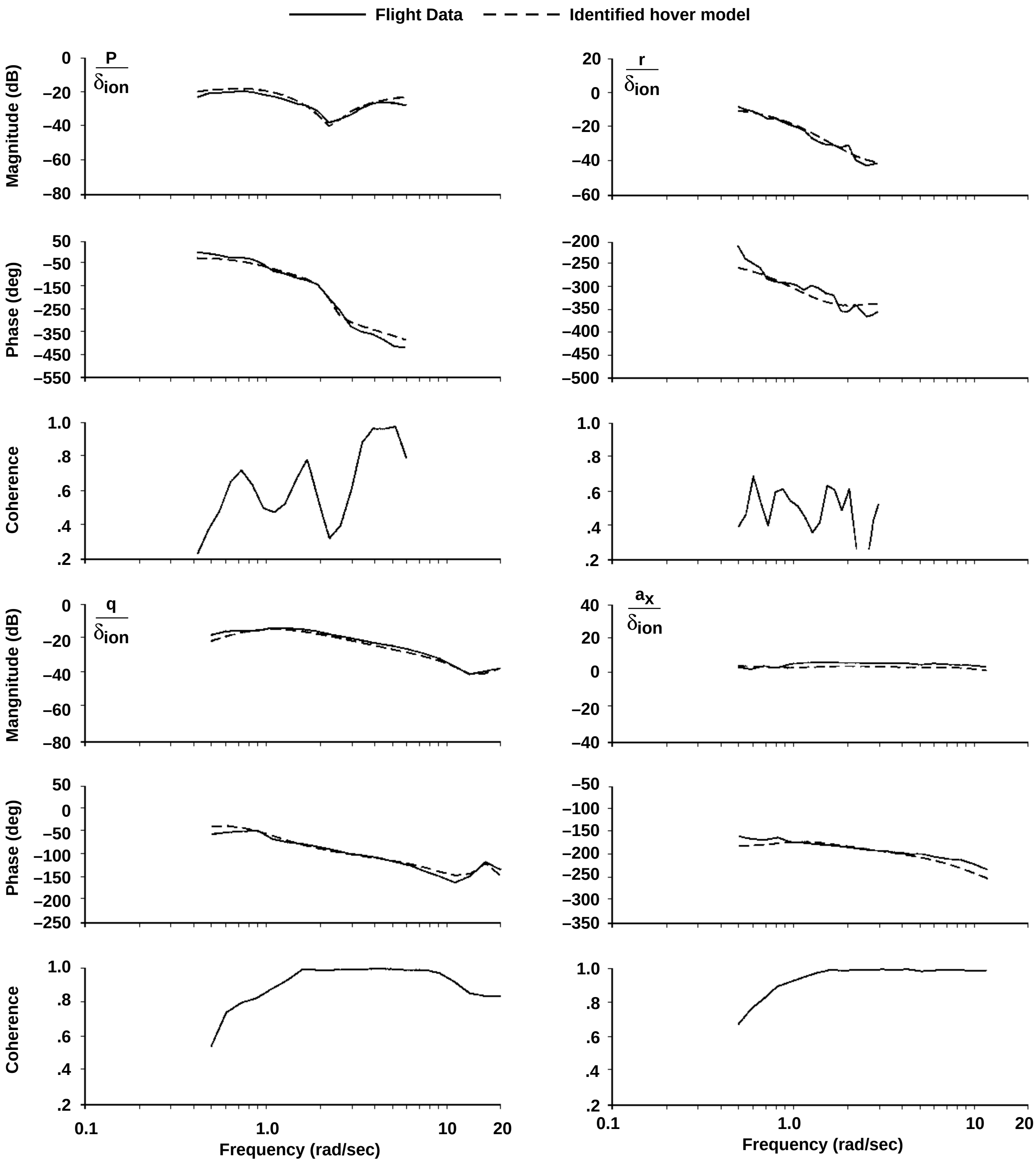

Figure B-1. Continued.

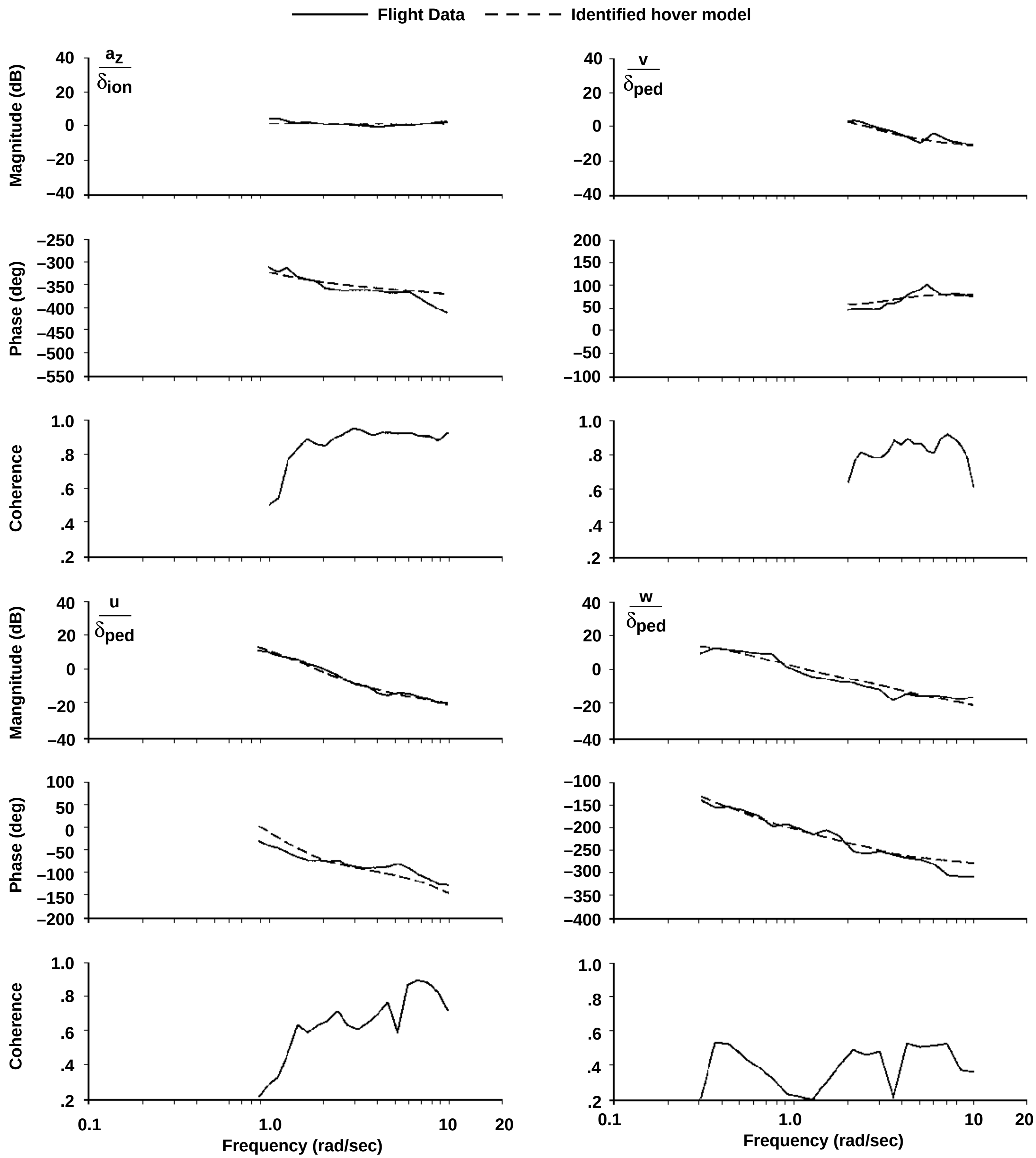

Figure B-1. Continued.

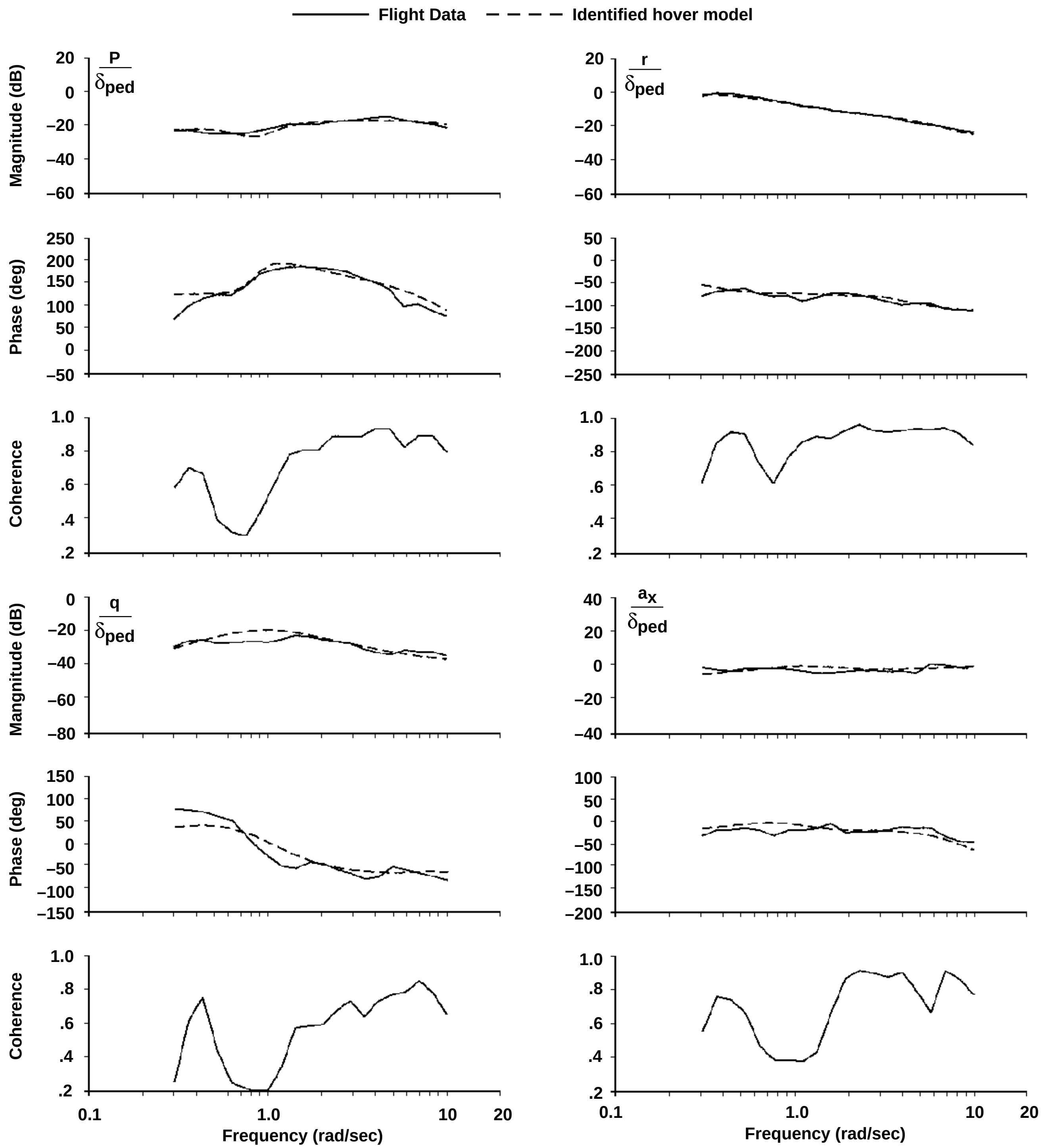

Figure B-1. Continued.

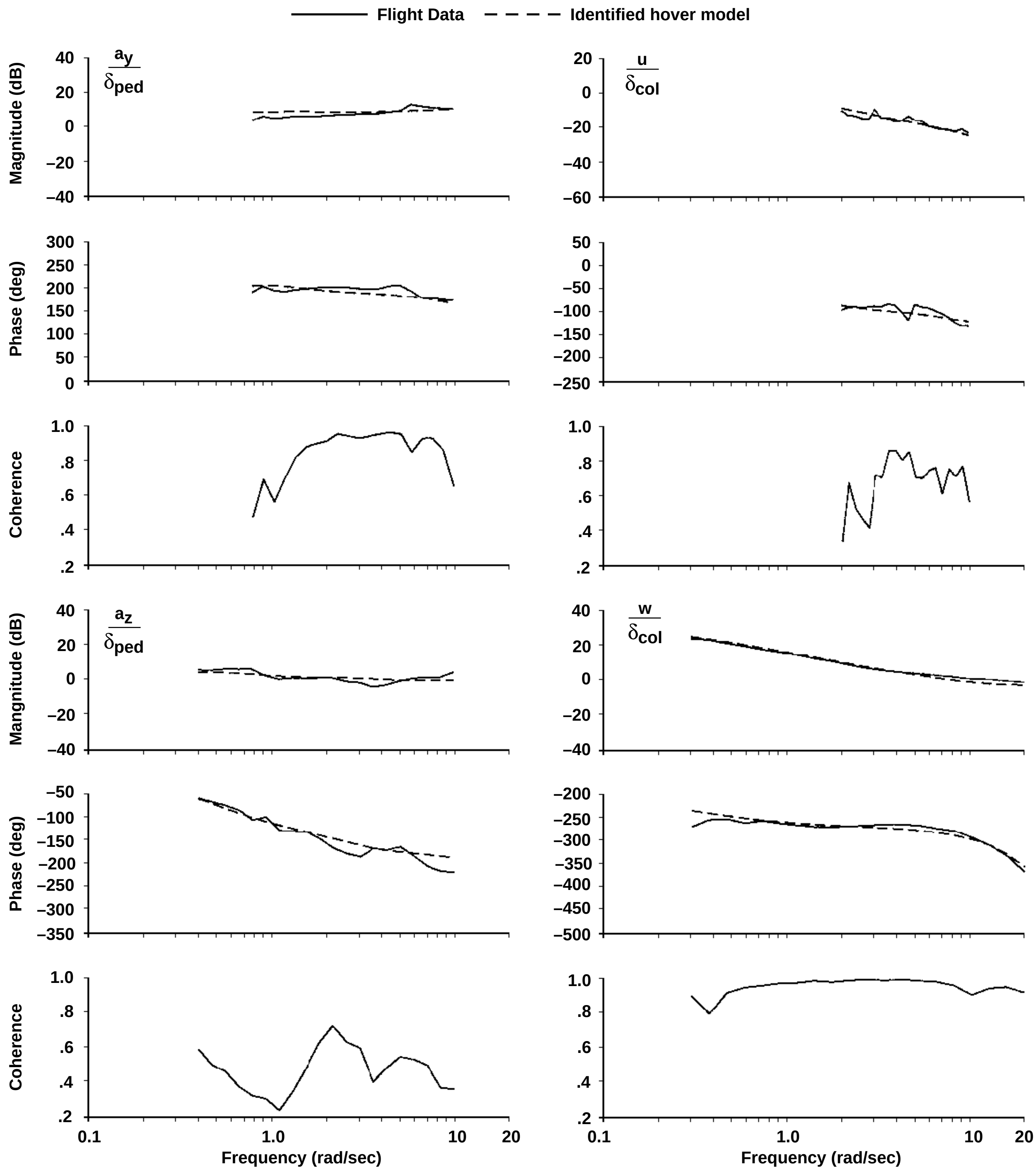

Figure B-1. Continued.

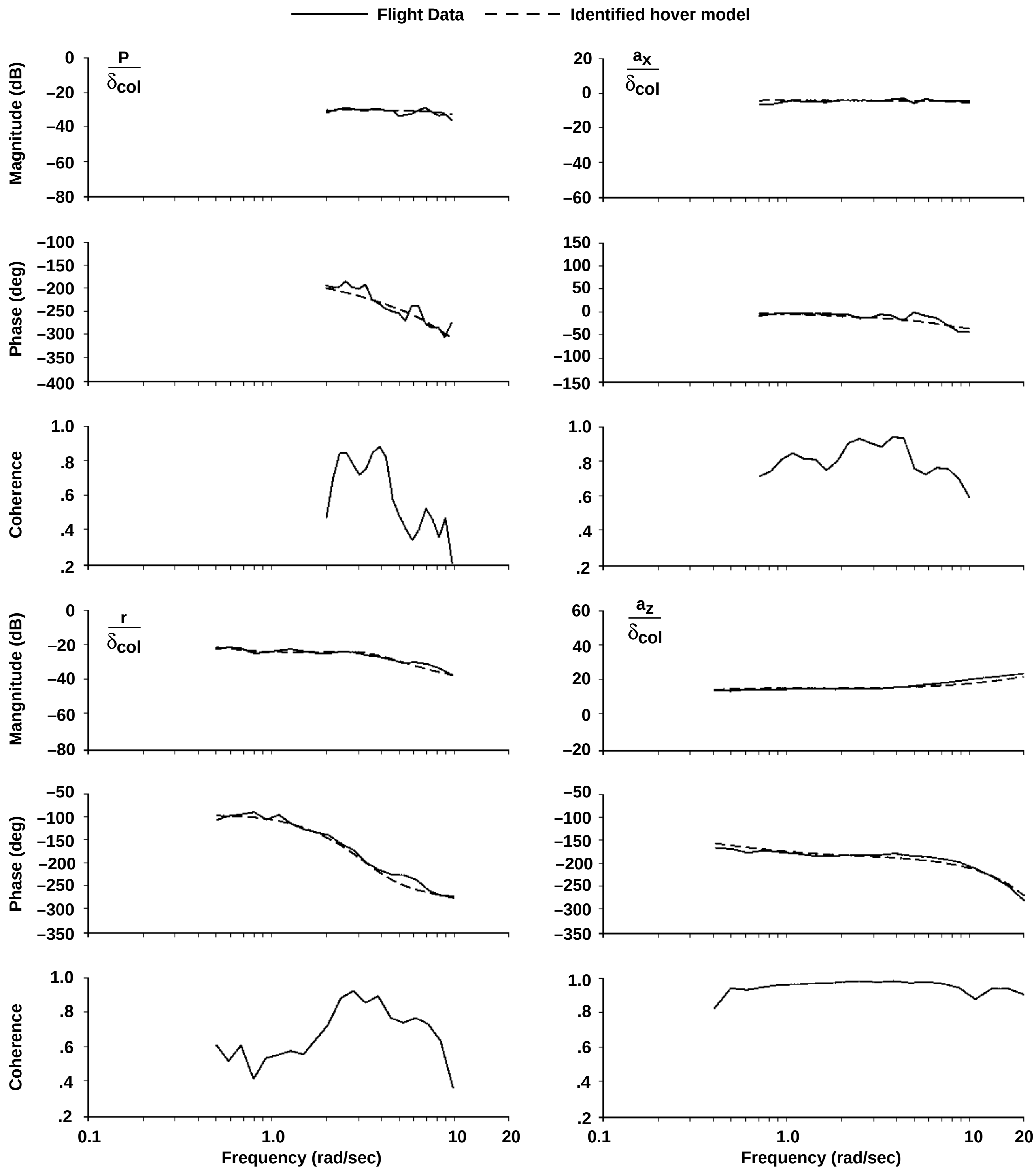

Figure B-1. Continued.

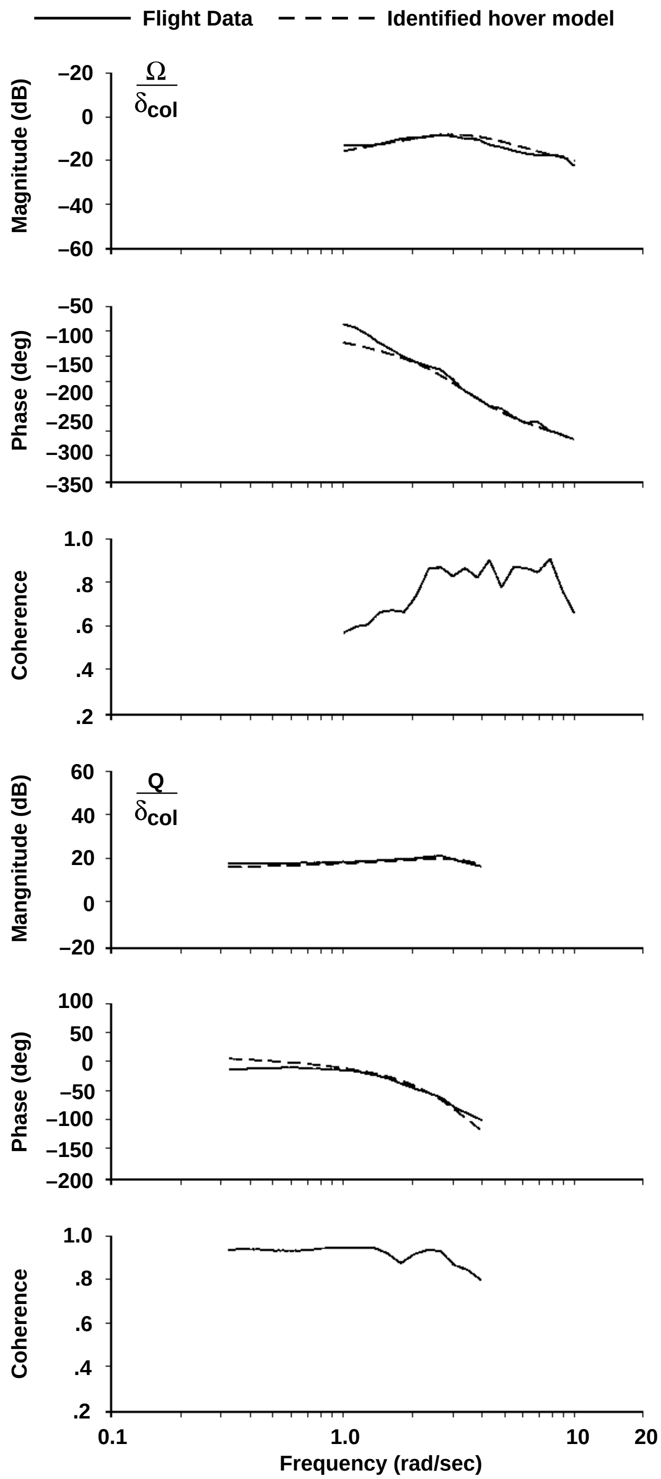

Figure B-1. Concluded.

Appendix C

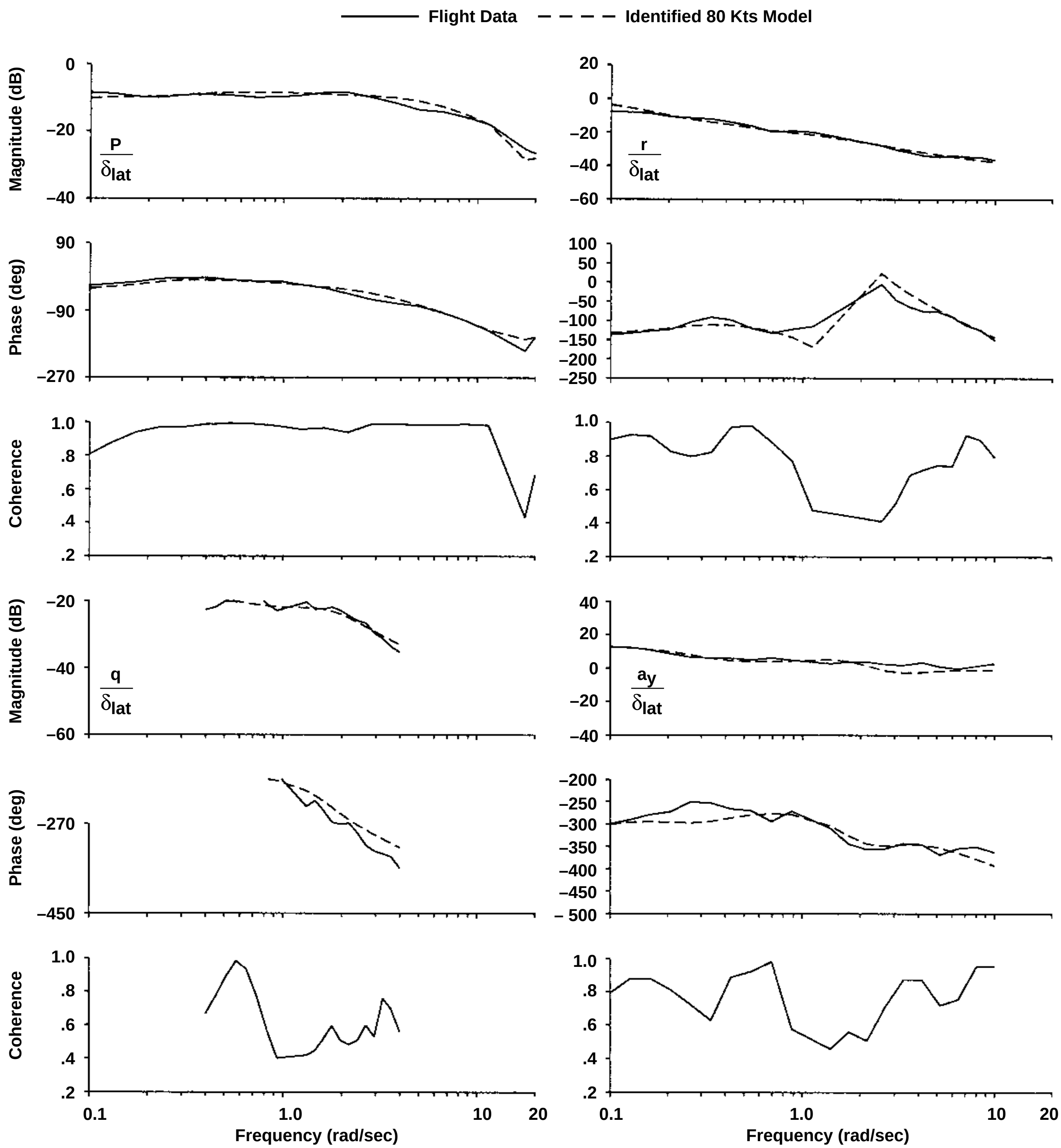

Figure C-1. 80 kts frequency response comparison.

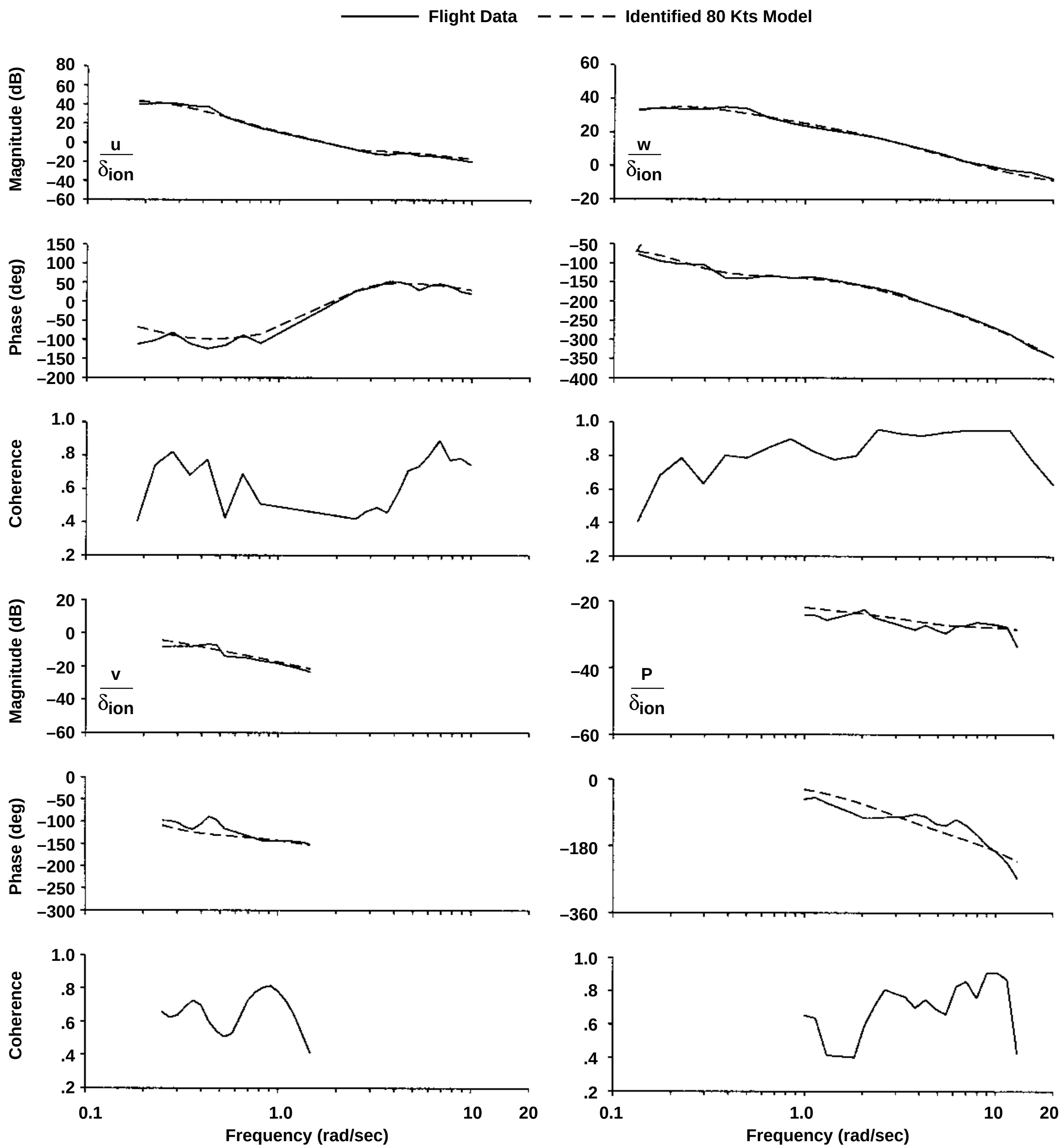

Figure C-1. Continued.

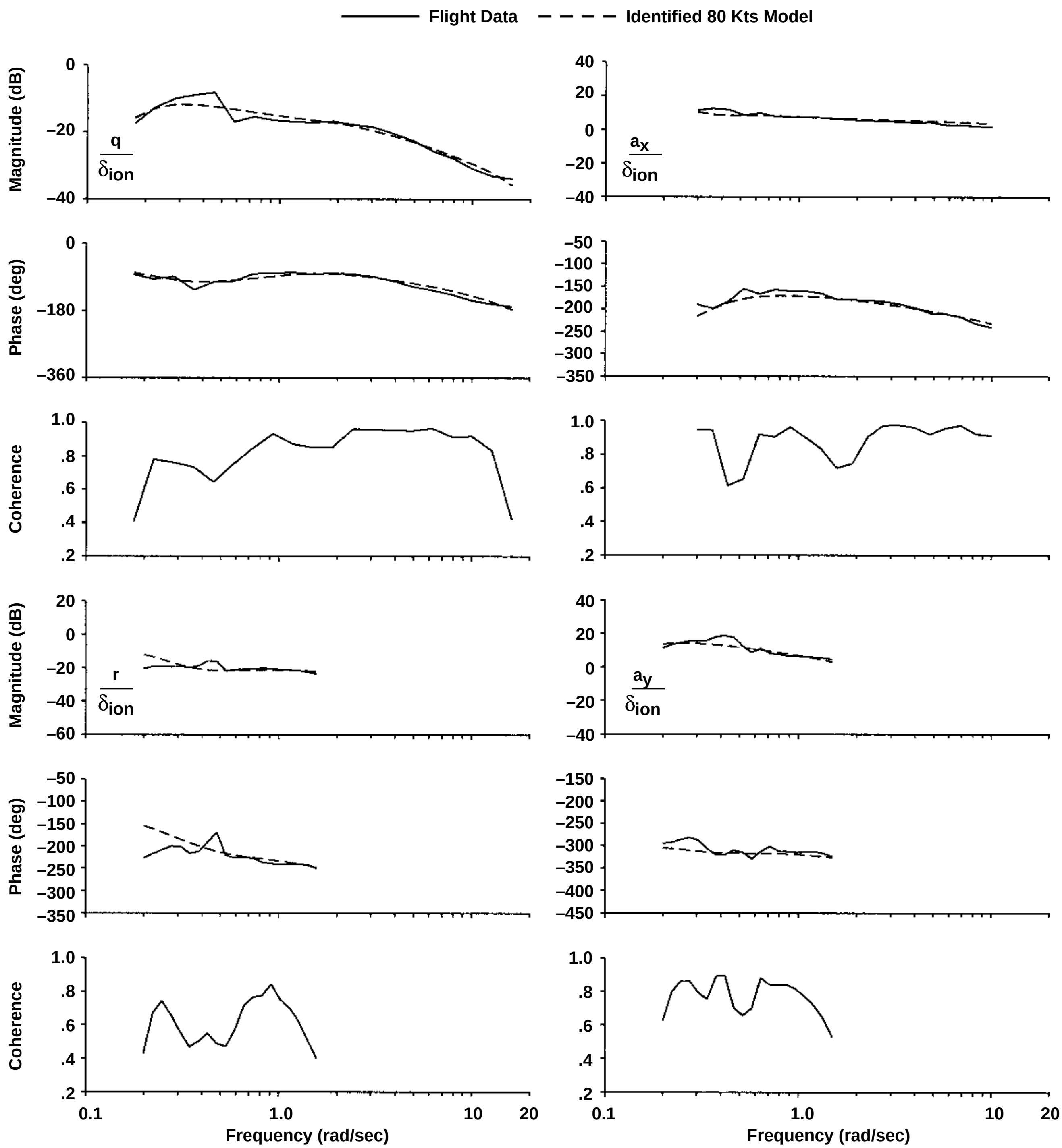

Figure C-1. Continued.

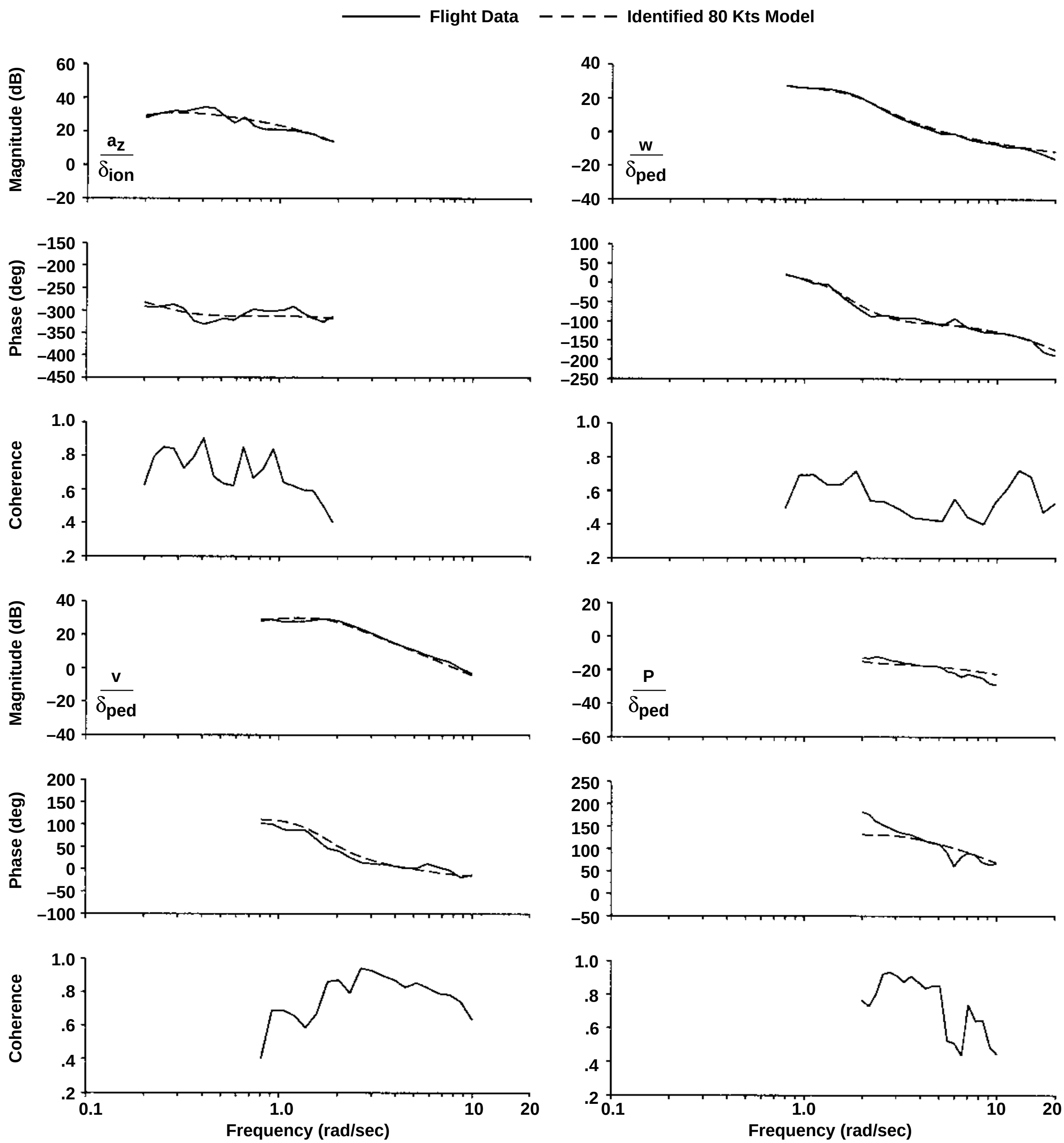

Figure C-1. Continued.

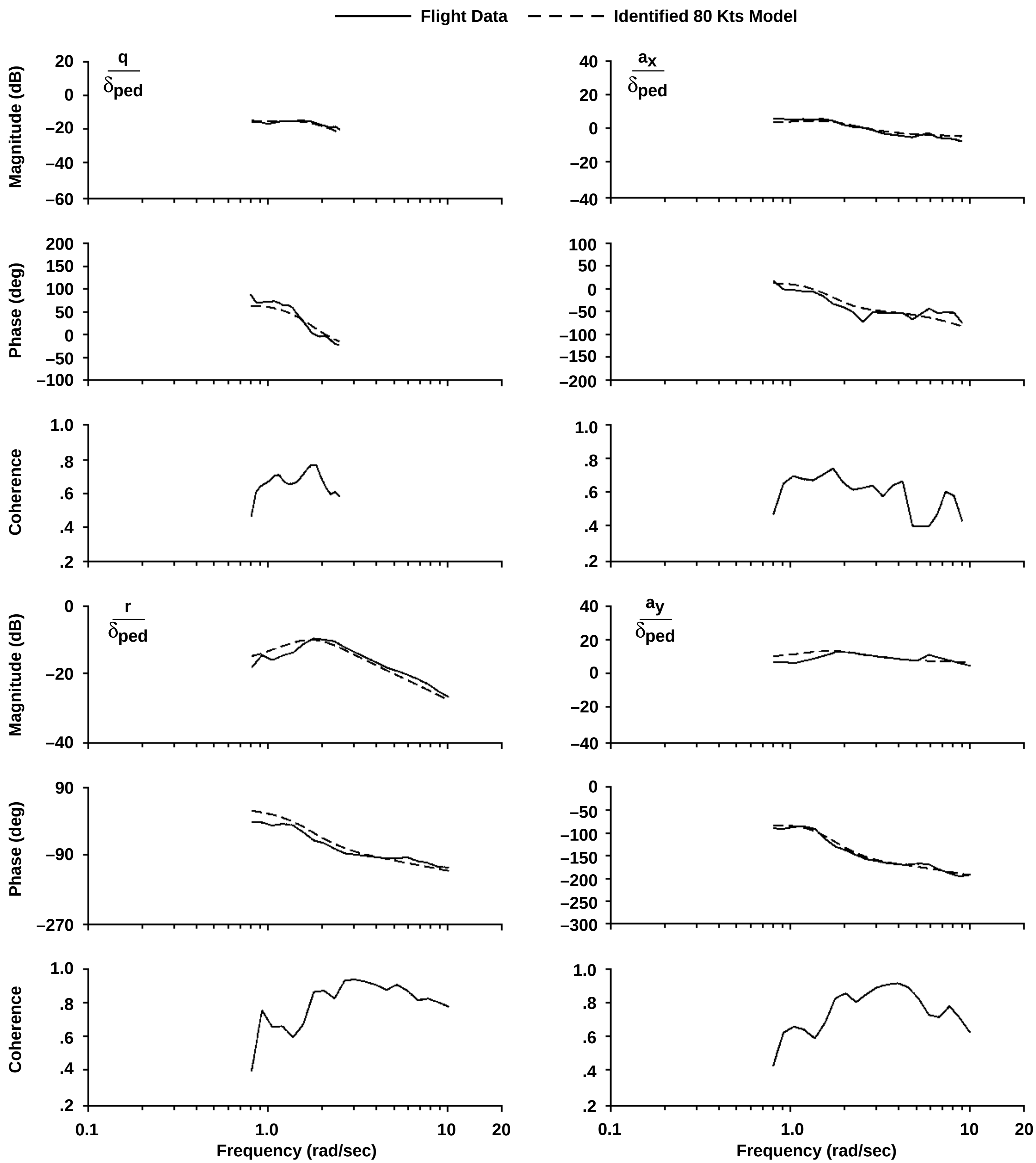

Figure C-1. Continued.

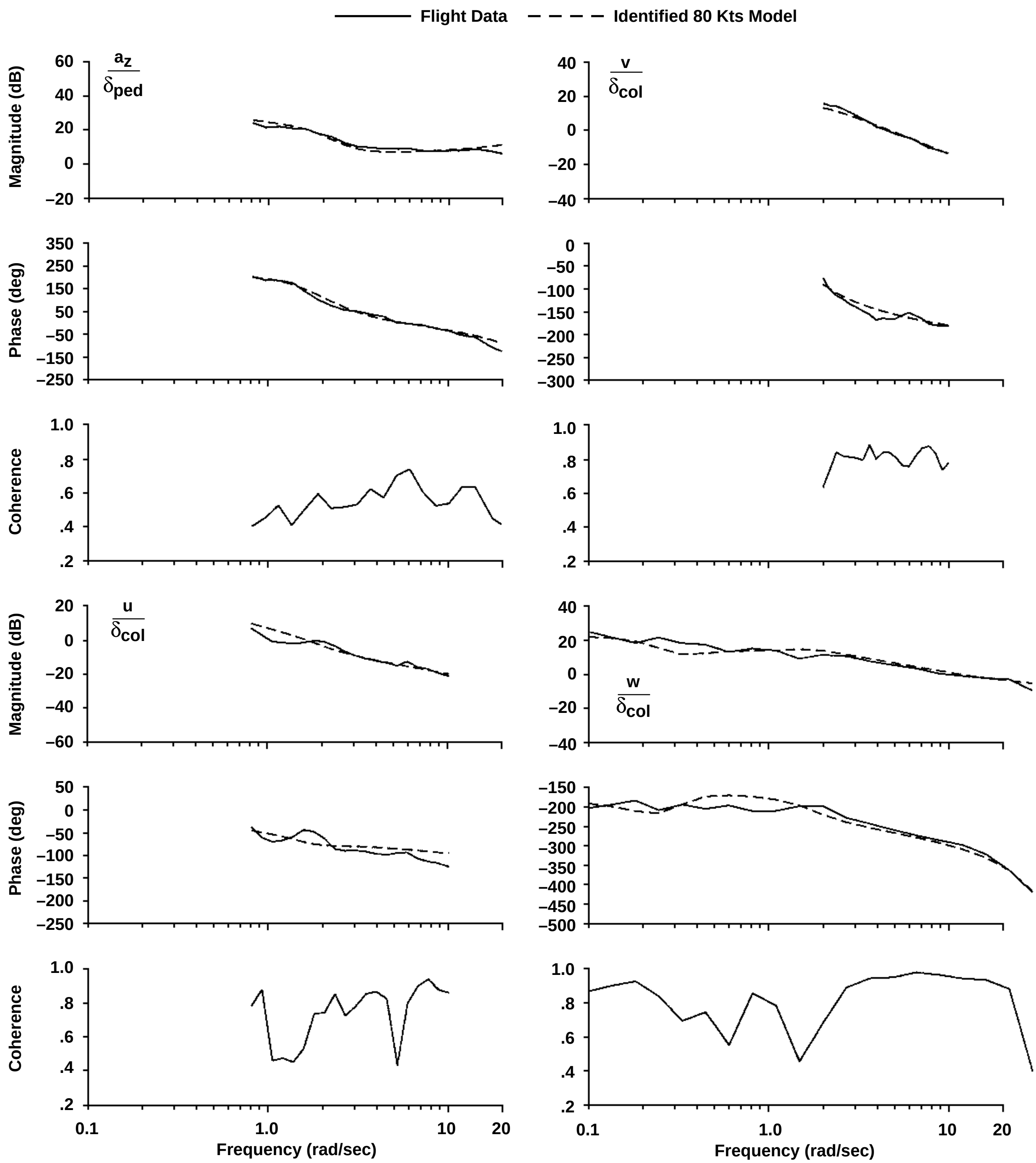

Figure C-1. Continued.

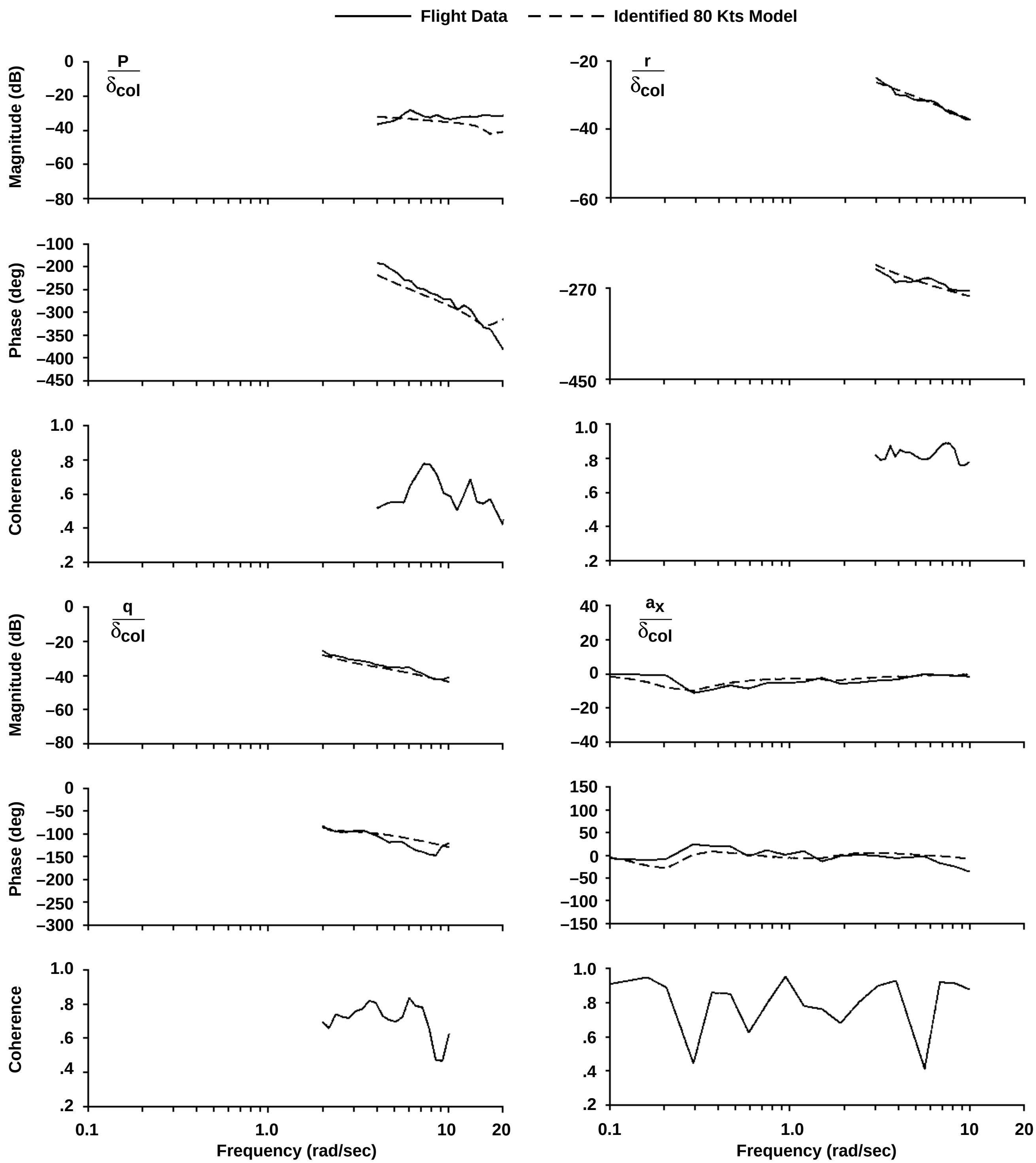

Figure C-1. Continued.

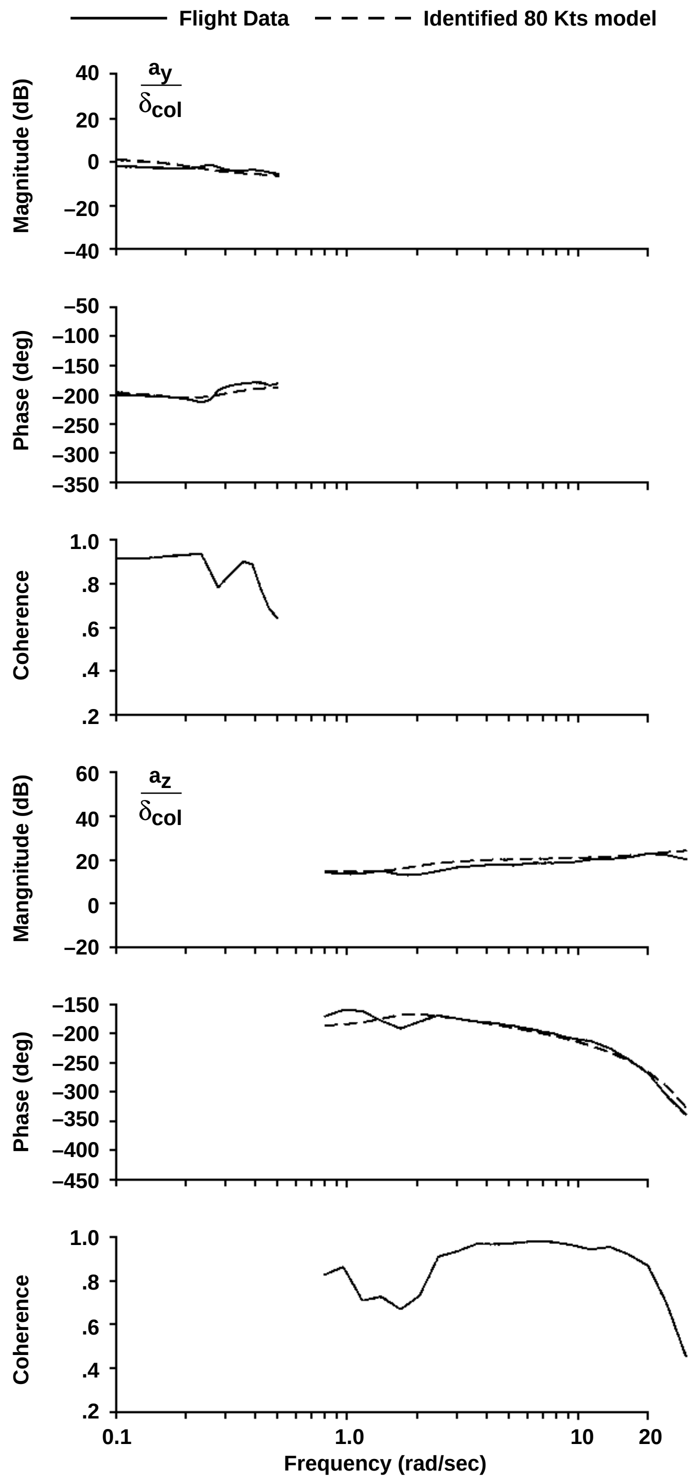

Figure C-1. Concluded.